

Determining design guidelines for a haptic admittance display in aircraft control

S. Kistemaker

Delft University of Technology



This page is intentionally left blank.

Determining design guidelines for a haptic admittance display in aircraft control

by

S. Kistemaker

in partial fulfilment of the degree of Master of Science
in Aerospace Engineering at Delft University of Technology.

Student number: 4377656
Project duration: June 25, 2020 – December 21, 2021
Thesis committee: Prof. dr. ir. M. (Max) Mulder, TU Delft, supervisor
Dr. ir. M.M.(René) van Paassen, TU Delft, supervisor
Dr. O.A. (Alexei) Sharpanskykh, TU Delft
Dr. ir. W. (Wei) Fu, TU Delft (guest)

This thesis is confidential and cannot be made public until 21/12/2023.

An electronic version of this thesis is available at <http://repository.tudelft.nl/>.

Preface

This thesis marks the end of an amazing chapter of my life, in which I got to study a field of engineering that I love, meet many new friends and just have a great time in general. The final part of this chapter started with me emailing Max, in search for an interesting thesis subject at the human-machine systems research group. And an interesting topic it certainly was! Max and René, I want to thank you so much for being so involved and supportive from the start of the project until the very end. After every meeting we had, you left me more motivated than before and your insightful feedback enabled me to focus on the right things, which are things that I am really grateful for.

Besides the friends with whom I have had memorable times at Delft Hyperloop, Proteus and the VSV, I particularly want to thank my roommates for all the good times we had at the EduP. You guys have played the biggest part in how I have grown as a person over the past seven years, and that is something for which I am extremely grateful. Finally, saving the best for last, I want to thank my parents. Mom and dad, you have always been supportive of me with everything that I wanted to do in life and you have always been there to help me and Maaïke out. It is easy to take good things for granted, but I want to assure you that I am not. Without you I would not have been close to the person I am today, and for that I will be always grateful.

*Sander Kistemaker
Delft, December 3rd 2021*

Contents

Preface	iii
List of Abbreviations	vii
List of Symbols	xii
List of Tables	xiii
List of Figures	xv
I Paper	1
II Preliminary thesis (previously graded under AE4020)	17
1 Introduction	19
2 Understanding the problem	23
2.1 A review of manual control	23
2.2 A review of haptics in aircraft control	25
2.3 The active stick	26
2.4 The neuromuscular system and its adaptive nature	27
2.5 The experimental setting and previous findings	27
2.5.1 Forcing function design and controlled element dynamics	27
2.5.2 Sign conventions	30
2.5.3 Previous experimental findings	31
2.6 Thesis objective and academic roadmap	32
3 Quantifying cognitive and reflexive control behavior	35
3.1 Modelling the neuromuscular system	35
3.1.1 Muscle spindles	35
3.1.2 Golgi tendon organs	36
3.1.3 Intrinsic arm properties	36
3.1.4 Muscle activation	36
3.1.5 Skin dynamics	37
3.2 Modelling cognitive and nonlinear behavior	37
3.3 Unification of the theory to model the experiment	38
4 Applying the model and devising a test strategy	41
4.1 Preparation of the data fitting algorithm	41
4.1.1 Analytical derivation and verification of model transfer functions	42
4.1.2 The data fitting algorithm	42
4.2 Quantification of human control behavior	44
4.2.1 Reduction of upper and lower bounds on remaining parameters	45
4.2.2 Identification of relations between human controller parameters	45
4.2.3 Definition of three human controller settings	52
4.3 Quantification of aircraft dynamics and active stick settings	61
4.4 Simulation output and observations	63
4.5 Reflection on existing manual control theory	70
4.6 Proposal of active stick tuning procedure	73
4.7 Testing conditions and performance predictions	75

5	Experiment design	79
5.1	Summary of the experimental setting.	79
5.2	Envisioned data analysis.	80
6	Conclusion	81
	Bibliography	82
III	Preliminary thesis appendix (previously graded under AE4020)	87
A	Analytical transfer function derivations	89
IV	Paper appendix	95
B	Clarification of the pilot model	97
C	Participant briefing	99
C.1	Context of the experiment and research objective.	99
C.2	The experiment.	99
C.3	Risks.	100
C.4	Planning	100
D	All experimental frequency response functions	101
E	Instructions for the project's code	105

List of Abbreviations

BW	Bandwidth
B747	Boeing 747
CC	Cessna Citation
CE	Controlled element
CNS	Central nervous system
CL	Closed-loop
dCL	Disturbance closed-loop
DOF	Degree of freedom
dOL	Disturbance open-loop
FBW	Fly-by-wire
FRF	Frequency response function
FT	Force task
GTO	Golgi tendon organ
HC	Human controller
HMI	Human-machine interface
LCD	Liquid crystal display
MS	Muscle spindle
MVT	Maximum voluntary torque
NMS	Neuromuscular system
OL	Open-loop
PDF	Probability density function
PIO	Pilot-induced oscillation
PT	Position task
RMS	Root mean square
RT	Relax task
SNR	Signal-to-noise ratio
tCL	Target closed-loop
tOL	Target open-loop
TU Delft	Technical University Delft

List of Symbols

β	Forcing function shaping filter lead corner frequency	[rad/s]
δ_a	Forcing function shaping filter lead corner frequency	[rad/s]
μ_b	Non-dimensional mass parameter for asymmetric aircraft motions	[-]
ω_{act}	Neuromuscular activation corner frequency	[rad/s]
$\omega_{c,d}$	Disturbance rejection gain crossover frequency	[rad/s]
$\omega_{c,n}$	Cognitive noise corner frequency	[rad/s]
$\omega_{c,t}$	Target tracking gain crossover frequency	[rad/s]
ω_c	Gain crossover frequency	[rad/s]
ω_d	Disturbance forcing function sinusoid frequency	[rad/s]
$\omega_{ff,L}$	Forcing function shaping filter lead corner frequency	[rad/s]
$\omega_{ff,l}$	Forcing function shaping filter lag corner frequency	[rad/s]
$\omega_{lpf,L}$	Low-pass filter lead corner frequency	[rad/s]
$\omega_{lpf,l}$	Low-pass filter lag corner frequency	[rad/s]
ω_t	Target forcing function sinusoid frequency	[rad/s]
ϕ	Aircraft roll angle	[rad]
$\phi_{m,d}$	Disturbance rejection phase margin	[°]
$\phi_{m,t}$	Target tracking phase margin	[°]
σ_e	Tracking error standard deviation	[rad]
$\sigma_{m_{grip}}$	Grip force standard deviation	[Nm]
$\sigma_{n,c}$	Cognitive noise standard deviation	[rad]
$\sigma_{n,m}$	Motor noise standard deviation	[Nm]
θ_d	Disturbance forcing function sinusoid phase angle	[rad]
θ_t	Target forcing function sinusoid frequency	[rad]
ζ_{ff}	Forcing function shaping filter damping ratio	[-]
ζ_{lpf}	Low-pass filter damping ratio	[-]
$(K_{\dot{\phi}})_{opt}$	Optimal manipulator roll rate feedback gain	[-]
$(K_{fwd})_{opt}$	Optimal manipulator feed-forward gain	[-]

$\overrightarrow{x_{+1\sigma}}$	Phasor representing the $+1\sigma$ value of a measured data point's magnitude and phase [-]	
$\overrightarrow{x_{\mu}}$	Phasor representing the mean of a measured data point's magnitude and phase [-]	
$\overrightarrow{x_{diff}}$	Difference vector that is equal to $\overrightarrow{x_{\mu}} - \overrightarrow{x_{+1\sigma}}$	[-]
\vec{v}_0	Optimization vector, initial guess	[-]
\vec{v}	Optimization vector	[-]
A_d	Disturbance forcing function sinusoid amplitude	[rad]
A_t	Target forcing function sinusoid amplitude	[rad]
b	Wing span	[m]
b_{act}	Neuromuscular activation damping	[Nms ² /rad]
B_i	Intrinsic arm damping	[Nms/rad]
B_{skin}	Skin damping	[Nms/rad]
B_{st}	Passive stick damping	[Nms/rad]
C	Optimization cost value	[-]
C_{fwd}	Constant to which $(K_{fwd})_{opt}$ is hypothesized to be related	[-]
C_L	Lift coefficient	[-]
D_e	Cognitive response, differentiator gain	[-]
e	Perceived tracking error signal	[rad]
f_d	Disturbance forcing function	[rad]
f_t	Target forcing function	[rad]
$H_{act}(= H_6)$	Neuromuscular activation dynamics	[-]
H_{ac}	Aircraft actuator dynamics	[-]
H_c	Controlled element dynamics	[-]
H_{delay}	Visual perception delay dynamics	[-]
H_{ff}	Forcing function shaping filter dynamics	[-]
$H_{gto}(= H_5)$	Golgi tendon organ dynamics	[-]
H_{hfb}	Haptic feedback dynamics	[-]
$H_i(= H_3)$	Intrinsic arm dynamics	[-]
H_{lpf}	Low-pass filter dynamics	[-]
$H_{ms}(= H_4)$	Muscle spindle dynamics	[-]
H_n	Cognitive noise shaping filter dynamics	[-]
$H_{skin}(= H_1)$	Skin dynamics	[-]

H_{st}	Passive stick dynamics	[-]
$I_{arm}(= H_2)$	Arm inertia	[Nms ² /rad]
I_e	Cognitive response, integrator gain	[-]
I_{st}	Passive stick inertia	[Nms ² /rad]
$K_{\dot{\phi}}$	Manipulator roll rate feedback gain	[-]
K_c	Controlled element open-loop gain	[-]
K_d	Gain used in the basic transfer functions that approximate aircraft dynamics in the human crossover region	[-]
K_{ff}	Forcing function shaping filter gain	[-]
K_{fwd}	Manipulator feed-forward gain	[-]
K_f	Golgi tendon organ force gain	[-]
K_i	Intrinsic arm stiffness	[Nm/rad]
K_p	Muscle spindle stretch gain	[-]
K_{skin}	Skin stiffness	[Nm/rad]
K_{st}	Passive stick stiffness	[Nm/rad]
K_v	Muscle spindle stretch rate gain	[-]
K_X^2	Aircraft moment of inertia around the roll axis	[-]
K_Z^2	Aircraft moment of inertia around the yaw axis	[-]
M	Mach number	[-]
m_i	Muscle force produced by intrinsic mechanical arm properties	[Nm]
m_{grip}	Grip force exerted on the manipulator	[Nm]
m_{meas}	Grip force measured by the manipulator	[Nm]
m_{mus}	Total muscle force produced produced by the arm	[Nm]
m_{refl}	Muscle force produced by neuromuscular activation	[Nm]
m_{res}	Resultant force that acts upon the arm	[Nm]
p	Aircraft roll rate	[rad/s]
P_e	Cognitive response, proportional gain	[-]
r	Aircraft yaw rate	[rad/s]
R^2	Coefficient of determination	[-]
T_{gto}	Golgi tendon organ neural transport delay	[-]
T_{ms}	Muscle spindle neural transport delay	[-]

T_{visual}	Visual perception delay	[s]
u	Total control signal	[rad]
u_p	Pilot control signal	[rad]
u_{gto}	Golgi tendon organ signal	[-]
u_{ms}	Muscle spindle signal	[-]
u_{sup}	Supraspinal reference signal	[-]
u_{tot}	Total neuromuscular activation signal	[-]
V	Airspeed	[m/s]
$W(N)$	The weight belonging to data point N in the optimization	[-]
W_n	Cognitive noise intensity	[rad ²]
x_m	Manipulator deflection	[rad]
x_{arm}	Local arm deflection	[rad]
$x_{st_{max}}$	Maximum stick deflection	[rad]
Y	Lateral body force exerted on an aircraft	[N]
y	Aircraft state	[-]
Y_p	Lumped pilot dynamics for McRuer's compensatory roll task [1]	[-]

List of Tables

2.1	The forming filter properties that define the three forcing function variants used by Fu [14].	29
2.2	The properties of the three target forcing functions tested by Fu [14]. The signal in bold is the one that will be used in the upcoming experiment.	30
2.3	The properties of the three disturbance forcing functions tested by Fu [14]. The signal in bold is the one that will be used in the upcoming experiment.	30
4.1	The quantified human controller parameters after iteration 0.	44
4.2	The quantified human controller parameters after iteration 1.	46
4.3	An overview of the upper and lower limits reached while fitting the model on the existing experimental data for $K_i = 4$ Nm/rad and $P_e = -1, -1.5, -2, \dots, -3.5$ for Fu's intermediate bandwidth.	52
4.4	An overview of the upper and lower limits reached while fitting the model on the existing experimental data for $P_e = -3$ and $K_i = 3, 3.5, \dots, 6.5$ Nm/rad for Fu's intermediate bandwidth. Only one gain crossover point existed for some of the open-loop disturbance FRFs, hence the 'N.A.' entries as an extremity of the second crossover points (see Figure 4.4 for visual clarification).	53
4.5	A summary of the relations shown in Figures 4.6 and 4.7, the approximations that were used and the 'average controller' setting that was derived from the approximation of the other two settings.	56
4.6	The distinctive parameters for the relaxed, average and tense controller. The specific crossover characteristics belong to the scenario of the Boeing 747 roll dynamics, where $K_{fwd} = 2.5$ and $K_\phi = -0.2857$	59
4.7	The crossover characteristics of the controlled element dynamics shown in Figure 4.11.	62
4.8	The target forcing function that is used in the simulations.	65
4.9	The disturbance forcing function that is used in the simulations.	65
4.10	The best recorded settings for all aircraft, for all three pilot settings.	65
4.11	The conditions to be tested in the experiment. The six green scenarios will be tested by all participants, whereas every participant will only test one of the four yellow experimental conditions.	75
B.1	An overview of the pilot coefficients that were defined as constants (green), and the remaining ones that were estimated for each pilot control style.	98

List of Figures

1.1	A basic framework of the approach envisioned for this thesis.	21
2.1	A basic representation of the conventional compensatory tracking task, in the context of flight.	24
2.2	The passive and active stick models as presented by Fu [14]. (a) Schematic diagram of the passive stick model, where the stick deflection is directly the result of force applied to the manipulator. (b) Schematic diagram of the active stick model, where the stick deflection is imposed on the human controller using measured system behavior.	26
2.3	A schematic representation of the neuromuscular system.	28
2.4	The LCD screen and manipulator used in the experiment [14].	29
2.5	Prefiltering of the disturbance forcing function f_d [14].	29
2.6	The sign conventions used in this thesis (modified images from [14]).	31
2.7	A visual explanation of how the identity of the active stick's haptic feedback (i.e., a pure rate feedback $K_m s$ in this case) dictates the CE dynamics that the human controller effectively experiences [14].	32
2.8	A graphical representation of the scientific contribution of this thesis, as well as two possible lines of development that may follow after.	33
3.1	The TU Delft neuromuscular model, which includes the red boundary conditions used by De Vlugt et al. [34] to identify the neuromuscular characteristics.	36
3.3	A schematic representation of the (a) passive (b) force and (c) active stick model, where the green 'NMS model' block acts as a small substitute for Figure 3.1. The force stick model bridges the conceptual gap between the passive and active stick that were introduced in Sections 2.1 and 2.3, respectively, but the active stick model is the one that will be focused on for the remainder of this thesis.	40
4.1	An overview of the workflow and the way content is organized in Chapter 4.	41
4.2	Verification of the analytical descriptions for the active stick model, for the open- and closed-loop (a) target tracking and (b) disturbance rejection response.	47
4.3	A demonstration of how a difference vector is calculated for every experimental frequency response data point generated by Fu [14]. In this example, data point six of ten from the open-loop disturbance rejection Bode plot of Fu's intermediate bandwidth (BW2) is selected.	48
4.4	Bode plot of the PD and PID open-loop disturbance rejection FRFs summarized in Table 4.4, which demonstrates the presence of multiple gain crossover points at many of the tested settings. For these situations, the most extreme minimal stability margins have been recorded as the second crossover point in Tables 4.3 and 4.4.	49
4.5	Bode plots of all the dynamic systems that the data fitting algorithm converged to, when fitting the model on Fu's intermediate bandwidth data with $P_e = [-3.5, -1]$ and $K_i = 4$	51
4.6	An overview of all the possible proprioceptor gains that realized a target tracking crossover frequency of $\omega_{c,t} \approx 1.7$ rad/s (circles) and $\omega_{c,t} \approx 2.5$ rad/s (triangles).	54
4.7	An overview of all the possible cognitive response gains that realized a target tracking crossover frequency of $\omega_{c,t} \approx 1.7$ rad/s (circles) and $\omega_{c,t} \approx 2.5$ rad/s (triangles).	55
4.8	A graphical representation of all the bold functions from Table 4.5, where the blue, green and red planes correspond with the relaxed, average and tense controller, respectively. It should be noted that Figures 4.8d and 4.8e are rotated by 90 degrees with respect to the other plots, such that visibility of the planes is improved.	57

4.9	Bode plots of all the dynamic systems that the data fitting algorithm converged to, when fitting the model on Fu's intermediate bandwidth data with $P_e = -3$ and $K_i = [3, 3.5, \dots, 6.5]$	58
4.10	A Bode plot of the relaxed (blue), average (red) and tense (yellow) controller for the open-loop (a) target tracking and (b) disturbance rejection response for the Boeing 747, where $K_{fwd} = 2.5$ and $K_{\dot{\phi}} = -0.2857$	60
4.11	The controlled element dynamics that are simulated in this thesis: the Boeing 747 (blue), the F-16 (red) and the Cessna 500 Citation (yellow).	63
4.12	The (a) $RMS(e)$ and (b) $RMS(m_{grip})$ values from Table 4.10 plotted in a graph, to emphasize the highly similar performance that can be achieved for the Boeing 747, the F-16 and the Cessna Citation.	65
4.13	A clarification of what (a) a regular, stable model condition and (b) a light gray, oscillatory model condition produced as simulation output. Here, the blue and red graph represent the target forcing function f_t and aircraft roll angle ϕ , respectively, and the yellow graph shows the m_{grip} that realized this response.	66
4.14	Simulation output for the Boeing 747.	67
4.15	Simulation output for the F-16.	68
4.16	Simulation output for the Cessna 500 Citation.	69
4.17	The control setting used by McRuer [1].	70
4.18	Experimental output generated by McRuer [1] for the compensatory roll task.	71
4.19	The average target tracking crossover frequencies achieved by participants in the experiment conducted by Fu [14]. The highlighted data point is most relevant, as the intermediate bandwidth forcing functions (see Tables 2.2 and 2.3) are used in this thesis as well.	73
4.20	The CE dynamics shown earlier in Figure 4.11, combined with the second-order transfer functions that approximate the three aircraft in the human crossover region (indicated in red).	74
4.21	An illustration of where inside the oscillatory zone of the simulation output the 'exotic' testing conditions are located for (a) the Boeing 747 and (b) the Cessna Citation.	76
4.22	A prediction of the HC's performance for testing conditions 1 to 6, which are introduced in Table 4.11.	77
A.2	A simplified block diagram of the passive stick a) target tracking and b) disturbance rejection open-loop response, that aims to highlight their similarity.	93
A.3	Verification of the analytical descriptions for the passive stick model, for the open- and closed-loop (a) target tracking and (b) disturbance rejection response.	94
B.1	A more detailed overview of the pilot model that is used in the simulations.	97
C.1	A visual summary of the experimental setting.	100
C.2	General planning of the experiment for a given participant.	100
D.1	The frequency response functions of conditions 1 (blue circle), 2 (red triangle) and 7 (black square), which respectively represent the cases of single, double and triple K_{fwd} for the Boeing 747. All values are reported as mean \pm std. deviation.	102
D.2	The frequency response functions of conditions 4 (blue circle), 5 (red triangle) and 8 (black square), which respectively represent the cases of single, double and triple K_{fwd} for the Cessna Citation II. All values are reported as mean \pm std. deviation.	102
D.3	The frequency response functions of conditions 1 (blue circle) and 3 (red triangle), which respectively represent the cases of single and double $K_{\dot{\phi}}$ for the Boeing 747. All values are reported as mean \pm std. deviation.	103

D.4	The frequency response functions of conditions 1 (blue circle) and 3 (red triangle), which respectively represent the cases of single and double $K_{\dot{\phi}}$ for the Cessna Citation II. All values are reported as mean \pm std. deviation.	103
D.5	The frequency response functions of conditions 2 (blue) and 3 (red), which respectively represent the cases of double K_{fwd} and double $K_{\dot{\phi}}$ for the Boeing 747. All values are reported as mean \pm std. deviation.	104
D.6	The frequency response functions of conditions 2 (blue) and 3 (red), which respectively represent the cases of double K_{fwd} and double $K_{\dot{\phi}}$ for the Cessna Citation II. All values are reported as mean \pm std. deviation.	104

I

Paper

Determining design guidelines for a haptic admittance display in aircraft control

Sander Kistemaker*, supervised by Max Mulder† and M. M. (René) van Paassen‡
Delft University of Technology, 2600 GB Delft, The Netherlands

DOI: 0000000/0.G00000

The haptic feedback signal in haptic interfaces is usually in the form of a force on the control device. In contrast, the “active side stick”, investigated in the 80s and 90s, uses an admittance display, whereby the position of the device is linked to the feedback signal, and force applied on the device is used as the control signal. These devices are usually tuned in a serendipitous manner. To better understand the potential and tuning rules for these devices, tuning is investigated with a model-based approach and verified in pilot-in-the loop experiments using various aircraft dynamics. It was found that certain gain settings offered considerable benefits in terms of tracking performance as well as the control effort exerted by the pilot, while taking into account the system’s stability margins. Based on these findings, a comprehensive tuning procedure is proposed for control systems involving an active manipulator.

I. Introduction

IN RECENT years, haptics have received an increasing amount of attention to improve the performance of human controllers (hereafter referred to as pilots) in manual control tasks. Not only can they improve performance in situations that are impractical to automate (e.g., exploratory tasks like robotic surgery [1] [2] and remotely-controlled exploration vehicles [3] [4]), but also form a flexible alternative in situations where the automation fails to deliver (e.g., evasive maneuvers or aircraft landings without functioning navigational systems). In some of these applications, the automation is able to communicate its intentions back to the pilot, while still providing the pilot with the possibility to override those intentions. This design philosophy is referred to as ‘haptic shared control’ [5] [6] [7]. In the current applications of haptic shared control for aircraft and many of the ones that have been researched recently, the pilot’s arm is either being pushed towards a setting that results in a trajectory that is desired by the aircraft [8], or the arm is being pushed away from settings that produce undesirable or dangerous flight conditions [9] [10] [11]. This is typically done through force feedback from the manipulator or active adjustment of the manipulator’s mechanical properties.

Whereas these designs may improve pilot performance, they fail to create a permanent and intuitive connection between the manipulator and the vehicle itself which, to a certain degree, means that these two objects move as two separate entities. Such a ‘passive manipulator’ configuration can be contrasted with the example of a person driving a car, for which the steering wheel serves two major purposes. First and foremost, it allows the pilot to send control commands to the vehicle, as is the case for the passive manipulator. Second, the position of the steering wheel is effectively coupled to the direction in which the car is moving, which one can feel particularly when being confronted with strong crosswinds. In other words, using the steering wheel, the car permanently provides the pilot with a haptic representation of the direction in which it is turning. This results in there being a permanent, bilateral stream of information at the steering wheel that is facilitated with haptic cues, which is a configuration referred to as a ‘haptic admittance display’ or ‘active manipulator’ in this paper.

A key advantage of such a configuration is that it essentially dele-

gates a portion of the control task to the neuromuscular system (NMS). Detecting and responding to disturbances like wind using visual and vestibular (motion) cues takes time and brainpower, while the intrinsic mechanical properties of the arms as well as reflex arcs allow the pilot to respond much quicker to any disturbances presented with the motion of the manipulator. In doing so, the cognitive burden of the task is largely reduced to only tracking a desired target (e.g., a road or a certain flight path), making this configuration feel more intuitive than the passive manipulator. This is one of the key findings produced by Fu [12], who most recently studied this configuration in the context of flight, which was done first by Hosman and Van der Vaart [13]. By conducting a compensatory roll task, Fu [12] showed that an active manipulator can provide significant benefits over a passive manipulator, in terms of tracking performance as well as control effort exerted by the pilot.

Another benefit lies in the fast and direct link that the active manipulator provides between pilot and aircraft, namely that it has the potential to stretch the limit of what systems pilots can stabilize and control manually. This could prove particularly useful in cases of extreme turbulence, malfunctioning stability augmentation systems or sudden deterioration of an aircraft’s dynamical behavior (e.g., due to wing damage or engine failure).

This paper aims to determine whether the design of flight control systems involving a haptic admittance display can be generalized to a set of practical guidelines. If successful, this could lay the foundation for future research of the more realistic and complex tasks in aircraft control. More specifically, such research could revolve around the use of a multi-dimensional (i.e., roll-pitch) control task, adaptive aircraft dynamics and an on-board setting, thereby fully exploring the potential of this control configuration.

To reach this objective, the technical details of the active manipulator are first introduced in Section II, along with some key findings with regards to the working principle of this configuration. This is followed by a definition of the top-level approach for deriving the desired guidelines in Section III. Afterwards, Section IV introduces the model with which predictions are made for the experiment. Based on the key findings from Section II and the observations made from the simulation results, hypotheses are defined in Section V, along with details of the experiment and the testing conditions that are based on said hypotheses. Afterwards, the results of this experiment are presented and discussed in Sections VI and VII. Using these findings, the hypotheses are revisited in Section VIII and proposals are made for a tuning procedure of the active manipulator and for future research topics in this area. Finally, the report is concluded in Section IX.

II. Background

To gain an understanding of how the active manipulator functions, it makes sense to compare it to the simpler and more familiar passive manipulator, which is done using Figs. 1 and 2 for a rolling aircraft. For both configurations holds that for a given deflection of the control

Copyright ©2021 by S. Kistemaker, M. Mulder and M. M. van Paassen, Delft University of Technology. Published by the American Institute of Aeronautics, Inc., with permission. All requests for copying and permission to reprint should be submitted to CCC at www.copyright.com; employ the eISSN 1533-3884 to initiate your request. See also AIAA Rights and Permissions www.aiaa.org/randp.

*MSc student, Section Control and Simulation, Faculty of Aerospace Engineering; s.kistemaker@student.tudelft.nl

†Full Professor, Section Control and Simulation, Faculty of Aerospace Engineering; m.mulder@tudelft.nl, Member AIAA

‡Associate Professor, Section Control and Simulation, Faculty of Aerospace Engineering; m.m.vanpaassen@tudelft.nl, Associate Fellow AIAA

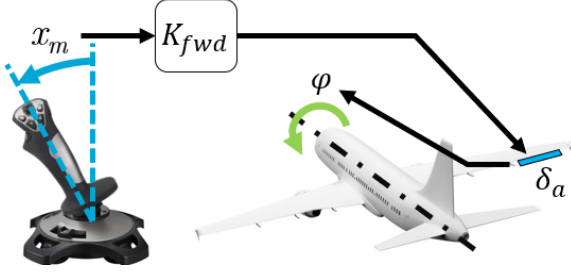


Figure 1. A schematic overview of the passive manipulator configuration, where the aircraft's control surfaces are driven by the measured manipulator deflection (x_m).

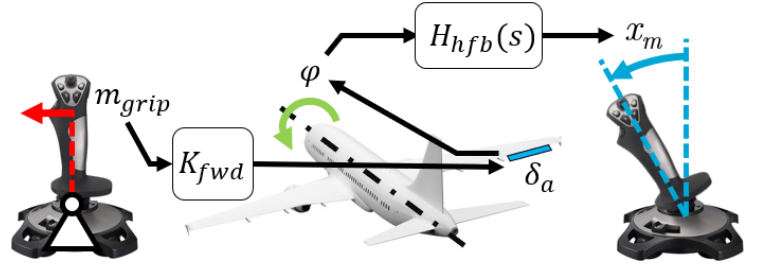


Figure 2. A schematic overview of the active manipulator, where the aircraft's control surfaces are driven by the measured moment of force applied by the pilot (m_{grip}), and where the manipulator's position (x_m) is imposed on the pilot using measurements of the aircraft's roll motion, which is transformed by $H_{hfb}(s)$.

surfaces (δ_a), the aircraft responds with the same rolling motion (ϕ). For the passive manipulator, the aircraft determines the desired deflection of the control surfaces by measuring the angular deflection of the manipulator (x_m), which can be scaled digitally by some feed-forward gain (K_{fwd}) to affect the overall gain of the system. Only limited by the mass, damping and stiffness of the manipulator, the pilot is completely in charge of placing the manipulator at a desired x_m by exerting some force on it.

For the active manipulator, consider it to be a completely rigid object first, as its motion is constrained by an electronic servo. In this case, the aircraft's control surfaces are not driven by the measured position (x_m). Instead, the force applied to the manipulator by the pilot is what drives them in this configuration. As the aircraft starts to roll due to the deflected control surfaces, measurements of the aircraft's motion are transformed by a chosen transfer function $H_{hfb}(s)$ and fed back to the electronic servo, which rotates the manipulator in accordance with the aircraft's motion. Since x_m now forms a representation of the aircraft's state, this effectively creates a haptic link between pilot and aircraft.

Fu [12] showed that the active manipulator was particularly useful for rejecting disturbances more effectively, while there were no significant changes found in the target tracking performance compared to the passive manipulator. This was done by comparing the power spectral density of the error signal e for the passive and active manipulator (see Fig. 3 for a clarification of the compensatory tracking task at hand), which showed that the active manipulator greatly attenuated signal power introduced into the system by the disturbance forcing function (f_d).

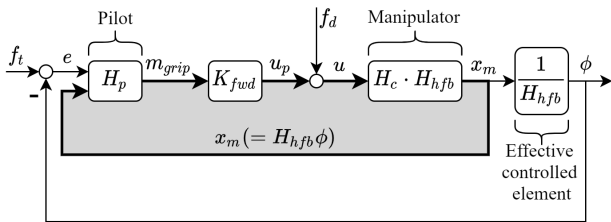


Figure 3. Schematic diagram of the compensatory tracking task, which shows how the highlighted disturbance rejection loop affects the CE dynamics effectively experienced by the pilot (modified image from Fu [12]).

Besides that, Fu reported three other key findings. First, the benefits provided by the active manipulator became more pronounced as the signal bandwidth of the forcing functions increased (in other words, as the control task became more challenging). These benefits in terms of tracking performance and exerted control effort were determined using the root-mean-square (RMS) value of the error signal (e) and the grip moment (m_{grip}), respectively. The second finding is related to the crossover region that McRuer et al. [14] determined for the compensatory roll task ($\omega_c \approx 4.5 - 7$ rad/s), which in turn is related to the maximum frequency at which pilots can send conscious control commands

to the system. Fu [12] discovered through the feedback from participants that haptic cues beyond this frequency band were unhelpful and merely added workload for the pilot. To combat this issue, a lag-lead filter was designed for the haptic feedback loop to attenuate signals beyond this frequency band, which led to increased user comfort without any significant change in tracking performance. Third, Fu [12] showed that the character of $H_{hfb}(s)$ has a decisive impact on the controlled element (CE) dynamics that the pilot effectively experiences. In the new configuration, the original CE dynamics (i.e., the aircraft dynamics, represented by $H_c(s)$ in Fig. 3) are essentially integrated into the positioning of the manipulator. As a result, pilots got the impression that they are controlling a system equal to $H_{c,eff}(s) = \frac{1}{H_{hfb}(s)}$.

The previous point highlights the design freedom that this configuration provides. This benefit can be combined with the findings that were produced by McRuer [14] with regards to compensatory tracking tasks. Based on a wide array of experimental conditions that were tested, McRuer concluded that pilots were most effective at controlling systems that have single integrator dynamics (i.e., $H_c(s) = \frac{K_c}{s}$). In these experiments, the adaptive nature of the pilot played a key role in realizing very similar combined open-loop dynamics (i.e., $H_{OL}(s) = H_p(s)H_c(s)$) for different values of K_c and different signal bandwidths for the system's forcing functions f_t and f_d . Combining the pilot's preference to converge to the same open-loop dynamics resembling $H_{OL}(s) = \frac{\omega_c}{s}$ with the argument that $H_{c,eff}(s) = \frac{1}{H_{hfb}(s)}$, one could argue that the preferred haptic feedback transfer function is defined as $H_{hfb}(s) = K_{hfb}s$, where $K_{hfb} = \frac{1}{\omega_c}$. In other words, pure rate feedback seems to be the ideal option for $H_{hfb}(s)$.

III. Top-level approach

When designing a control system involving an active manipulator, numerous factors need to be considered (see Figure 4 for clarification):

1. The feed-forward gain K_{fwd} , which scales the force that is applied by the pilot before it actuates the aircraft's control surfaces.
2. The rate feed-back gain K_{hfb} , which scales the magnitude of the manipulator's motion with respect to the measured rotation rate of the aircraft. This gain is referred to as K_ϕ hereafter, since we are dealing with aircraft roll.
3. The controlled element dynamics.
4. The properties of the lag-lead filter in the haptic feedback loop (denoted as $H_{lpf}(s)$). These have been determined by Fu [12] experimentally by maximizing user comfort without sacrificing performance, which is why this filter will remain unchanged in this paper.
5. The spectral properties of the target and disturbance forcing functions (i.e., the general mission difficulty).
6. The adaptive and complex nature of the pilot's control behavior.

In order to generalize the design of such a control configuration, the compensatory tracking task tested by Fu [12] is first replicated in simulation, using a model that accurately describes the human elements that facilitate the active stick's working principle (i.e., the neuromuscular system). The neuromuscular model developed at TU Delft (TUD) [15] lends itself well for this purpose. The participants in Fu's experimental

conditions were exposed to three types of forcing functions of various difficulties, which evoked different types of control behavior from the pilots. By fitting the model on the experimental frequency response functions (FRFs) generated by Fu under these conditions, three pilot settings (i.e., the ‘relaxed’, ‘average’ and ‘ambitious’ pilot) are defined, which encompass a range of possible control styles.

Second, the experiment is simulated with the roll dynamics of three aircraft (the Boeing 747 as used by Fu [12], the Cessna Citation II as identified by TUD at a standard altitude of 30,000 ft and an airspeed of 121.3 m/s [16] and a linearized model of the F-16 at the same flight condition [17]), the three pilot control styles and 186 manipulator settings, which are defined by K_{fwd} and K_{ϕ} . Fu already researched the effect of forcing function signal bandwidth, which is why this degree of freedom is not explored any further in this paper. Fu’s intermediate and high signal bandwidth forcing functions posed too much of a challenge to participants, which made these signals unsuitable to investigate the effects of other design parameters effectively. This is why the low signal bandwidth forcing functions were selected for modelling and experimental purposes in this paper instead. As a result, the factorial combination of three aircraft, three pilot control styles and 186 manipulator settings amounted to 1,674 simulated conditions.

Third, based on observations from these results and findings produced by McRuer [14] and Fu [12] earlier, hypotheses are stated with regards to the optimal feed-forward and feed-back gain. Based on this, the testing conditions are derived for another compensatory tracking task experiment in the Human-Machine Interface (HMI-) lab at TUD.

IV. Model predictions

This section describes the model-based approach that has been used to make predictions about the experiment that was going to be conducted. A schematic overview of the Simulink model that replicates the experiment is shown in Figure 4. Section IV A first explains how the pilot’s control behavior has been defined. The most elaborate aspect of this definition is summarized in the green ‘NMS model’ block, which contains the neuromuscular model from De Vlught et al. [15]. This model was selected, as it defines the relevant neuromuscular sensors (proprioceptors), actuators (muscles) and linkage (neurons) as separate dynamical systems. Afterwards, Section IV B describes the remaining information that was used to run the simulations, the observations of whose output are presented in Section IV C.

A. Quantification of pilot control behavior

Whereas the NMS model from De Vlught [15] is sufficient to define the pilot’s reflexive and inertial responses, the cognitive process that also drives the NMS needs a definition as well. The widely-used simplified precision model introduced by McRuer and Jex [18] represents the pilot’s equalization of the perceived error signal (e), which enters the pilot through a second-order 0.25 s Padé filter to account for the visual time delay [19]. A noise term is injected at the error signal, which represents the pilot’s non-linear control behavior. Due to the fact that pure rate feedback is employed and the pilot will thereby effectively experience single integrator CE dynamics, a first-order lag [20] shaping filter $H_{sf}(s)$ with a corner frequency of 10 rad/s [21] is used for the noise term. The force sensors and electronic servos inside the manipulator are assumed to be ideal and the lag-lead filter implemented by Fu [12] to attenuate high-frequency components is represented by $H_{lpf}(s)$.

Participants were subjected to sinusoidal target and disturbance forcing functions (Equations 1 and 2, respectively) for runs that lasted 90 seconds, of which the last 81.92 seconds were used for data analysis. Using these forcing functions, Fu [12] was able to experimentally determine FRFs of the average target tracking open-loop ($H_{t,OL}(j\omega_t) = \frac{\phi(j\omega_t)}{E(j\omega_t)}$) and closed-loop responses ($H_{t,CL}(j\omega_t) = \frac{\phi(j\omega_t)}{F_t(j\omega_t)}$), and the disturbance rejection open-loop ($H_{d,OL}(j\omega_d) = \frac{U_p(j\omega_d)}{F_d(j\omega_d)}$) and closed-loop responses ($H_{d,CL}(j\omega_d) = \frac{\phi(j\omega_d)}{F_d(j\omega_d)}$), each containing ten data points that all had their own standard deviation.

$$f_t(t) = \sum_{k=1}^{10} A_t(k) \sin(\omega_t(k)t + \theta_t(k)) \quad (1)$$

$$f_d(t) = \sum_{k=1}^{10} A_d(k) \sin(\omega_d(k)t + \theta_d(k)) \quad (2)$$

In total, sixteen coefficients were used to model the pilot’s control response: twelve for the definition of the NMS model from De Vlught [15] and four for the cognitive equalization of the visually perceived error e . To determine three representative settings for these coefficients, two major steps were taken. First, six of the sixteen coefficients that defined the visual response time [19], neural signal transportation [22] and arm inertia [23] were fixed based on literature. Afterwards, the model was fitted on the experimental FRFs of the various conditions tested by Fu [12], while taking into account realistic limits for the remaining coefficients [24] [25] [26]. For every testing condition, a sum-of-squares cost function was defined involving the 40 available data points of that condition. Before the non-linear optimization MATLAB routine *fmincon.m* estimated the ten coefficients for the different conditions, weights were applied to every data point based on the relative size of their standard deviation.

Finally, this resulted in three pilot control styles, where the ‘ambitious’ and ‘relaxed’ setting, respectively, resembled the strongest and weakest tracking performance recorded by Fu [12], with the ‘average’ setting, as the name suggests, being approximately halfway in between the other two. Appendix B can be consulted for a more detailed description of the model that was used and an overview is provided of all coefficients that quantify the model for the relaxed, average and ambitious pilot.

B. Quantification of hardware and simulation strategy

The roll dynamics of the aircraft are defined by the aileron-to-roll-angle dynamics $\frac{\phi(s)}{\delta_a(s)}$ and the aileron’s actuator dynamics $H_{act}(s)$, as shown in Equation 3. For the B747, the F-16 and the Cessna, this resulted in the transfer functions shown in Equations 5, 7 and 9, respectively. The simulated setting ranges of the manipulator were extended up to the point where the system became unstable for nearly all aircraft dynamics and pilot settings, which resulted in a setting range of $K_{fwd} = [0.5, 1, \dots, 10.5]$ and $K_{\phi} = [0.075, 0.150, \dots, 0.600]$.

$$H_c(s) = H_{act}(s) \cdot \frac{\phi(s)}{\delta_a(s)} \quad (3)$$

$$H_{c,B747} = \frac{1}{0.083s + 1} \cdot \frac{12s^2 + 4.362s + 5.313}{s^4 + 2.704s^3 + 1.117s^2 + 1.518s} \quad (4)$$

$$= \frac{7.906s^2 + 2.873s + 3.5}{0.0547s^5 + 0.8067s^4 + 1.842s^3 + 0.819s^2 + s} \quad (5)$$

$$H_{c,F16} = \frac{1}{0.0495s + 1} \cdot \frac{31.12s^2 + 9.354s + 92.11}{s^4 + 1.212s^3 + 5.586s^2 + 3.587s + 0.03915} \quad (6)$$

$$= \frac{31.12s^2 + 9.354s + 92.11}{0.1555s^5 + 3.33s^4 + 4.675s^3 + 18.11s^2 + 11.27s + 0.123} \quad (7)$$

$$H_{c,CC} = \frac{1}{0.083s + 1} \cdot \frac{22.86s^2 + 12.53s + 144.7}{s^4 + 2.535s^3 + 7.019s^2 + 13.87s - 0.2035} \quad (8)$$

$$= \frac{22.86s^2 + 12.53s + 144.7}{0.0830s^5 + 1.21s^4 + 3.118s^3 + 8.17s^2 + 13.86s - 0.2035} \quad (9)$$

For every simulated run, the cognitive non-linearities were generated using the white noise signal $f_{n,c}$, which gave the simulated performance a stochastic nature. To generate representative results for a given model condition, 30 runs that produced a power signal-to-noise ratio at the perceived error e of 10, as supported by Van der El et al. [21] (with $9.95 < \text{SNR}(e) < 10.05$ deemed acceptable), were averaged to produce the simulation outputs that are summarized in Figure 5. As the pilot can readily produce tracking errors and control forces that are equal and of opposing signs across any given run, the RMS values of e and m_{grip} are deemed the most suitable metrics to assess the pilot’s tracking performance and exerted control effort, respectively.

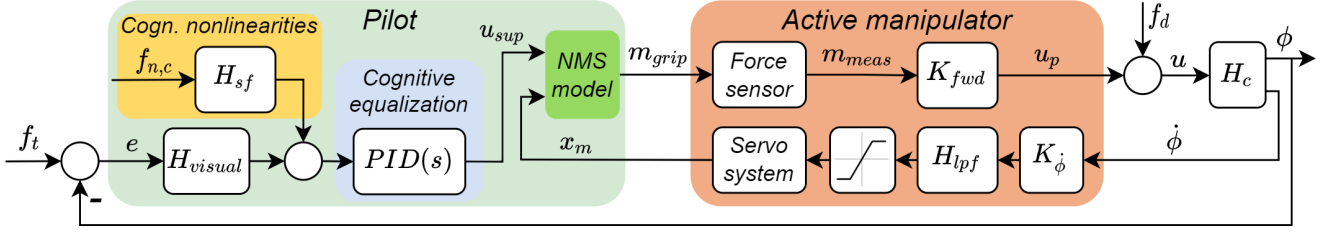


Figure 4. A schematic overview of the Simulink model that is used to simulate the experiment.

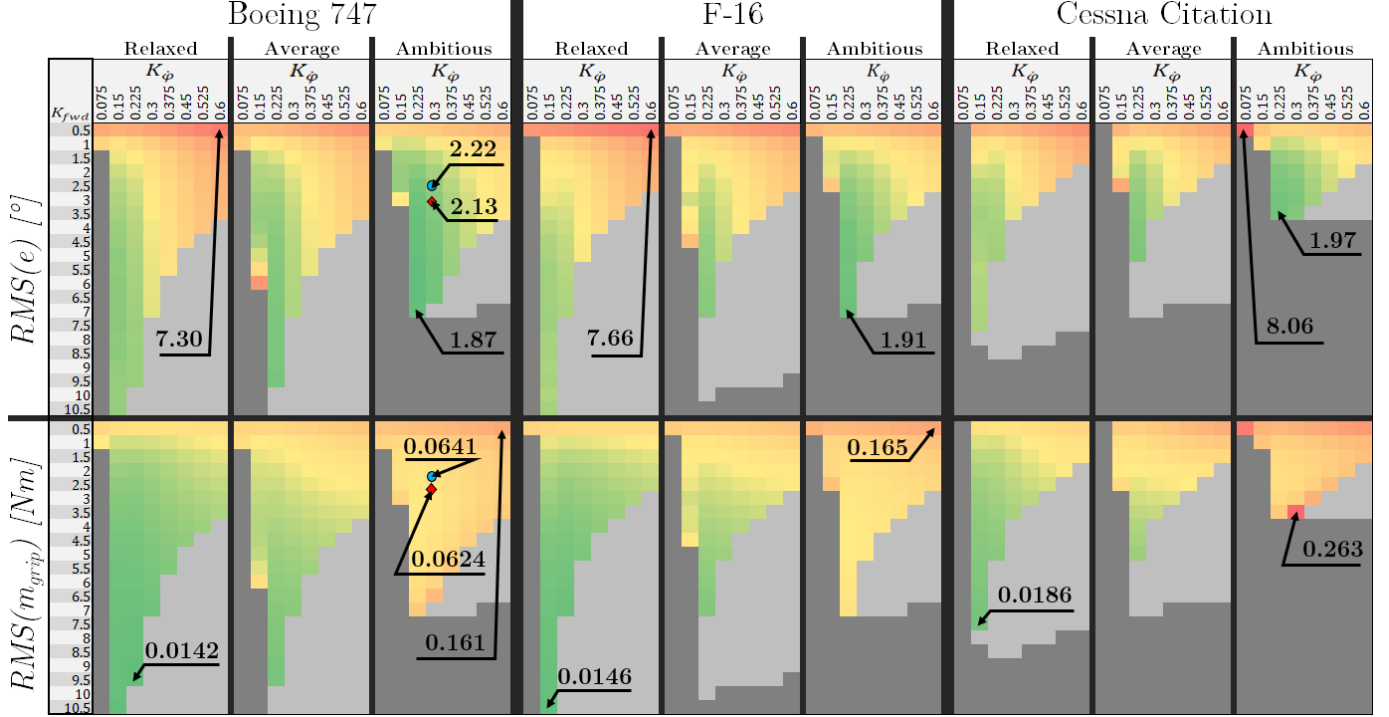


Figure 5. The simulation output of all model conditions, where the RMS of the error signal e is a measure for the tracking performance and the RMS of m_{grip} is a measure for the amount of control effort exerted by the pilot. To save space but maintain a decent impression of overall performance, only the highest and lowest values for $RMS(e)$ and $RMS(m_{grip})$ have been indicated in the heatmaps for most aircraft. The setting that Fu [12] tested at is indicated with a blue circle, to highlight how closely the hypothesized optimum (red diamond) was approached through trial and error in the simulator at the selected feedback gain of $K_{\phi} = 0.2857$.

C. Observations

While processing the simulation output, some of the model conditions in the heatmaps of Figure 5 have been blocked with two different shades of gray. This is done for the following reasons:

- Dark gray: unstable model condition. The value for which K_{fwd} causes system instability reduces as the pilot becomes more aggressive. Similarly, the minimum K_{ϕ} required for stability increases for a more aggressive control style.
- Light gray: model condition for which oscillations of extremely high frequency and intensity occurred in the system's signals. For many of these conditions, the system seemed to be able to track the target signal, however, this was realized using an $RMS(m_{grip})$ that was in the order of 10^3 larger than the largest values reported by Fu [12]. These results are clearly unrealistic and are, therefore, omitted from the heatmaps. The manipulator settings at which this oscillatory behavior occurred seemed to be independent of the pilot's control style, but were mostly affected by the CE dynamics.

Looking at Figure 5, several observations can be made. First, the value for K_{ϕ} that consistently produces the best results for all aircraft

in terms of tracking performance and control effort seems to hover at ≈ 0.225 . For all aircraft, a more aggressive control style does seem to make larger values for K_{ϕ} more viable in terms of tracking performance. In terms of control effort, however, an optimum appears for most aircraft when the pilot becomes more aggressive, which further supports an 'optimal' value for K_{ϕ} of ≈ 0.225 . Combining this point with the observation made about K_{ϕ} for the unstable model conditions, a human performance plateau is implied for this control configuration.

Second, for any given feedback gain, both the tracking performance and required control effort seem to improve for an increasing K_{fwd} (except for the situations with ambitious control styles, where $RMS(m_{grip})$ does increase), however, the added returns diminish as the oscillatory zone is approached. Whereas the practical consequences of entering this zone are unknown at this point, it is safe to assume that these conditions will result in system instability. Approaching this zone would thereby decrease stability margins. Selecting an 'optimal' K_{fwd} based on the model condition that resulted in the lowest $RMS(m_{grip})$ for an ambitious control style resulted in a safety factor of at least 1.5 for all aircraft before the oscillatory zone was reached, which was deemed acceptable for protecting pilots from destabilizing the system. As a result, the supposed optimal feed-forward gains became $(K_{fwd})_{opt,B747} \approx 3.5$, $(K_{fwd})_{opt,F16} \approx 4$ and $(K_{fwd})_{opt,CC} \approx 2$, respectively.

Third, the pilot seems to reap most (if not all) performance benefits from the active stick configuration as a relaxed controller already. Whereas there seems to be some tracking performance to be gained from having a more ambitious control style for the relatively slow responding B747, the pilot seems to be rewarded with diminishing tracking performance returns as the aircraft becomes faster / more nervous.

A possible explanation as to why $(K_\phi)_{opt}$ for the compensatory roll task seems to be largely independent of the CE dynamics and the pilot's control style can be found in the work from McRuer [14]. McRuer reported that pilots consistently adapt their control behavior $H_p(s)$ to produce the same open-loop dynamics $|H_p H_c| \approx \frac{\omega_c}{s}$, where the preferred gain crossover frequency ω_c was estimated to be around 4.75 rad/s for a compensatory tracking task in this control context (i.e., a side stick in pure lateral motion). Combining the pilot's tendency to shape the open-loop dynamics to become $\frac{\omega_c}{s}$ with the idea that $H_{c,eff}(s) = \frac{1}{K_\phi s}$, one could argue that for this control context $(K_\phi)_{opt} = \frac{1}{\omega_c} \approx \frac{1}{4.75} = 0.2105$, which is supported by the simulation output shown in Figure 5.

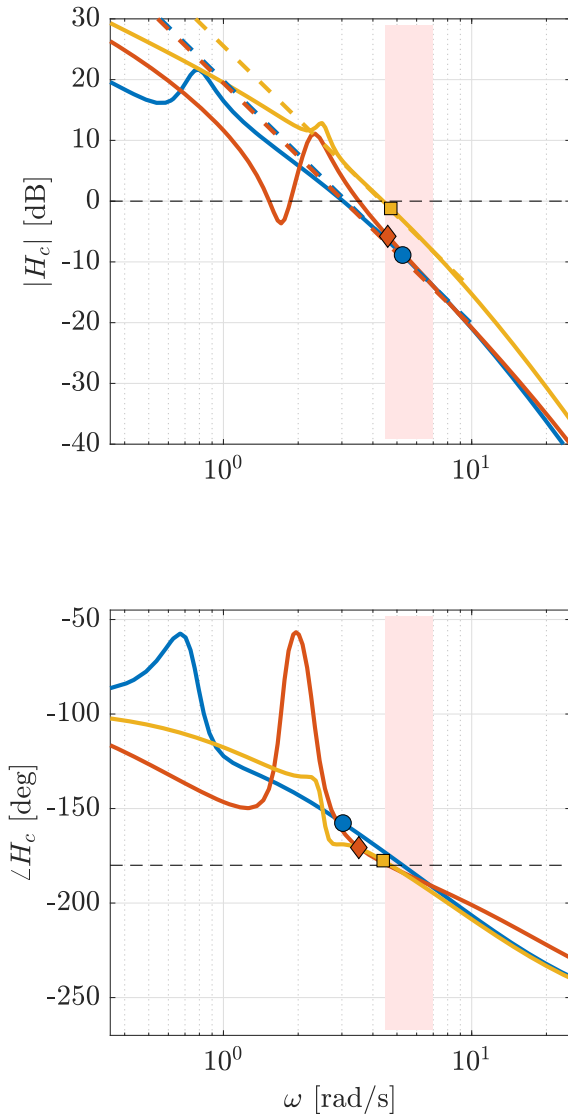


Figure 6. Bode plot of the roll dynamics and the accompanying gain and phase crossover points of the Boeing 747 (blue, circle), F-16 (red, diamond) and Cessna Citation (yellow, square). The highlighted area represents the crossover region related to this task ($\omega_c \approx 4.5 - 7$ rad/s) [18]. The second-order system approximations of $|H_c|$ for the three aircraft are indicated with dashed lines.

To determine why the simulations suggest a $(K_{fwd})_{opt}$ of about 3.5, 4 and 2 for the B747, the F-16 and the Cessna, respectively, a possible explanation could once again be found in the findings from McRuer [14]. McRuer determined that the character of the CE dynamics around the crossover region play a decisive role when designing for and assessing human performance in manual control tasks. Even though Equations 5, 7 and 9 show that the aircraft roll dynamics are all third-order systems, Figure 6 shows that the three aircraft dynamics all resemble second-order systems in the crossover region for this task, which means that pilots will likely compensate for controlling a second-order system. When the s^2 -term in the numerator of Equations 5, 7 and 9 is divided by the s^4 -term in the denominator of the same equations, the second-order systems that the respective aircraft resemble around this frequency domain can be approximated using $(H_c(s) = \frac{K_d}{s^2})$. This resulted in $K_{d,B747} = 9.800$, $K_{d,F16} = 9.346$ and $K_{d,CC} = 18.89$, which produced the approximations that are shown with dashed lines in Figure 6. The relation $K_d \cdot (K_{fwd})_{opt} = C_{fwd}$ could be a possible explanation as to why $(K_{fwd})_{opt,CC}$ is about half the value of the other two, with $(K_{fwd})_{opt,B747}$ being only slightly smaller than $(K_{fwd})_{opt,F16}$.

While the rationale behind the value for C_{fwd} is still unknown, a global minimum does seem to form for $RMS(m_{grip})$ for all aircraft, as the pilot's control behavior becomes more aggressive. Based on this argument, the simulation output would suggest that for CE dynamics resembling 1) *second-order* systems inside the crossover region related to 2) *this specific control context*, a value of $C_{fwd} \approx 37$ would be called for. While these findings leave something to be desired, there is a silver lining to be found when considering the work carried out by Fu [12]. After heuristically selecting a feedback gain ($K_\phi = 0.2857$), Fu selected K_{fwd} based on manual trial and error in the simulator, which resulted in the selection of $K_{fwd} = 2.5$. Looking at the bottom right matrix in Figure 5, one can notice how closely Fu was able to approach the simulated minimum for $RMS(m_{grip})$ given that feedback gain, with the closest simulated feedback gain ($K_\phi = 0.3$) resulting in $RMS(m_{grip}) = 0.0641$ Nm, while $(RMS(m_{grip}))_{opt} = 0.0624$ Nm for $K_\phi = 0.3$.

V. Method

Following the analysis from Section IV, the predicted effects of different CE dynamics as well as the haptic admittance display feed-forward and feed-back gains are put to the test in an experiment. First, hypotheses are formalized, which form the basis of the conditions to be tested. Afterwards, details are provided about the experiment design, along with a description of the envisioned data analyses.

A. Hypotheses

Based on the findings presented in Section II and at the end of Section IV, we expect that for a compensatory tracking task in a given control context (in this case defined as a side stick in lateral motion):

1. $(K_\phi)_{opt}$ is the inverse of ω_c , where $H_{Ol}(s) = \frac{\omega_c}{s}$ are the open-loop dynamics to which pilots prefer to converge in a passive manipulator configuration. As a result, $(K_\phi)_{opt}$ is hypothesized to be constant for a given control context.
2. $(K_{fwd})_{opt}$ is inversely proportional to K_d , where $H_d(s) = \frac{K_d}{s^2}$ approximates the CE dynamics as a simple X-th order system around the crossover region related to this control context.
3. $(K_{fwd})_{opt}$ can be determined using the simulated global minimum that forms for $RMS(m_{grip})$ as pilots adopt a more ambitious control style.

B. Experiment design

1 Apparatus: A target-following and disturbance-rejection compensatory tracking task highly similar to the one conducted by Fu [12] was tested in the HMI-lab at TU Delft. This was done using the hardware that is shown in Figures 7 and 8. Participants were tasked with minimizing the error angle e of the aircraft on the digital flight display, which effectively meant keeping the aircraft level with the virtual horizon. The error e came to be as a result of the difference between the target forcing function f_i and the current aircraft roll angle ϕ , while being perturbed by another forcing function f_d that represents turbulence.

The properties of these sinusoidal forcing functions, whose definitions are presented in Equations 1 and 2, are shown in Table 1. To maintain coherency with the work carried out before, these properties are identical to those of the low bandwidth signal tested by Fu [12].



Figure 7. The manipulator and liquid crystal display (LCD) screen that were used for the experiment [12].

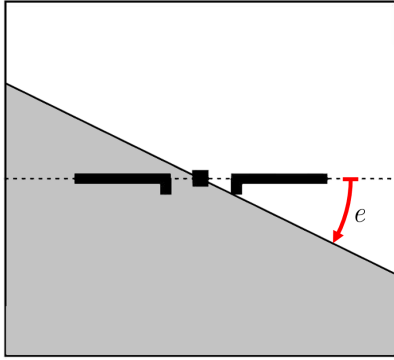


Figure 8. The simplified artificial horizon that participants saw on the LCD screen, which includes a clarification of e for the reader (modified image from Fu [12]).

Table 1. Properties of the target and disturbance forcing functions

k	f_t			f_d				
	Period	ω_t , rad/s	A_t , rad	Period	ω_d , rad/s	A_d , rad	ϕ_d , rad	
1	5	0.3835	0.1864	1.7411	6	0.4602	0.0242	1.2829
2	11	0.8437	0.0910	5.4434	13	0.9971	0.0102	0.9194
3	21	1.6107	0.0277	3.3194	23	1.7641	0.0097	1.8334
4	37	2.8379	0.0094	3.8945	38	2.9146	0.0084	2.5865
5	51	3.9117	0.0056	1.2212	53	4.0650	0.0090	1.5750
6	71	5.4456	0.0039	4.3954	73	5.5990	0.0120	3.7298
7	101	7.7466	0.0033	3.0397	103	7.9000	0.0215	1.5056
8	137	10.5078	0.0032	0.0160	139	10.6612	0.0413	3.1201
9	191	14.6495	0.0031	5.4767	194	14.8796	0.0934	1.0491
10	224	17.1806	0.0031	3.4525	227	17.4107	0.1407	4.8887

2 *Independent variables*: The experiment has three independent variables that are all tested at two levels: K_{fwd} , K_ϕ and the CE dynamics. For the two aircraft that are tested, the values for K_{fwd} and K_ϕ are based on what is deemed optimal by the hypotheses, and double of that value. Table 2 provides an overview of the six conditions that are tested by all participants. It should be noted that four additional conditions (indicated in yellow) were all intended to be tested by a subgroup of the participants. The findings with regards to these extra conditions are discussed in Section VII, after the findings of the first six are presented in Section VI.

Furthermore, Table 2 emphasizes that $(K_\phi)_{opt}$ is hypothesized to be constant and equal to 0.2105, as the control context is identical for both aircraft. As for the selection of the two aircraft, Section IV suggests that $(K_{fwd})_{opt}$ is quite similar for the B747 and the F-16, which is

why one of these two was deemed the most suitable candidate to disregard. The B747 made it through the aircraft selection, as it increases the coherency between this paper and the results generated earlier by Fu [12], which was done solely with said aircraft. As mentioned in Section IV, the optimal feed-forward gains that correspond with these aircraft are $(K_{fwd})_{opt,B747} = 3.5$ and $(K_{fwd})_{opt,CC} = 2$.

Table 2. All conditions that were tested before and during the experiment. Besides the six conditions that were tested by all participants, the four indicated in yellow were each intended to be tested by a subgroup of the participants only (see Section VII for more information).

Aircraft	K_ϕ	K_{fwd}		
		$(K_{fwd})_{opt}$	$2 \cdot (K_{fwd})_{opt}$	$3 \cdot (K_{fwd})_{opt}$
B747	$(K_\phi)_{opt}(= 0.2105)$	1	2	7
	$2 \cdot (K_\phi)_{opt}(= 0.4210)$	3	9	
Cessna	$(K_\phi)_{opt}(= 0.2105)$	4	5	8
Citation	$2 \cdot (K_\phi)_{opt}(= 0.4210)$	6	10	

3 *Procedure*: Twelve student volunteers, whose experience ranged from video games to glider pilot licenses, performed the six conditions shown in Table 2. For one half of the participants, the conditions of the B747 were first tested in a random order and for the other half the ones of the Cessna Citation, such that the twelve unique sequences resulting from this were all tested by one person. Afterwards, each participant would test the yellow condition that was assigned to them randomly. The document that was used to brief participants can be found in Appendix C.

Identical to the way the previous experiment was conducted and the current one was modeled, participants conducted runs of 90 seconds for every condition, of which the last 81.92 seconds was used for analysis to negate any transient effects from the signal ramp-up. Participants were tasked with minimizing the $RMS(e)$, which was read out to them after every run to keep them involved and motivated. For every condition, runs of 90 seconds were added until the tracking performance stabilized for five consecutive runs, leading to an average of eight runs per condition. Consequently, the measurements of only the last five runs for every condition were used for the final analysis.

C. Data analysis

During the experiment, measurements of the aircraft's roll angle (ϕ), the forcing functions (f_t and f_d) as well as the force exerted by the pilot on the manipulator (m_{meas}) were recorded at a sampling frequency of 100 Hz. Using these measurements, as well as two signals that were derived from this ($e = f_t - \phi$ and $u_p = K_{fwd} \cdot m_{meas}$), various analyses were conducted.

1 *Time domain*: the overall performance of the participants is assessed in terms of 1) one's ability to track the target and 2) the amount of effort it took. The tracking performance is assessed by calculating $RMS(e)$ and the exerted control effort is quantified using $RMS(m_{meas})$.

2 *Frequency domain*: the use of multisine forcing functions allows for the identification of the participant's frequency responses to f_t and f_d at the frequencies $j\omega_t$ and $j\omega_d$, respectively. This results in FRFs for the target tracking open-loop ($H_{iOL}(j\omega_t) = \frac{\phi(j\omega_t)}{E(j\omega_t)}$) and closed-loop response ($H_{iCL}(j\omega_t) = \frac{\phi(j\omega_t)}{F_t(j\omega_t)}$), as well as the disturbance rejection open-loop response ($H_{dOL}(j\omega_d) = \frac{U_p(j\omega_d)}{U(j\omega_d)}$). As is argued by Fu [12] and supported by Figure 4, the CE dynamics are by default present in the numerator of the disturbance rejection closed-loop response, which does not make it straightforward to interpret the impact of f_d on ϕ . Therefore, the following adjustment is made:

$$|H_{dCL}(j\omega_d)| = \left| \frac{\phi(j\omega_d)}{F_d(j\omega_d)} / H_c(j\omega_d) \right| \quad (10)$$

$$\angle H_{dCL}(j\omega_d) = \angle \frac{\phi(j\omega_d)}{F_d(j\omega_d)} - \angle H_c(j\omega_d) \quad (11)$$

The RMS -values as well as the crossover characteristics that result from the Fourier analysis are tested for normality using the Kolmogorov - Smirnov (K-S) test, after which all variables that passed

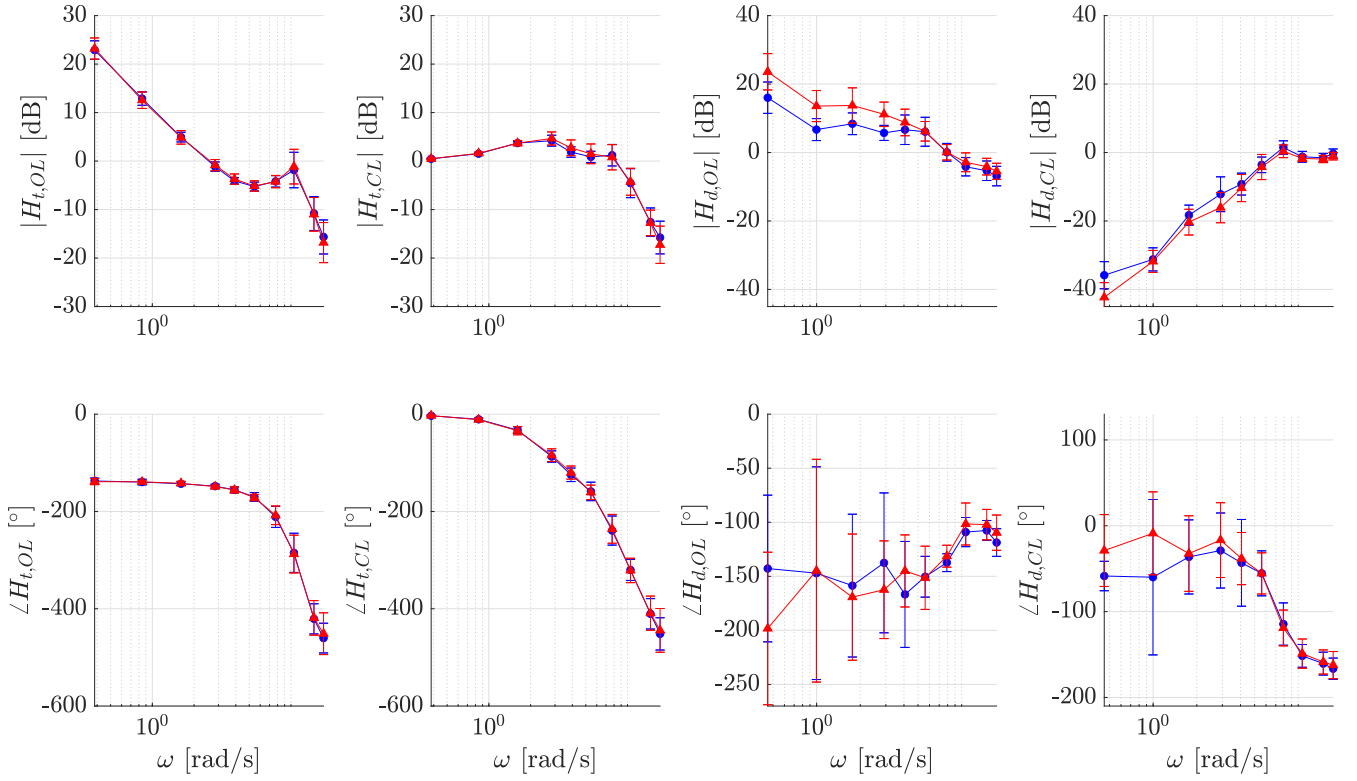


Figure 9. All FRFs related to Conditions 2 (blue circle) and 5 (red triangle). All values are reported as mean \pm std. deviation.

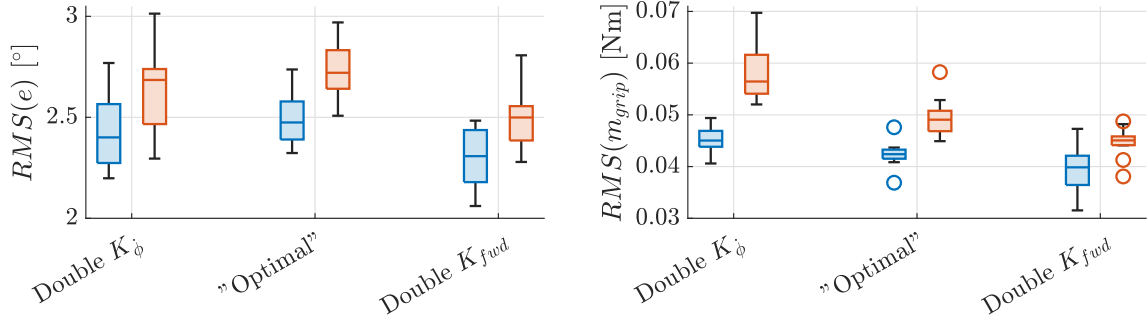


Figure 10. The RMS values of the tracking error e and the grip moment m_{grip} for all B747 (blue, left) and Cessna Citation (red, right) conditions.

the test are subjected to two different two-way analyses of variance (ANOVAs): one investigating the variable pair (CE dynamics / K_{fwd}) and the other the pair (CE dynamics/ K_{ϕ}). Whenever a variable cannot be considered as normally distributed for at least one of the tested conditions, a Friedman's ANOVA is conducted and a Wilcoxon signed-rank test is used to check for significant differences between the relevant conditions. Furthermore, it should be noted that all these variables have been corrected for between-subject variability.

VI. Experiment results

Figure 9 shows all FRFs related to Conditions 2 and 5, such that the reader can get a general impression of the pilot's control behavior. Appendix D can be consulted to get a complete overview, as it compares the FRFs of all conditions in all possible combinations that can be of interest. The values that represent the overall performance, target tracking crossover characteristics and disturbance rejection crossover characteristics for Conditions 1 to 6 are shown in Figures 10, 11 and 12, respectively.

All variables were found to be normally distributed, except for $RMS(m_{grip})$ and $\omega_{c,d}$. These variables produced a significant K-S test for one and three of the six testing conditions, respectively. This is why their effects are not presented among the ANOVA significance tests from Table 3, but are presented separately using non-parametric tests in Table 4 instead.

A. Tracking error and exerted control effort

When looking at Figure 10 and Tables 3 and 4, several things stand out. One of the strongest main effects here is related to the conditions with a double K_{fwd} , which resulted in a significantly lower $RMS(e)$ than their single K_{fwd} counterparts. To a lesser extent, $RMS(e)$ also reduced significantly by flying the slower / more stable B747, and for the conditions that used a double K_{ϕ} as opposed to their single K_{ϕ} counterparts.

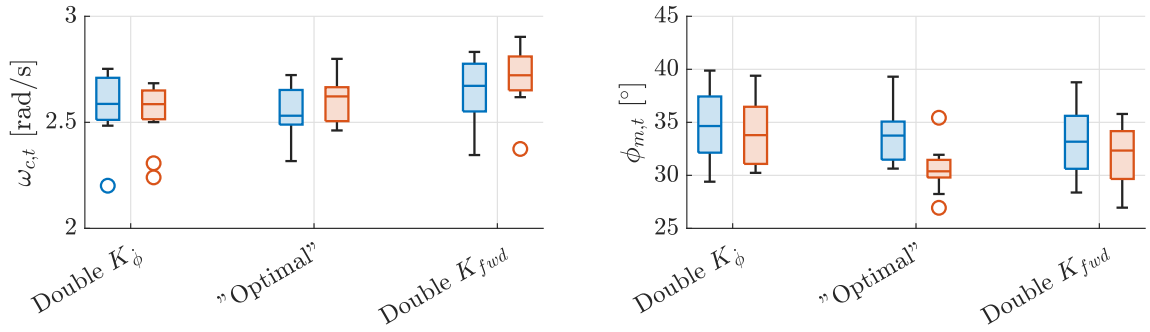
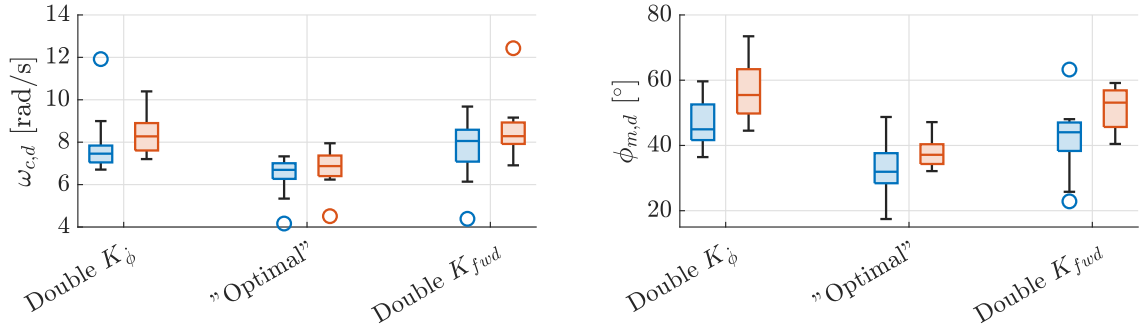
Regarding the exerted control effort, the Wilcoxon signed-rank tests following the significant Friedman ANOVA in Table 4 show that having a faster / more nervous aircraft significantly increased the amount of control effort exerted by the pilot. Furthermore, a double K_{ϕ} also resulted in a significantly higher exerted control effort. Interestingly, the exerted control effort significantly reduced to an equally great extent for the conditions with a double K_{fwd} .

Summarizing the findings with respect to the time-domain performance metrics, it seems that faster / more nervous CE dynamics reduce the pilot's tracking performance while also making the task more demanding. A double feed-back gain improves tracking performance somewhat, however it comes at a clear cost in terms of increased control effort / reduced user comfort, which was supported by participants consistently referring to Conditions 3 and 6 as more 'difficult', 'jerky', 'erratic' and 'hectic'. A double feed-forward gain, on the other hand, seems to provide significant benefits, both in terms of tracking performance and exerted control effort.

Table 3. Significance tests for the ANOVAs conducted for the time domain metrics and the target tracking and disturbance rejection crossover characteristics

			A/C type	K_{fwd}	K_ϕ	A/C type * K_{fwd}	A/C type * K_ϕ
Tracking performance	$RMS(e)$	F value	F(1,11)	F(1,11)	F(1,11)	F(1,11)	F(1,11)
		Significance	8.775	28.202	8.465	0.794	0.091
				$p < 0.05$	$p < 0.05$	$p > 0.05$	$p > 0.05$
Target tracking crossover characteristics	$\omega_{c,t}$	F value	F(1,11)	F(1,11)	F(1,11)	F(1,11)	F(1,11)
		Significance	0.028	10.520	0.102	0.000	1.992
				$p > 0.05$	$p < 0.01$	$p > 0.05$	$p > 0.05$
	$\phi_{m,t}$	F value	F(1,11)	F(1,11)	F(1,11)	F(1,11)	F(1,11)
Significance		2.740	0.107	6.218	1.605	8.395	
			$p > 0.05$	$p > 0.05$	$p > 0.05^a$	$p > 0.05$	$p < 0.05$
Disturbance rejection crossover characteristics	$\phi_{m,d}$	F value	F(1,11)	F(1,11)	F(1,11)	F(1,11)	F(1,11)
		Significance	7.994	16.946	51.595	1.018	3.204
			$p < 0.05$	$p < 0.01$	$p < 0.01$	$p > 0.05$	$p > 0.05$

^a This significance value changed from $p < 0.05$ to $p > 0.05$ after a Bonferroni correction had been applied.

**Figure 11. The target tracking gain crossover frequency $\omega_{c,t}$ and phase margin $\phi_{m,t}$ for all B747 (blue, left) and Cessna Citation (red, right) conditions.****Figure 12. The disturbance rejection gain crossover frequency $\omega_{c,d}$ and phase margin $\phi_{m,d}$ for all B747 (blue, left) and Cessna Citation (red, right) conditions**

B. Target tracking crossover characteristics

As for the target tracking crossover characteristics shown in Figure 11, there are fewer identified effects. The strongest effect to be noted here is the significant increase of $\omega_{c,t}$ as a result of having a double K_{fwd} . For the phase margin $\phi_{m,t}$, only a significant interaction was found between the aircraft type and K_ϕ . Upon closer inspection using paired-sample T-tests, it was concluded that no significant main effect was found for the CE dynamics nor K_ϕ with respect to $\phi_{m,t}$ (see Table 5).

To summarize, the target tracking crossover characteristics remain largely unaffected by variations in the CE dynamics and K_ϕ , however, a double K_{fwd} does significantly increase $\omega_{c,t}$. Furthermore, there seems to be an interaction between the CE dynamics and K_ϕ , which implies that the faster / more nervous the CE dynamics become, the more disadvantageous having a single K_ϕ is for the phase margin $\phi_{m,t}$. Besides that, no main effects are found for $\phi_{m,t}$.

C. Disturbance rejection crossover characteristics

When comparing the vertical axes of Figures 11 and 12, it becomes apparent that the different testing conditions resulted in a much greater variation in the pilot's ability to reject disturbances as opposed to the ability to track the target signal. For $\omega_{c,d}$, two main effects are identified. As can be seen in Table 4, $\omega_{c,d}$ increases significantly for a double K_{fwd} as well as a double K_ϕ . The CE dynamics, on the other hand, seem to have no significant effect on this parameter. For $\phi_{m,d}$, no significant interactions are found. However, a double K_{fwd} , a double K_ϕ and faster / more nervous CE dynamics all significantly increase $\phi_{m,d}$.

To summarize, the disturbance rejection phase margin $\phi_{m,d}$ increases for faster / more nervous CE dynamics. But more importantly, doubling either K_{fwd} or K_ϕ significantly increases $\omega_{c,d}$ and $\phi_{m,t}$, which is a finding that seems counter-intuitive. This remarkable result can be explained by the working principle of the active manipulator. As can be seen in Figure 4, the pilot's control response (u_p) to disturbances

incurred on the aircraft (f_d) is the result of 1) a relatively slow, cognitive response and 2) a neuromuscular response that is comprised of a) a fast, reflexive response and b) an instantaneous response, thanks to the intrinsic mechanical properties of the arm. For disturbances below the crossover region, pilots are able to register and respond adequately to what they feel and will therefore take conscious actions. As a result, the cognitive contribution to the rejection of disturbances imposes its relatively large time delay on the FRF. This is supported by the disturbance rejection open-loop phase plots of Conditions 2 and 3 shown in Figure 13, which reports mean phase angles of $\approx -140^\circ$ to -160° up to the crossover region related to this task.

Table 4. Friedman’s ANOVA and the following Wilcoxon’s signed-rank tests for the non-normally distributed variables $RMS(m_{grip})$ and $\omega_{c,d}$. The independent variables that had a significant effect on their dependent variable across all comparisons are indicated in bold.

Dep. var. with Friedman statistic	Indep. var.	Co. pair	Mdn 1	Mdn 2	z	p
$RMS(m_{grip})$, $\chi^2(5) = 45.619$, $p < 0.01$	A/C type	1-4	0.04239	0.04906	-3.059	$p < 0.01$
		2-5	0.03986	0.04506	-2.589	$p < 0.01$
		3-6	0.04503	0.05645	-3.059	$p < 0.01$
	K_{fwd}	1-2	0.04239	0.03986	-2.197	$p = 0.028$
		4-5	0.04906	0.04506	-2.510	$p = 0.012$
	K_ϕ	1-3	0.04239	0.05645	-2.275	$p = 0.023$
4-6		0.04906	0.05645	-2.981	$p < 0.01$	
$\omega_{c,d}$, $\chi^2(5) = 29.333$, $p < 0.01$	A/C type	1-4	6.695	6.873	-1.647	$p = 0.099$
		2-5	8.056	8.283	-1.098	$p = 0.272$
		3-6	7.459	8.274	-1.961	$p = 0.050$
	K_{fwd}	1-2	6.695	8.056	-2.197	$p = 0.028$
		4-5	6.873	8.283	-2.981	$p < 0.01$
	K_ϕ	1-3	6.695	7.459	-2.824	$p < 0.01$
4-6		6.873	8.274	-2.903	$p < 0.01$	

Table 5. The paired-samples T-tests that show that neither the aircraft type nor K_ϕ is a main effect for $\phi_{m,d}$. The 2-tailed p-values are reported after having applied a Bonferroni correction for the comparisons.

Isolated effect	Co. pair	Paired differences					p (2-tailed)
		Mean	σ	95% CI		t(11)	
A/C type	1-4	3.321	3.645	1.005	5.637	3.156	< 0.05
	3-6	0.5292	4.975	-2.632	3.690	0.368	> 0.05
K_ϕ	1-3	-0.8802	3.239	-2.938	1.178	-0.941	> 0.05
	4-6	-3.672	3.883	-6.139	-1.205	-3.276	< 0.05

Continuing with Figure 13, a transition can be observed around the crossover region inside the phase plot, as the pilot’s inability to consciously respond to faster disturbances gradually delegates a larger portion of the disturbance rejection task to the much faster NMS, effectively increasing $\phi_{m,d}$. Finally, for frequency components well past the crossover region ($\omega > 10$ rad/s), the role of the cognitive response seems to have been eliminated entirely from the disturbance rejection task. An increase in either K_{fwd} or K_ϕ encourages a more aggressive response to the injected disturbances, which interestingly seems to make the pilot delegate a larger portion of the disturbance rejection task to the faster NMS, thereby increasing both $\omega_{c,d}$ and $\phi_{m,d}$. Judging from the divergent verbal feedback that participants gave regarding user comfort for conditions 2/5 and 3/6, it seems that one can use the neuromuscular potential to reject disturbances more effectively either subconsciously or forcibly, by increasing K_{fwd} or K_ϕ , respectively.

Given the idea that the NMS seems to play a dominant role for

rejecting disturbances beyond a certain frequency (in other words, $H_{dOL}(s) \approx H_c(s)K_\phi H_{lpf}(s)H_{NMS,x_m}(s)K_{fwd}$ beyond that frequency), another observation could be made when comparing the Condition pairs 2/3 and 5/6. As can be seen in Figure 13, the FRFs for the conditions of double K_{fwd} and double K_ϕ seem to converge beyond the crossover region. This supports the notion that the NMS can be modelled accurately as a linear system, or at the very least that the neuromuscular response to x_m can be modelled as such.

Based on the same idea, it also becomes straightforward to explain why the disturbance rejection open-loop phase plots for the Cessna Citation in and beyond the crossover region have a minor, but consistently larger value than their B747 counterparts (see Figure 9). Faster CE dynamics effectively form a smaller time delay between the moment some turbulence f_d is applied and the moment the NMS can respond to it through the haptic cues presented by x_m , thereby increasing $\phi_{m,d}$.

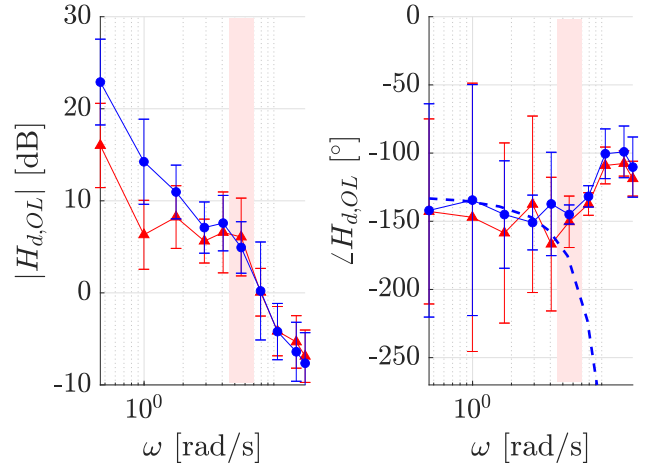


Figure 13. Disturbance rejection open-loop FRF of conditions 2 (red triangle) and 3 (blue circle), reported as mean \pm std. deviation. The average $\angle H_{dOL}$ of condition 3 has been plotted in dashed blue as well, to highlight how $\angle H_{dOL}$ follows a trajectory in and beyond the highlighted crossover region that is different from the phase plot related to the conventional compensatory tracking task that relies purely on a cognitive (visual) response from the pilot.

VII. Additional experimental findings

Based on the observations from Section VI, increasing K_{fwd} and K_ϕ seems to provide significant performance gains (with the exception of a higher K_ϕ increasing exerted control effort), without sacrificing anything in terms of stability margins. This poses the obvious question: how far can these settings be pushed for performance gains?

To shed light on this question, it is worth mentioning that four additional settings were intended to be tested at the time that the conducted experiment was being prepared (see Table 2). Each participant would try to complete one of these four conditions in the same way as the previous six conditions, at the very end of their session. In doing so, some additional insights could be generated regarding the consequences of setting the gains at values that correspond with the light gray conditions shown and explained in Figure 5 and Section III, respectively.

A. Initial tests

After running initial tests, it became evident that Conditions 9 and 10 (i.e., the setting of $(2 \cdot (K_{fwd})_{opt}, 2 \cdot (K_\phi)_{opt})$ for the B747 and the Cessna Citation, respectively) resulted in an unworkable situation. While the control task itself did not seem impossible at these settings, the side stick would very easily start to resonate in the user’s fist, causing the servos that drive the manipulator to shut down out of self-protection.

The aforementioned Conditions 9 and 10 were located well inside the light gray oscillatory domains from Figure 5, however the same could not be said about Conditions 7 and 8. For both the B747 and the Cessna, this setting of $(3 \cdot (K_{fwd})_{opt}, 1 \cdot (K_\phi)_{opt})$ was near or at the transition point to the oscillatory domain. While some stick vibrations were registered, these two conditions were deemed suitable to be tested by six of the twelve participants each.

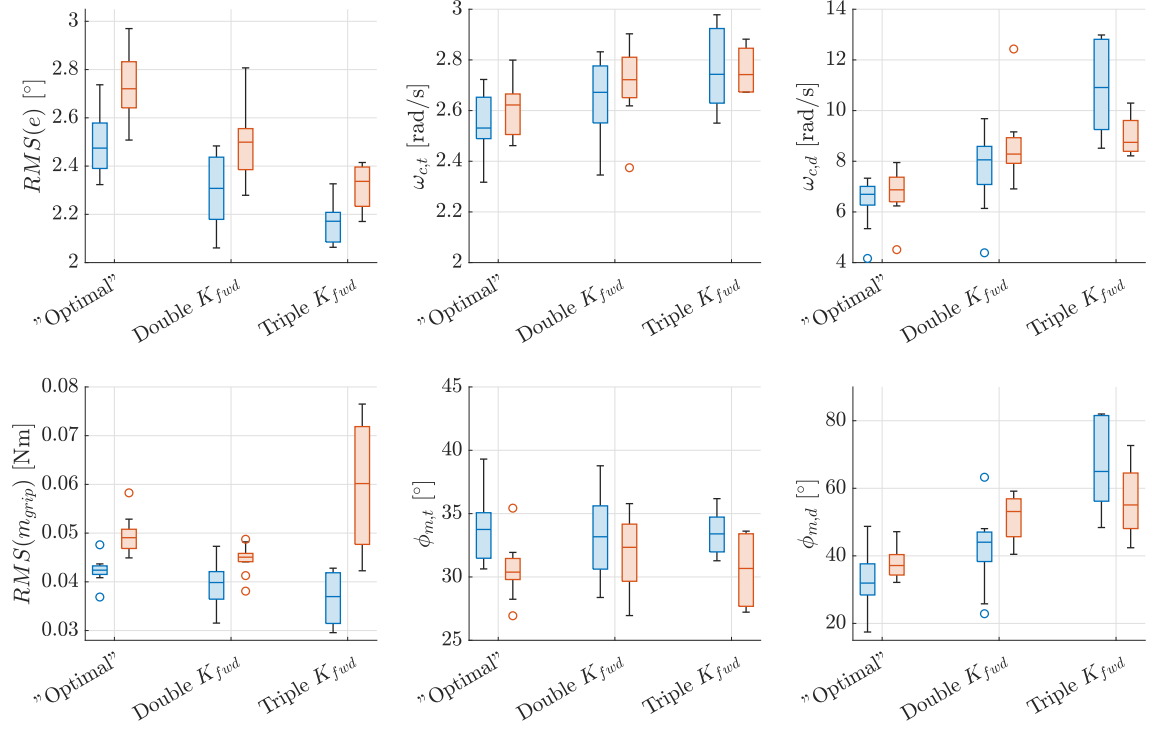


Figure 14. Boxplots that characterize pilot performance for the B747 Conditions 1, 2 and 7 (blue) and the Cessna Citation conditions 4, 5 and 8 (red).

B. Experimental data from participants

For the B747, all six participants successfully completed the condition with a triple K_{fwd} . Moderate vibrations were registered during a single run of one participant, while another participant reported to feel minor vibrations in the stick. For the Cessna, the condition was aborted for two out of six participants, due to the same, excessive vibrations that were experienced while trying out Conditions 9 and 10. The remaining four participants successfully finished the triple K_{fwd} condition, of which two did so while having endured considerable vibrations throughout many of the runs. Consequently, the experimental output of Conditions 7 and 8 that is shown in Figures 14 and 15 is generated from six and four samples, respectively, as opposed to the others that were derived from all twelve participants.

As can be seen in Figure 14, the trends that were identified in Section VI are largely continued here, particularly for the B747. For this aircraft, the triple K_{fwd} provides a moderate increase to $\omega_{c,d}$ while $\phi_{m,d}$ remains largely unaffected. Furthermore, $\omega_{c,d}$ and $\phi_{m,d}$ continue to increase as we move from the case of double K_{fwd} to triple K_{fwd} . Evidently, $RMS(m_{grip})$ was greatly affected for the triple K_{fwd} condition of the Cessna due to the present stick vibrations. At the same time, the trends for the crossover characteristics of the Cessna seem to flatten out somewhat as we move from the case of double K_{fwd} to triple K_{fwd} .

Whereas the metrics from Figure 14 suggest that the pilot's performance is equally good or considerably better in every regard when we move from the case of double K_{fwd} to triple K_{fwd} for the B747, they fail to provide any information about the looming instability of the stick. However, the disturbance rejection FRFs of Conditions 1/2/7 and 4/5/8 do provide a possible indication for the stick instability that seems to be the limiting factor of this control configuration. When looking at Figure 15, the area of interest is that of $|H_{dOL}(s)|$ well beyond the crossover region ($\omega > \approx 10$ rad/s). To reiterate the information shown in Figure 4, this transfer function describes how the disturbance rejection loop behaves, by calculating the pilot's control response u_p (which is formed by a cognitive and neuromuscular response) to a disturbance signal introduced at u .

As was discussed in Section VI, pilots lack the ability to respond consciously to signals well beyond the crossover region. Looking at

Figure 4, one can imagine how a value for $|H_{dOL}(s)|$ that is greater than 0 dB in a frequency band where the cognitive feed-back loop is eliminated could lead to indefinite amplification of disturbance signals in the neuromuscular feed-back loop. Pilots can mitigate this problem by relaxing their grip and reducing the level of muscle co-contraction, effectively maximizing their neuromuscular admittance. The consequence of such an action is demonstrated with the difference between $|H_{d,OL,B747}|$ and $|H_{d,OL,CC}|$ beyond the crossover region in Figure 15. A clear trend is visible in the shape of $|H_{d,OL,B747}|$ where participants were virtually unaffected by stick vibrations, while $|H_{d,OL,CC}|$ shows a clear regression back towards the disturbance rejection response of the double K_{fwd} condition to combat the stick vibrations.

Evidently, there is a limit to the extent with which pilots can relax their arm. If K_{fwd} , $K_{\dot{\phi}}$ or likely a product of the two is increased sufficiently (as supported by the similarities between Conditions 2 and 3 for $|H_{dOL}(s)|$ for $\omega > 4.5$ rad/s in Figure 13), this could mean that the NMS can no longer prevent the high-frequency disturbances from amplifying indefinitely. This lines up with the observations made during the experiment, as participants who were forced to abort their runs due to excessive vibrations did not seem to struggle with the control task at hand, but were rather surprised about the stick's sudden failure instead.

Summarizing these findings, it seems that the neuromuscular response plays a decisive role in determining how far the active manipulator's settings can be pushed for performance gains. Another question that could be asked at this point is: why did the triple K_{fwd} condition for the Cessna Citation result in considerable vibrations, while the triple K_{fwd} condition for the B747 narrowly seemed to avoid them? A possible explanation can be found when combining two earlier findings:

1. The values found for $K_{d,B747}$ ($= 9.800$) and $K_{d,CC}$ ($= 18.89$) at the end of Section IV, which approximate the CE dynamics of the respective aircraft in the crossover region as $H_c(s) = \frac{K_d}{s^2}$.
2. One of the observations made in Figure 13, which discusses the similarity of $H_{d,OL}(s)$ beyond the crossover region for the conditions with a double K_{fwd} and a double $K_{\dot{\phi}}$.

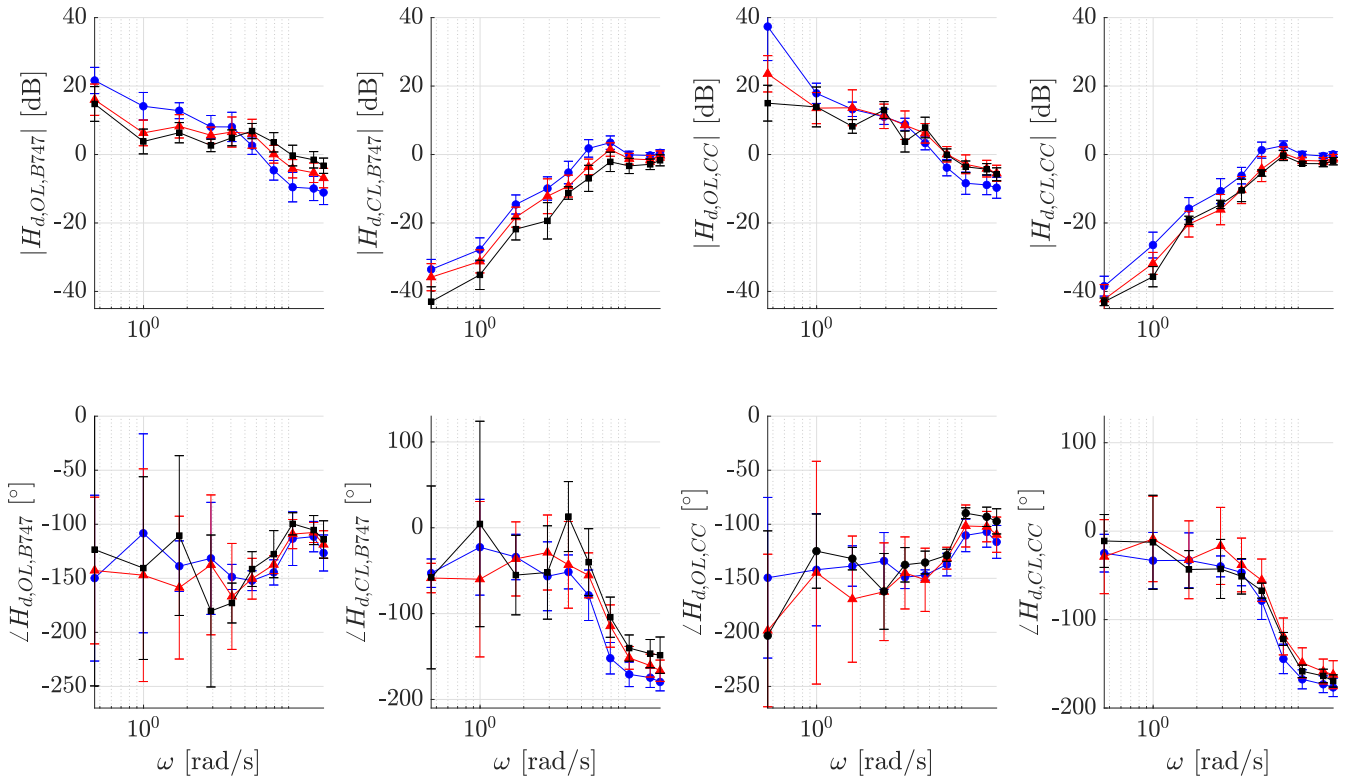


Figure 15. Open- and closed-loop disturbance rejection FRFs for the B747 Conditions 1, 2 and 7 (left) and the Cessna Citation Conditions 4, 5 and 8 (right), all reported as mean \pm std. deviation. The cases of single, double and triple K_{fwd} are indicated in blue circles, red triangles and black squares, respectively.

Whereas the relation $K_d \cdot (K_{fwd})_{opt} = C_{fwd}$ was already suggested in Section IV, it seems that the combined open-loop gain of the hardware (i.e., the relation $K_d \cdot K_{fwd} \cdot K_\phi = C$) can be a possible indicator of the system's stability margin with respect to the stick vibrations. Filling in this equation for the tested conditions gives:

- Conditions 1-6: $7.220 < C < 15.90$. No issues observed with regards to stick vibrations.
- Condition 7: $C = 21.66$. The earliest signs of stick vibrations started to appear for a few participants.
- Condition 8: $C = 23.86$. Considerable to severe vibrations were experienced by the majority of the participants.
- Conditions 9 and 10: $C = 28.88, C = 31.81$. Unworkable settings with regards to stick vibrations.

VIII. Discussion

Based on the findings presented in Sections VI and VII, we can reflect on the hypotheses from Section V, propose a tuning procedure and make suggestions for future research.

A. Reflection on hypotheses

Hypothesis 1 stated that $(K_\phi)_{opt}$ is constant for a given control context, as it would be based on the open-loop dynamics to which pilots prefer to converge for that control context. The experimental data from Section VI support this hypothesis, as the condition with a double K_ϕ for both aircraft resulted in significantly more exerted control effort, which was confirmed by participants consistently referring to these conditions as the least comfortable.

Hypothesis 2 stated that $(K_{fwd})_{opt}$ is inversely proportional to K_d , where $H_{OL}(s) = \frac{K_d}{s^X}$ approximates the CE dynamics as a simple X-th order system in the crossover region related to this control context. As such, a certain interaction between the aircraft type and $(K_{fwd})_{opt}$ was inferred when quantifying the testing conditions from Table 2. The fact

that no statistically significant interactions were found between the aircraft type and K_{fwd} (as can be seen in Table 3) supports the idea that the right interaction was inferred between said variables when defining the testing conditions. It should be noted that the validity of this hypothesis is supported within the scope of this paper, which has only tested CE dynamics that resemble *second-order* dynamics in the crossover region.

Hypothesis 3 stated that for a given control context, the value for $(K_{fwd})_{opt}$ can be determined using the simulated global minimum that forms for $RMS(m_{grip})$ as pilots adopt a more ambitious control style. This hypothesis proved to be incorrect, as participants consistently performed better with reduced effort for situations where a double K_{fwd} was applied. While the premise with which $(K_{fwd})_{opt}$ was selected may have been invalid in the first place, the model's inability to point us to the right $(K_{fwd})_{opt}$ has a variety of possible causes as well:

1. The parameters that define the NMS model from De Vlugt [15] (i.e., mechanical properties, proprioceptor gains and neural activation / transportation dynamics) need to be identified for a specific control context. The collective work of several researchers has enabled the quantification of this NMS model for a side stick in lateral motion, however the need for multiple sources increases the probability that some coefficients are defined inaccurately.
2. The components inside the NMS model are all defined as linear mass-spring-damper systems, whose gains were scaled up or down linearly as the pilot was simulated to have a more ambitious control style. This approach may have proven ineffective for predicting the actual neuromuscular response.
3. The pilot's cognitive equalization of the visually perceived error e was modelled using a simple PID-controller, which may have rendered the model ineffective at predicting pilot performance accurately as well.

While Hypothesis 3 provided an argument for a possible value of $(K_{fwd})_{opt}$, it would have called for a very cumbersome and impractical design procedure if its validity was supported by the data. Fortunately, the observations described in Section VII and illustrated in Figure 15 suggest that there may be a tangible and practical indicator in $|H_{dOL}(s)|$ for the maximum value that can be set for K_{fwd} , which enables designers of such a system to select $(K_{fwd})_{opt}$ in a way that acceptable stability / safety margins are achieved.

Despite the fact that the model did not live up to its full potential, it was reasonably well able to predict the settings at which the stick started to produce vibrations that could not be controlled. As explained in Section IV, it produced realizations for these conditions that seemed to be stable in terms of tracking performance at first sight, albeit that they were realized with control signals of extremely high frequency and intensity.

B. Proposed tuning procedure

After reflecting on the stated hypotheses, the following tuning procedure is proposed for control systems involving an active manipulator:

1. For a given control context, determine $(K_{\phi})_{opt}$ first:
 - (a) Perform a single integrator CE dynamics ($H_c(s) = \frac{K_c}{s}$) compensatory tracking task with a passive manipulator, similar to McRuer's experiment [14].
 - (b) Determine the average crossover frequency ω_c to which pilots prefer to converge for various values of K_c . While McRuer showed that ω_c varied relatively little for different forcing function signal bandwidths [14], one could test for this parameter as well to gain additional confidence in the value found for ω_c .
 - (c) Calculate $(K_{\phi})_{opt} = \frac{1}{\omega_c}$.
2. Then, for a given control context and some CE dynamics:
 - (a) Determine $(K_{fwd})_{opt}$ heuristically through trial and error in the simulator. $(K_{fwd})_{opt}$ is found once the desired maximum value for $|H_{dOL}(s)|$ is achieved in the frequency band well beyond the crossover region.
 - (b) From this value, $(K_{fwd})_{opt}$ can be inferred for other CE dynamics that are of comparable character in the crossover region of said control context.

An important caveat to add to Step 2a of the procedure is that $|H_{dOL}(s)|$ (and thereby the system's stability / safety margin) seems to be quite heavily dependent on the control style of the pilot. This provides designers of such a system with a challenge that is threefold:

1. The accurate quantification of a pilot's control intensity. The most straightforward solution for this challenge seems to be the use of measurements that record the clamping force that a pilot exerts on the manipulator, as this metric can be related directly to the pilot's neuromuscular admittance [27].
2. The decision which pilot (i.e., which neuromuscular response) should be considered the benchmark. This challenge can be overcome by performing measurements of neuromuscular admittance for the control context at hand, amongst a pool of pilots that are deemed fit for the task. Based on this, a pilot who can achieve a low (if not the lowest) neuromuscular admittance can be selected to act as the benchmark.
3. The formulation of appropriate stability / safety margins using the quantification that the designer has defined at point 1. For the suggestion mentioned at point 1, this could for instance translate to the requirement that " $|H_{dOL}(s)|$ shall be no larger than -3 dB well beyond the crossover region, given that maximum clamping force is applied by the pilot", where a representative pilot has been selected methodically through a process like the one described in point 2.

C. Recommendations

Based on the findings from this paper, numerous recommendations can be made for future research in the field of active manipulators. First off, a fixed-base simulator was used in this paper to gather insights, meaning this situation is most comparable to that of a pilot remotely controlling a drone from the ground. When the pilot is on board the aircraft that he or she controls, the motion of the vehicle can cause the pilot to provide involuntary control commands to the manipulator, a process that is also known as biodynamic feedthrough [28]. After a feasibility study has been conducted for the active manipulator configuration in an on-board setting, the proposed tuning procedure could be put to the test in such a context as well.

Furthermore, the requirement that " $|H_{dOL}(s)|$ shall be no larger than -3dB well beyond the crossover region" which was introduced at the end of Section VIII B calls for further clarification. As $|H_{dOL}(s)|$ decreases inside and beyond the crossover region, the "well beyond" in this sentence needs to be defined more accurately, as it currently does not provide a conclusive answer as to what exactly is deemed acceptable.

Regarding the degrees of freedom within the design of the active manipulator, several topics can be investigated. Firstly, the hypothesized main predictor for $(K_{\phi})_{opt}$, namely the control context (which in our case was defined as a side stick in lateral motion) should be put to the test. This can be done either using a pitch/(roll) tracking task or using a different manipulator, such as a yoke or a steering wheel. Secondly, while it is hypothesized that $(K_{fwd})_{opt}$ and $(K_{\phi})_{opt}$ are not dependent on each other, this can be put to the test in a future experiment as well. Thirdly, the validity of Hypothesis 2 can be tested for CE dynamics that resemble first- or third-order systems in the crossover region of a given control context. If valid at all, one could also determine in what way (if any) C_{fwd} would change as the conventional, effectively experienced system order is altered.

Another factor that could be considered in future research is the effect of slower actuator dynamics on the control response of the pilot. The servo used for this experiment had a bandwidth of around 40 Hz ($\omega \approx 250$ rad/s), which is a frequency around fourteen times higher than that of the fastest component in the used forcing functions ($\omega_d [10] = 17.4107$ rad/s). While it is expected that a servo bandwidth of less than five times the highest forcing function frequency component will result in a noticeable drop of $\angle H_{dOL}(s)$ in the high frequency band, it is unknown whether such a loss in phase will result in reduced user comfort or instability of the disturbance rejection loop.

Besides these recommendations that are directly applicable to the functioning of the active manipulator, more research can also be done with respect to the interrelation between the pilot's response to the visually perceived error ($H_e(s)$) and the haptic cues ($H_r(s)$). In previous research, these control responses have been defined as separate dynamical systems [12]. While this is convenient from a system identification perspective, it does not readily provide insights about the intertwined nature of the two, as the adaptive NMS facilitates both responses simultaneously. Other research has identified the NMS using a model that incorporates this intertwined nature, however the cognitive command signal (u_{sup} in Figure 4) had to be assumed to be zero in order for this identification to work [26]. If a pilot's supraspinal signal u_{sup} were to be measured in a future experiment, then the NMS model from De Vlugt [15] could successfully be identified during a control task like the one described in this paper.

Furthermore, while it is expected that the interrelated clamping force and neuromuscular admittance play an important role in shaping the dynamic behavior of the NMS, it would also be interesting to see how the relative contribution of proprioceptive feedback (i.e., reflexes) to the NMS's dynamic behavior would change as pilots adapt their control style. This would require measurements of not only u_{sup} , but also of the neural signal that actuates the relevant muscles in the arm.

IX. Conclusion

This paper continued research into the concept of the active manipulator which, due to the coupling between the manipulator's angular deflection and the measured roll rate of the aircraft, permanently provides the pilot with a haptic representation of the aircraft's motion. Since

previous research has already shown that a control system involving an active manipulator can provide significant benefits over a conventional control configuration, the primary objective of this paper was to determine whether the tuning procedure of such a configuration could be generalized to a set of guidelines. Based on a literature study, it was concluded that haptic cues in the form of pure *rate* feed-back are desirable, effectively reducing the gains to be tuned to a single feed-forward and a single feed-back gain. An experiment was conducted to investigate the impact of these variables on the pilot's control behavior, as well as the impact that different aircraft dynamics may have had on the gain settings that produced the most potent results. Based on the output from the experiment, a tuning procedure is proposed that aims to assist designers of future control systems involving an active manipulator with finding the optimal feed-forward and feed-back gain for their system.

References

- [1] Lanfranco, A. R., Castellanos, A. E., Desai, J. P., and Meyers, W. C., "Robotic Surgery: A Current Perspective," *Annals of Surgery*, Vol. 239, 1 2004, pp. 14–21.
- [2] Rassi, I. E. and Rassi, J. M. E., "A Review of Haptic Feedback in Teleoperated Robotic Surgery," *Journal of Medical Engineering and Technology*, Vol. 44, 7 2020, pp. 247–254.
- [3] Schmidt, G. R., Landis, G. A., and Oleson, S. R., "HERRO Missions to Mars and Venus using Telerobotic Surface Exploration from Orbit," *NASA Glenn Research Center*, 2012.
- [4] Yoerger, D. R. and Slotine, J.-J. E., "Supervisory Control Architecture for Underwater Teleoperation," *Proceedings. 1987 IEEE International Conference on Robotics and Automation*, 1987.
- [5] Steele, M. and Gillespie, R. B., "Shared Control between Human and Machine: Using a Haptic Steering Wheel to Aid in Land Vehicle Guidance," *Proceedings of the Human Factors and Ergonomics Society Annual Meeting*, Vol. 45, 10 2001, pp. 1671–1675.
- [6] Griffiths, P. G. and Gillespie, R. B., "Sharing Control between Humans and Automation using Haptic Interface: Primary and Secondary Task Performance Benefits," *Human Factors*, Vol. 47, 2005, pp. 574–590.
- [7] Abbink, D. A., Mulder, M., and Boer, E. R., "Haptic Shared Control: Smoothly Shifting Control Authority?" *Cognition, Technology and Work*, Vol. 14, 3 2012, pp. 19–28.
- [8] Beefink, D. G., Borst, C., van Baelen, D., van Paassen, M. M., and Mulder, M., "Haptic Support for Aircraft Approaches with a Perspective Flight-Path Display," *Institute of Electrical and Electronics Engineers Inc.*, 7 2018, pp. 3016–3021.
- [9] van Baelen, D., Ellerbroek, J., van Paassen, M. M., and Mulder, M., "Design of a Haptic Feedback System for Flight Envelope Protection," *Journal of Guidance, Control, and Dynamics*, Vol. 43, 2020, pp. 700–714.
- [10] Smisek, J., Sunil, E., van Paassen, M. M., Abbink, D. A., and Mulder, M., "Neuromuscular-System-Based Tuning of a Haptic Shared Control Interface for UAV Teleoperation," *IEEE Transactions on Human-Machine Systems*, Vol. 47, 8 2017, pp. 449–461.
- [11] Alaimo, S. M., Pollini, L., Bresciani, J. P., and Bülthoff, H. H., "Evaluation of Direct and Indirect Haptic Aiding in an Obstacle Avoidance Task for Tele-operated Systems," Vol. 44, IFAC Secretariat, 2011, pp. 6472–6477.
- [12] Fu, W., van Paassen, M. M., and Mulder, M., "Developing Active Manipulators in Aircraft Flight Control," *Journal of Guidance, Control, and Dynamics*, Vol. 42, No. 8, 8 2019, pp. 1755–1767.
- [13] Hosman, R. J. A. W. and van der Vaart, J. C., "Active and Passive Side Stick Controllers: Tracking Task Performance and Pilot Control Behavior," *AGARD Conference Proceedings No. 425: The Man-Machine Interface in Tactical Aircraft Design and Combat Automation*, 1987.
- [14] McRuer, D. T., Graham, D., Krendel, E., and Reisener(Jr.), W., "Human Pilot Dynamics in Compensatory Systems. Theory, Models, and Experiments with Controlled Element and Forcing Function Variations. Technical Report AFFDL-TR-65-15," Tech. rep., Air Force Flight Dynamics Laboratory, 1965.
- [15] de Vlugt, E., Schouten, A. C., and van der Helm, F. C. T., "Quantification of Intrinsic and Reflexive Properties during Multijoint Arm Posture," *Journal of Neuroscience Methods*, Vol. 155, No. 2, 9 2006, pp. 328–349.
- [16] Mulder, J. A., van der Vaart, J. C., van Staveren, W. H. J. J., Chu, Q. P., and Mulder, M., "Aircraft Responses to Atmospheric Turbulence Lecture Notes AE4304," TU Delft, 2016.
- [17] Russell, R. S., "Non-linear F-16 Simulation using Simulink and Matlab," University of Minnesota, 2003.
- [18] McRuer, D. T. and Jex, H. R., "A Review of Quasi-Linear Pilot Models," *IEEE Transactions on Human Factors in Electronics*, Vol. 8, 1967, pp. 231–249.
- [19] Jain, A., Bansal, R., Kumar, A., and Singh, K., "A Comparative Study of Visual and Auditory Reaction Times on the Basis of Gender and Physical Activity Levels of Medical First Year Students," *International Journal of Applied and Basic Medical Research*, Vol. 5, 2015, pp. 124.
- [20] Levison, W. H. and Kleinman, D. L., "A Model for Human Controller Remnant," *IEEE Transactions on Man-Machine Systems*, Vol. 10, 1969.
- [21] van der El, K., Pool, D. M., and Mulder, M., "Analysis of Human Remnant in Pursuit and Preview Tracking Tasks," *IFAC-PapersOnLine*, Vol. 52, 2019, pp. 145–150.
- [22] Schouten, A. C., "Proprioceptive Reflexes and Neurological Disorders," PhD thesis. Delft University of Technology, 2004.
- [23] Lasschuit, J., "Modeling the Neuromuscular System Dynamics for Haptic Interface Design; Identification of the NMS in multiple directions," 2007.
- [24] van Paassen, M. M., van der Vaart, J. C., and Mulder, J. A., "Model of the Neuromuscular Dynamics of the Human Pilot's Arm," *Journal of Aircraft*, Vol. 41, No. 6, 11 2004, pp. 1482–1490.
- [25] Lam, T. M., "Haptic Interface for UAV Teleoperation," PhD thesis. Delft University of Technology, 2009.
- [26] Bhoelai, A. K., van Paassen, M. M., Abbink, D. A., and Mulder, M., "Design of Test Signals for Identification of Neuromuscular Admittance," *IFAC-PapersOnLine*, Vol. 49, 2016, pp. 266–271.
- [27] Pronker, A. J., Abbink, D. A., van Paassen, M. M., and Mulder, M., "Estimating an LPV Model of Driver Neuromuscular Admittance using Grip Force as Scheduling Variable," *IEEE Transactions on Human-Machine Systems*, Vol. 50, 10 2020, pp. 454–464.
- [28] Venrooij, J., Abbink, D. A., Mulder, M., van Paassen, M. M., Mulder, M., van Der Helm, F. C. T., and Bülthoff, H. H., "A Biodynamic Feedthrough Model Based on Neuromuscular Principles," *IEEE Transactions on Cybernetics*, Vol. 44, 2014, pp. 1141–1154.

II

Preliminary thesis (previously graded
under AE4020)

1

Introduction

With the improvements made in automation, many tasks that relied heavily on manual labor several decades ago (e.g., production / assembly tasks and warehouse logistics) are now carried out by machines. There are, however, still many tasks for which the performance or reliability of automation is (perceived to be) inadequate for what is at stake (e.g., the safety of human passengers). In many of these situations, the human controller (HC) no longer contributes through continuous manual efforts, but acts as a supervisor to the automation instead.

While this often results in stable system performance with less human labor required, it may come at the cost of situational awareness. This became one of the possible causes for the 1963 BAC One-Eleven test crash, where all seven of the test flight crew lost their lives as a result of entering an unrecoverable stall condition [2]. This triggered the development of the stick shaker [3], which warns the pilot of an impending stall condition through vibrations in the control column, effectively reproducing the stick vibrations that occur as a result of the aerodynamic buffeting in mechanically controlled aircraft.

In many control tasks, HCs make use of the visual, auditory and vestibular (motion) cues that they receive to determine the best course of action. Haptic cues, like the ones generated by the stick shaker, come through the sensation of touch in the skin as well as the sensation of force and motion in muscles and joints. By supplying haptic feedback to the HC, an additional display is essentially created between the HC and the environment, which improves the involvement of the HC with the task at hand.

While haptic cues can be helpful to the HC's performance as a supervisor (as is the case for the occasional warnings from the stick shaker), continuous haptic feedback *also* has the potential to improve the HC's performance during manual control tasks. As such, haptic cues can not only improve performance in situations that are impractical to automate (e.g, exploratory tasks), but also form a flexible alternative in situations where the automation fails to deliver (e.g, evasive maneuvers or aircraft landings without functioning navigational systems). Concrete examples of systems that already incorporate haptic cues in manual control tasks range from remotely-controlled exploration vehicles [4] [5] to robotic surgery [6] [7] and exoskeletons [8]. In some of these applications, the automation is able to communicate its intentions back to the HC, while still providing the HC with the possibility to override those intentions. This design philosophy is referred to as 'haptic shared control', and it has become a concept of interest approximately two decades ago [9] [10] [11].

Virtually all research about haptic shared control in the context of flight has been explored using a manipulator (i.e., the control column, side stick, or 'stick') like the ones that are currently installed in fly-by-wire (FBW) aircraft. Such a configuration translates the measurement of the stick's position into a deflection of the aircraft's control surfaces. This stick position comes to be through two factors: 1) the force applied to the stick by the HC and 2) the mechanical properties of the stick. Haptic shared control relies on the ability of the HC to feel the cues provided by the automation, and possibly override them. As a result, this means that haptic feedback in such a 'passive stick' configuration can only come through the aforementioned two terms, that is through **force feedback** or active adjustment of the stick's mechanical properties [12] [13].

Fu et al. [14] have recently explored haptic shared control in the context of flight, using a fundamentally different approach that was introduced by Hosman et al. [15] and is referred to as the 'active stick' throughout this thesis. In this configuration, there is a direct and permanent link between the position of the manipulator and the motion of the aircraft itself. The resulting user experience is comparable to that of vehicles that HCs are most familiar with (e.g., cars and bicycles), where the steering device shoots sideways when being confronted with crosswinds. To realize this experience in an aircraft, the stick position is no longer what drives the control surfaces, and it is no longer directly the result of the applied force and the stick's mechanical properties. Instead, the force applied on the stick by the operator is now what drives the aircraft's control surfaces, which in turn rotate the aircraft. This motion is then measured and fed back to servo motors that impose the position of the stick on the HC. To summarize the working principle of the active stick: force is what drives the aircraft and the haptic cues come to the HC in the form of **position feedback**.

Fu has demonstrated that the active stick with its position feedback can provide significant benefits to the HC in terms of tracking performance and exerted control effort. Whereas the target signal tracking performance for the active and passive stick was comparable, the active stick proved to be especially helpful for rejecting disturbances acting on the aircraft, such as turbulence, more effectively. During Fu's experiment, the HC was seated in fixed-base simulation environment, which means that this scenario is most comparable to that of an aircraft or drone whose motion is being controlled remotely from the ground.

This thesis aims to expand upon the idea of the active stick, by determining whether the design of such a 'full' haptic link between the aircraft and the stick can be generalized to a set of practical guidelines. Figure 1.1 provides a graphical representation of the approach envisioned to reach this objective. In general, this approach can be summarized as:

1. Study the experimental setting and findings produced by Fu [14] regarding the active stick and its performance relative to the conventional passive stick.
2. Study the neuromuscular system, which plays a key role in the effectiveness of the active stick.
3. Reproduce the experimental setting in a model, which incorporates a detailed description of the neuromuscular system.
4. Determine three reasonable HC settings (the 'relaxed', 'average' and 'tense' controller), by fitting the model on the existing experimental frequency response plots generated by Fu [14] and taking into account the simulated time-domain performance.
5. Simulate a variety of active stick settings for the relaxed, average and tense controller, using the previously tested Boeing 747 roll dynamics as well as ones from the Cessna 500 Citation and the F-16.
6. Use the simulation output to identify trends and dependencies in active stick settings that lead to a strong performance.
7. Propose an active stick tuning procedure, derive the testing conditions from said procedure and generate performance predictions using the model.
8. Test the conditions and make observations about participants' control behavior using time- and frequency-domain analyses.
9. Provide design recommendations for future control systems involving an active stick, as well as recommendations for future experiments to be conducted to further progress the active stick's development.

The structure of the report has been defined to suit this approach. First, Chapter 2 introduces the fundamental concepts inherently related to the control task at hand (i.e., items 1 and 2). This includes manual control theory, a review of haptics in aircraft control and an introduction to the concept of the active manipulator. It also includes a review of the experiment conducted by Fu [14], as this information is needed for the data fitting procedure that is conducted at the start of Chapter 4. After all relevant subjects have been introduced, Chapter 3 covers item 3, by going into detail about the information that is used to model the human response for this task accurately.

Chapter 4 forms the foundation of the innovation made by this thesis, by summarizing the findings that are facilitated with the model from Chapter 3. As mentioned above, the model is first used to determine three reasonable HC settings, by fitting the model on the frequency-domain data that has been generated for the various conditions tested by Fu [16] (item 4). Afterwards, a wide variety of conditions is simulated, which involves a factorial combination of the three HC settings, three different aircraft roll dynamics and 168 active stick settings (item 5). The simulation output of these conditions is used to identify trends in performance, which are combined with the existing theory on manual control presented by McRuer [1] to propose a tuning procedure for the active stick (item 6). Based on the proposed tuning procedure, the testing conditions for this thesis are determined and performance predictions are generated using the model (item 7). Chapter 5 builds on top of this information, by providing an overview of the variables that will be measured during and derived from the experiment (item 8). Finally, the report is concluded in Chapter 6.

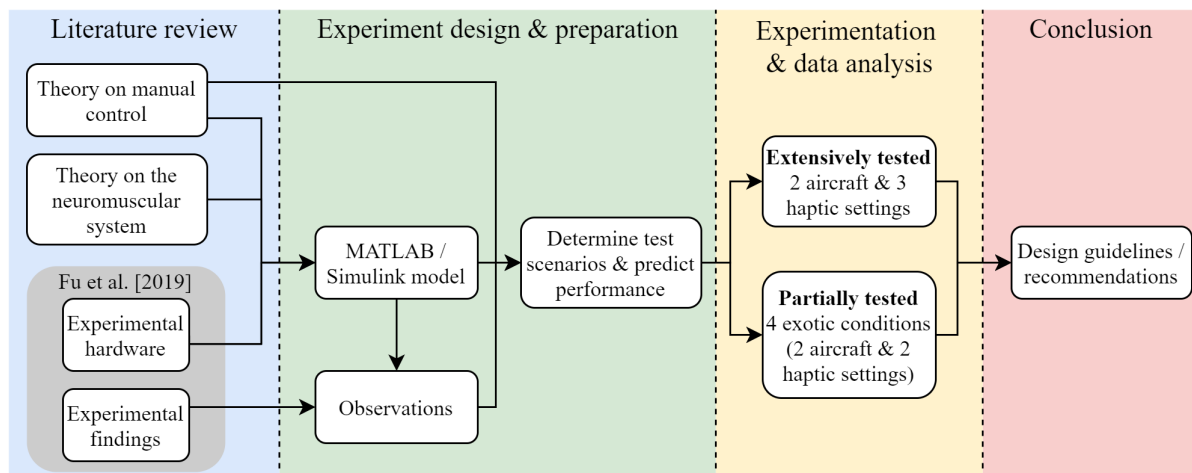


Figure 1.1: A basic framework of the approach envisioned for this thesis.

2

Understanding the problem

The starting point for any research project is to identify the context that clarifies the topic and the work that has been done, and that facilitates a focused plan for the scientific progress to be made in this thesis and hereafter. To start off, Section 2.1 provides a brief review of the fundamental information related to manual control theory. This is followed by Section 2.2, which summarizes the current lines of development regarding haptics in aircraft control and classifies them in two different ways. Section 2.3 then introduces the object of interest for this study (i.e, the active stick) and emphasizes what makes this concept unique over the conventional passive stick.

Section 2.4 introduces the neuromuscular system, which plays an instrumental role in receiving haptic cues and executing physical commands. The information from these sections is all that is needed to explain the control task at hand, which is done in Section 2.5. As is mentioned in Chapter 1, this section also summarizes the experimental findings of Fu [14], as this information is needed to understand the model fitting procedure from Chapter 4 as well as the reasoning towards the testing strategy laid out in this thesis. Finally, Section 2.6 states the objective of this thesis and illustrates how the envisioned outcome may open the door to various lines of research.

2.1. A review of manual control

Whenever a human plays a role in a control task, his/her contribution can be of mainly two different natures:

1. **Supervisory control.** This type of behavior revolves around monitoring control tasks that are automated, with the intention of intervening only when the automation does not produce the expected system behavior. A common example of this type of control is found in the cockpit, where pilots spend the majority of their long-haul flights monitoring the actions carried out by the autopilot and flight management systems.
2. **Manual control.** Whenever a control task is continuously dependent on the input provided by a human controller (HC), this is considered a manual control task. Examples that quickly come to mind involve personal transportation, e.g., keeping one's car or bicycle in the right lane. In aeronautics, take-off and landing procedures are often done by hand.

Depending on the control task at hand, the HC's contribution may either be of one type, or some combination of the two. This thesis focuses solely on the second type: manual control. Generally speaking, manual control tasks involve HCs following a moving target (also known as a target forcing function) using the system that they are controlling, while being exposed to disturbances from the environment. Depending on the way that information about the task is presented to the HC, a manual control task can be classified in three different ways:

1. **Preview tracking task.** A manual control task can be considered a 'preview tracking task', whenever the HC is able to perceive how the target of said task will move in the (near) future. This type of control task is the most common in the physical world, as HCs are typically able to anticipate the way their target moves (ranging from winding roads to flying tennis balls). The way information about the future is processed internally and included in the current control behavior makes this the most complex type of control task to analyze and make predictions about.

2. **Pursuit tracking task.** During this type of control task, HCs attempt to follow a moving target without knowing anything about its future movements. The HC does so by continuously comparing the target and the system's current state, and providing a corrective action to the system as a result of that comparison.
3. **Compensatory tracking task.** This is the type of control task that is tested in this thesis. McRuer et al. have laid the groundwork for manual control with their research on compensatory tracking tasks in the 1960s [1]. This control task is essentially a pursuit tracking task, but the comparison between the target and the system's current state is no longer to be interpreted by the HC. Instead, the system error e is the only parameter which the HC can directly perceive and act upon (see Figure 2.1). While this type of control task is the least resemblant of common control tasks that HCs perform every day, its simplicity allows for the identification of the most basic component of the human response in a given control system. Using the knowledge about this basic response, the effects of internal processing of current and future information can be determined in the more complex pursuit and preview tracking tasks.

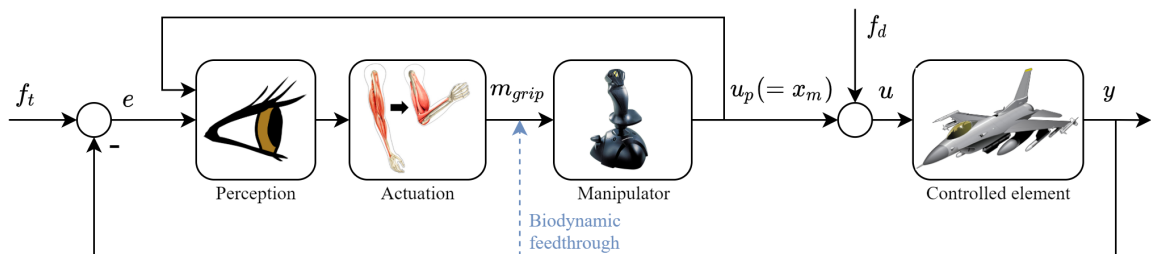


Figure 2.1: A basic representation of the conventional compensatory tracking task, in the context of flight.

Based on the information presented to the HC, he or she decides what action to take. This decision is translated from an electrical signal from the brain to the contraction of certain muscles. The collection of body parts responsible for facilitating this process is called the **neuromuscular system**, whose significance will be elaborated upon in Section 2.4.

Figure 2.1 shows how the neuromuscular system produces a force (here defined as m_{grip}) on the manipulator. In the conventional manipulator design (referred to as the 'passive stick' in this thesis) that is used in virtually all academic research and FBW aircraft, this force, combined with the mechanical properties of the stick, result in a certain stick position x_m . The measured value of x_m is then fed to the aircraft to realize certain control surface deflections, which in turn affect the motion of the aircraft that is represented through its output y .

This basic example calls for a couple of nuances, which are already presented in Figure 2.1. Firstly, it is normal for control tasks to be subjected to some disturbing force, which in our situation comes in the form of turbulence. The disturbance is represented by the forcing function f_d and is typically introduced at the input of the controlled element (or 'plant'). This means that the signal which actually drives the system is the sum of the HC's explicit input and some disturbance signal that the HC cannot observe nor control directly, in other words $u = u_p + f_d$.

Secondly, the HC does not only make use of the perceived error e when deciding what to do. In practice, this error e is used internally to determine which stick position x_m would be ideal right now, and a comparison between said position and the current x_m results in the intended muscle force m_{grip} . Thirdly, the system may provide feedback to the HC in an additional way for the situation of on-board control. Besides the various types of cues that are mentioned in Chapter 1, the motion of the aircraft may also have a direct, involuntary impact on the force that the HC applies on the manipulator. This effect is called biodynamic feedthrough [12] and can lead to pilot-induced oscillations (PIOs) in extreme situations.

2.2. A review of haptics in aircraft control

Most modern FBW aircraft have incorporated haptic feedback in their manipulators in what can be considered a rather 'supervisory' fashion. As was already mentioned in Chapter 1, the oldest example of this the stick shaker [3], which only activates whenever an aircraft is approaching a stall condition. A similar but physically more disruptive implementation that was developed around the same time was the stick pusher; an electromechanical device that pushed the stick forwards whenever an aircraft approached stall [17]. After the first applications of haptics were implemented, a lack of computational power and efficient actuator designs caused the development of haptics to stagnate. Technological advancements reinvigorated the interest for haptics in the 1990s and caused a steadily increasing amount of publications ever since.

Research papers published about haptics in aircraft control may be classified in two ways:

1. **Remote control versus on-board control**
2. Haptic cue philosophy: **interpreted** (objective-oriented) **versus observed** (vehicle-oriented)

Until now, the remotely-controlled aircraft received the majority of attention for research regarding haptics [18] [19]. The case of on-board control of aircraft and helicopters, on the other hand, has received less attention, although numerous examples exist [20] [21]. As mentioned in Section 2.1, an effect that does come into play during on-board control is biodynamic feedthrough [22]. To prevent haptic cues from facilitating any PIOs, the interaction between said cues and biodynamic feedthrough ought to be understood before they can be recommended for practical use.

Regardless of the distinction made at point 1, the vast majority of research papers published on this topic involve haptic cues, which are generated as a result of the automation's interpretation of what ought to be done next by the HC. The most popular example for this is collision avoidance, where the automation directly [18] [23] or indirectly [24] [25] pushes the HC away from simulated obstacles using force feedback from the manipulator. Another example which contains a comparable level of interpretation by the automation involves haptic cues, which are generated using the highway-in-the-sky concept [26] [27]. Here, the automation generates haptic cues that push the aircraft towards the right trajectory, which reduces the HC's tendency to stare down at the flight display, where this three-dimensional, transparent tunnel is presented. A different approach is taken more recently by D'Intino et al. in the context of a helicopter [20]. In this approach, the automation combines the HC's input with a probabilistic model to estimate the HC's intended trajectory, and provides a corrective force to the manipulator that ought to steer the helicopter towards that path.

Whereas the aforementioned (objective-oriented) approaches may prove useful in various situations, the reliance on accurately defined boundary conditions may render some of them of limited use outside nominal or standard operations. A vehicle-oriented approach operates differently, in the sense that the automation sends no corrective forces based on a mission that it either estimates in real-time or has defined beforehand. Instead, a vehicle-oriented approach bases its haptic cues on measurements of the aircraft state. The most 'interpreted' variant that can be discussed here revolves around flight envelope protection. This approach, as introduced by Ellerbroek et al., involves the automation actively shifting the stick's neutral point and its mechanical stiffness based on the aircraft's current position inside the flight envelope [12]. More recently, Van Baelen et al. have studied more extensively how such haptic feedback is best designed, by analyzing it for the hazardous flight conditions that occur during a windshear or icing event [13].

A slightly older, vehicle-oriented method presented by Alaimo et al. aimed to increase the HC's situational awareness, by simulating a 'mechanically steered' feel on the stick for a remotely controlled aircraft [28]. This was achieved using force feedback and an adaptive manipulator stiffness. An interesting comment is made by Alaimo about this in a later paper [24]: *"Although the haptic force was not designed in order to help the pilot to reject the wind gust, and, to certain extent, even disturbed him, it successfully increased the pilot situational awareness in terms of external disturbances since mean performance was improved with respect to the case of no haptic aiding"* (p.6474).

2.3. The active stick

More recently, Fu et al. [14] took a fundamentally different vehicle-oriented approach to haptic feedback, which included experimental findings that are interesting to compare with the quote from the previous section. As opposed to the passive manipulator design introduced in Section 2.1, Fu extended the 'active' manipulator approach, based on the work of Hosman and Van der Vaart [15] and Hosman et al. [29].

Figures 2.2a and 2.2b illustrate the difference between these approaches graphically. For the active stick, the force applied to the manipulator by the HC is what commands the control surfaces, and the stick's position is imposed on the HC using servo motors, based on measurements of the aircraft state. In doing so, a full haptic link is established between the motion of the aircraft and the motion of its manipulator. In line with Alaimo's comment of earlier, Fu showed that such a full haptic link can be beneficial to the HC, especially for rejecting disturbances more easily and effectively.

On top of that, participants of Fu's experiment experienced a similar discomfort while using the active stick. This discomfort became more pronounced when the bandwidth of the forcing functions was increased. As the disturbance acting on the aircraft became more aggressive, the aircraft's motion (and thus the manipulator's motion) became more aggressive as well. Once the manipulator moved around faster than the HC could consciously move around his/her arm (in other words, the manipulator's motion bandwidth stretched beyond the HC's crossover region), the haptic cues caused involuntary arm movements that were deemed unhelpful and merely added workload. To address this issue, Fu applied a low-pass filter to the haptic cues, which improved the user comfort while sacrificing little to none of the tracking performance.

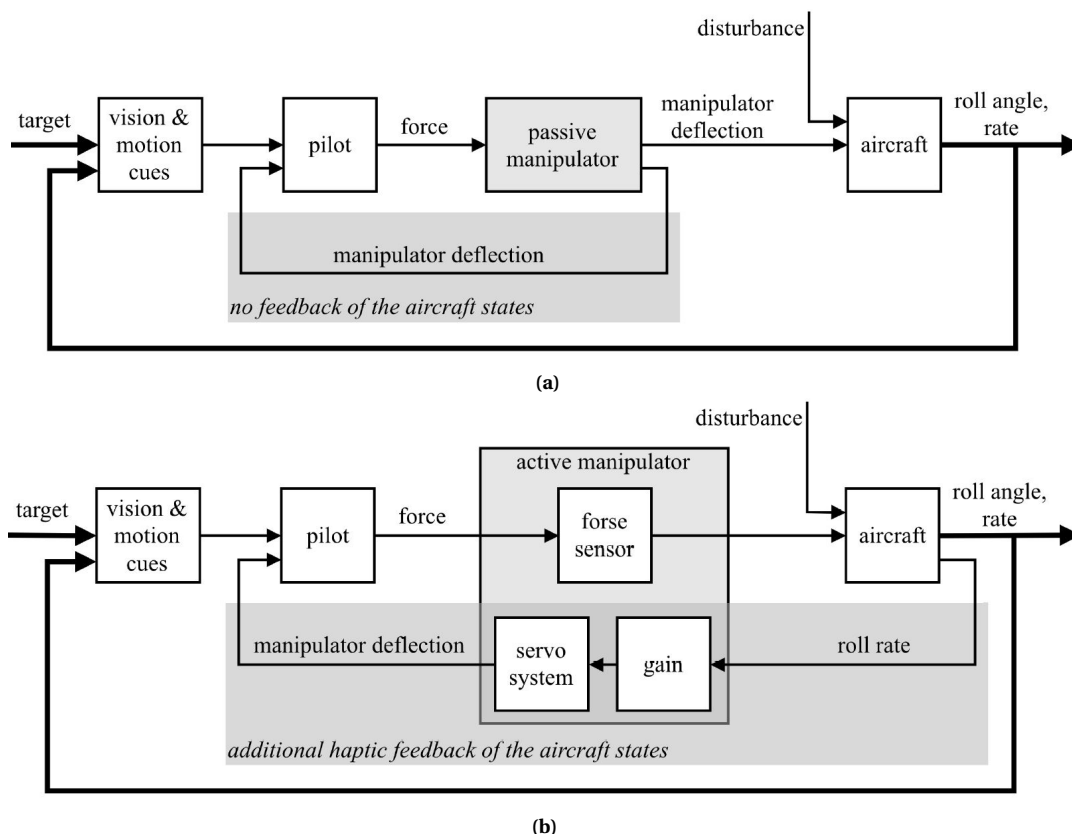


Figure 2.2: The passive and active stick models as presented by Fu [14]. (a) Schematic diagram of the passive stick model, where the stick deflection is directly the result of force applied to the manipulator. (b) Schematic diagram of the active stick model, where the stick deflection is imposed on the human controller using measured system behavior.

2.4. The neuromuscular system and its adaptive nature

The human response can be summarized as the collection of internal processes responsible for receiving information, processing information and executing control commands. What lies at the core of these processes is the neuromuscular system (NMS). It facilitates the two types of control behavior that together amount to the total force exerted on the stick (m_{grip}): cognitive and reflexive.

Cognitive behavior is produced as result of the various cues that are processed in the brain into conscious commands, which are then executed by the NMS. Reflexive behavior, on the other hand, occurs as a result of haptic sensor feedback without conscious involvement of the brain. In this situation, the haptic sensory output is sent to the relevant muscles directly through the spinal cord, which can serve as a defense mechanism against imminent harm (e.g., overstretching a muscle or burning a finger). Figure 2.3 provides a schematic overview of the NMS architecture in the context of the well-known knee jerk reflex.

Until now, it may seem like HCs have no control over the reflexive behavior that the NMS produces, however this is not the case. The sensors and muscles that may produce reflexive behavior are also inherently part of the cognitive control loop, which means that HCs are able to 'tune' these components in various ways based on the instructions that they are following. For the case of the active stick, this means that a perturbation in the stick's position x_m can lead to a range of reaction forces m_{grip} from the arm. The ratio of imposed displacement to resulting reaction force ($\frac{x_m}{m_{grip}}$), also known as the *admittance*, is a useful relationship to quantify the HC's sensitivity to haptic perturbations. As the name suggests, a high admittance allows for much displacement with relatively little force to resist that motion, while a low admittance provides much resistance force to allow little displacement. Whereas the admittance may vary considerably depending on the task at hand, three basic control objectives have been defined that aim to determine its most extreme values [30]:

1. **The position task (PT).** During this task, the HC is instructed to keep the manipulator in a given position, actively rejecting any haptic disturbances that may occur.
2. **The relax task (RT).** As the name suggests, the HC is instructed to relax the arm and let haptic disturbances freely change the motion of the manipulator and the arm.
3. **The force task (FT).** During this task, the HC is instructed to keep m_{grip} constant. In practice, this means that the HC is actively giving way to any haptic disturbance that may be produced by the manipulator.

2.5. The experimental setting and previous findings

This section summarizes the experimental setting that was used by Fu [14] and will be used for this thesis, as well as the test scenarios and findings produced by Fu earlier. Participants are seated in the human-machine interface (HMI-) lab, a fixed-base simulator environment at the Technical University Delft (TU Delft). Figure 2.4 shows the hardware that is used for carrying out the task: an 18-inch liquid crystal display (LCD) screen and a two-axis hydraulically-driven manipulator.

The participants are tasked with a one-dimensional control task, where they only have to control the aircraft's roll angle ϕ . For this reason, the servo motor responsible for the manipulator's pitch motion is constrained in the neutral position. Every test run lasts 90 seconds, of which the last 81.92 seconds are used for data analysis.

2.5.1. Forcing function design and controlled element dynamics

A target (f_t) and disturbance (f_d) forcing function are both defined as the sum of ten sinusoids (see Equations 2.1 and 2.2). Fu [14] intended to make these forcing functions of equal difficulty in two ways. On the one hand, Fu paired the signals' sinusoid frequency components ($\omega_t(k)$ and $\omega_d(k)$) as much as possible, as can be seen in Tables 2.2 and 2.3. This is reflected more clearly in the number of periods that these sinusoids fit inside the measurement time of 81.92 seconds. On the other hand,

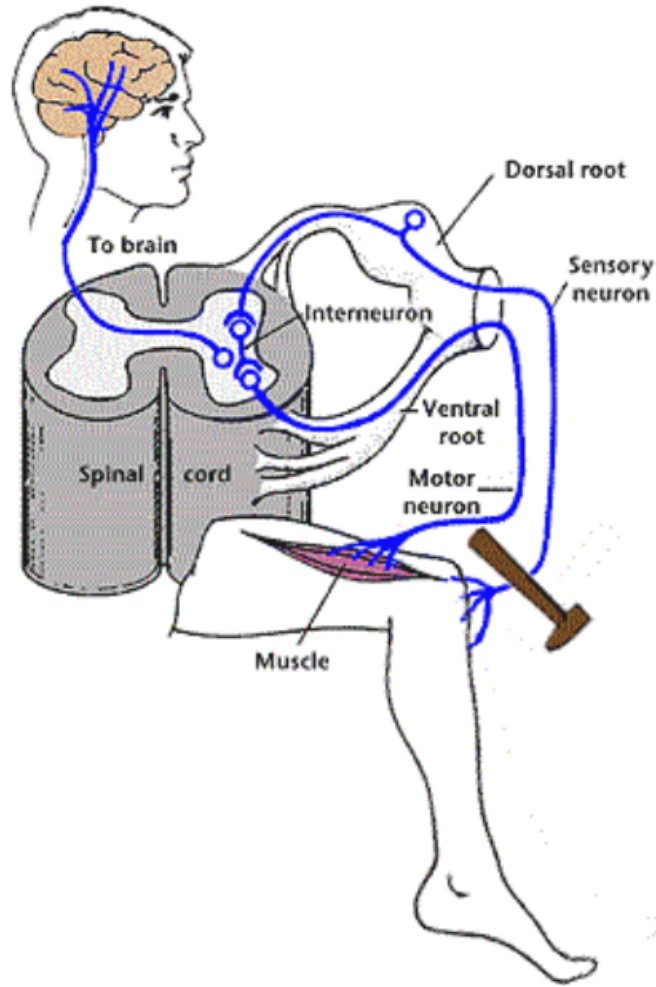


Figure 2.3: A schematic representation of the neuromuscular system. Image extracted from: <http://www.corpshumain.ca/Touche.php>

the amplitude of the sinusoids ($A_t(k)$ and $A_d(k)$) are all determined using the shaping filter shown in Equation 2.3 (where $K_{ff} = 0.2$ and $\zeta_{ff} = 0.7$). In doing so, both forcing functions were essentially defined in terms of roll angles ϕ_t and ϕ_d .

For the experiment at hand, a direct expression for both the roll angle ϕ and the roll rate $\dot{\phi}$ are desired. The latter term can be obtained directly from the CE dynamics H_c if the disturbance signal is not injected *after* said dynamics, but before them (in line with Figures 2.1, 2.2a and 2.2b). To do so, f_d needs to be scaled by $\frac{1}{|H_c|}$, as is shown in Figure 2.5. Finally, the sinusoid phase angles $\theta_t(k)$ and $\theta_d(k)$ from Equations 2.1 and 2.2 are randomized for every test run to prevent participants from recognizing any patterns in the signals.

$$f_t(t) = \sum_{k=1}^{10} A_t(k) \sin(\omega_t(k)t + \theta_t(k)) \quad (2.1)$$

$$f_d(t) = \sum_{k=1}^{10} A_d(k) \sin(\omega_d(k)t + \theta_d(k)) \quad (2.2)$$

$$H_{ff}(s) = K_{ff} \cdot \frac{(1/\omega_{ff,L}^2)s^2 + (2 \cdot \zeta_{ff}/\omega_{ff,L})s + 1}{(1/\omega_{ff,l}^2)s^2 + (2 \cdot \zeta_{ff}/\omega_{ff,l})s + 1} \quad (2.3)$$



Figure 2.4: The LCD screen and manipulator used in the experiment [14].

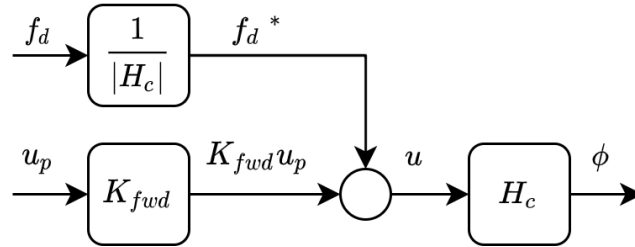


Figure 2.5: Prefiltering of the disturbance forcing function f_d [14].

Three variants of f_t and f_d were created and tested by Fu [14], by varying the shaping filter's corner frequencies as shown in Table 2.1. This resulted in the forcing function properties shown in Tables 2.2 and 2.3. The highlighted signals defined by the intermediate filter bandwidth are the ones that will be used in all test scenarios of the upcoming experiment that is explained in greater detail in Chapter 5. The CE dynamics used by Fu [14] were Boeing 747 roll dynamics, whose open-loop gain and roll subsidence mode have been adjusted to make the aircraft easier to control. Equation 2.4 shows this result, where the leftmost component of the transfer function represents the fast actuator dynamics and $K_{c,B747} = -3.5$.

$$\begin{aligned}
 H_{c,B747}(s) &= \frac{1}{0.083s+1} \cdot K_{c,B747} \cdot \frac{2.259s^2 + 0.821s + 1}{s(0.4s+1)(1.647s^2 + 0.336s + 1)} \\
 &= \frac{1}{0.083s+1} \cdot \frac{-12s^2 - 4.362s - 5.313}{s^4 + 2.704s^3 + 1.117s^2 + 1.518s} \\
 &= \frac{-7.906s^2 - 2.873s - 3.5}{0.05468s^2 + 0.8067s^4 + 1.842s^3 + 0.819s^2 + s}
 \end{aligned} \tag{2.4}$$

Table 2.1: The forming filter properties that define the three forcing function variants used by Fu [14].

Bandwidth	$\omega_{ff,l}$ [rad/s]	$\omega_{ff,L}$ [rad/s]
BW1	0.60	4.80
BW2	1.00	8.00
BW3	1.65	13.2

Table 2.2: The properties of the three target forcing functions tested by Fu [14]. The signal in bold is the one that will be used in the upcoming experiment.

k	Period	ω_t [rad/s]	A_t [rad]		
			BW1	BW2	BW3
1	5	0.3835	0.1864	0.1984	0.1999
2	11	0.8437	0.0910	0.1645	0.1944
3	21	1.6107	0.0277	0.0724	0.1462
4	37	2.8379	0.0094	0.0248	0.0645
5	51	3.9117	0.0056	0.0134	0.0352
6	71	5.4456	0.0039	0.0074	0.0185
7	101	7.7406	0.0033	0.0045	0.0095
8	137	10.5078	0.0032	0.0036	0.0058
9	191	14.6495	0.0031	0.0032	0.0040
10	224	17.1806	0.0031	0.0032	0.0036

Table 2.3: The properties of the three disturbance forcing functions tested by Fu [14]. The signal in bold is the one that will be used in the upcoming experiment.

k	Period	ω_d [rad/s]	A_d [rad]		
			BW1	BW2	BW3
1	6	0.4602	0.0242	0.0273	0.0278
2	13	0.9971	0.0102	0.0213	0.0281
3	23	1.7641	0.0097	0.0258	0.0557
4	38	2.9146	0.0084	0.0220	0.0574
5	53	4.0650	0.0090	0.0209	0.0551
6	73	5.5990	0.0120	0.0221	0.0550
7	103	7.9000	0.0215	0.0289	0.0599
8	139	10.6612	0.0413	0.0462	0.0736
9	194	14.8796	0.0934	0.0964	0.1173
10	227	17.4107	0.1407	0.1430	0.1606

2.5.2. Sign conventions

Figures 2.6a and 2.6b introduce the sign conventions related to the experimental setting. On the left, a closeup of the manipulator is presented. In line with the standard convention for aircraft control, the counterclockwise motion of the manipulator is defined as the positive direction. Such a positive deflection then results in a negative aircraft roll rate (i.e., a rolling motion towards the left), which explains the ‘-’ sign of the open-loop gain $K_{c,B747}$ that is introduced in Section 2.5.1.

The right image presents the artificial horizon that participants will see on the LCD screen. The tracking error $e (= f_t - \phi)$ represents the amount of roll that needs to be carried out to reach the desired position, in other words when $e = +20^\circ$, the aircraft needs to roll 20° to the right. Linking that back to the previous point, this means that a positive tracking error e will induce a negative moment force / stick deflection. It is worth mentioning that this convention conflicts with the one used by Fu [14], which translates a positive stick input to a positive roll rate. As a result, the values used by Fu for K_c and the haptic feedback gain are multiplied by -1 .

For the sake of convenience, the forces produced by the arm (m_{res}) and exerted on the stick (m_{grip}) are expressed in moments around the rotation axis of the stick, which lies approximately 90 mm below the central gripping point of the HC’s hand. The small difference between the displacement of the stick (x_m) and the local displacement of the arm (x_{arm}) is bridged by a spring-damper system that represents the skin dynamics. Sections 3.1 to 3.3 will go into more detail about how the skin dynamics and others that impact the arm’s motion are defined.

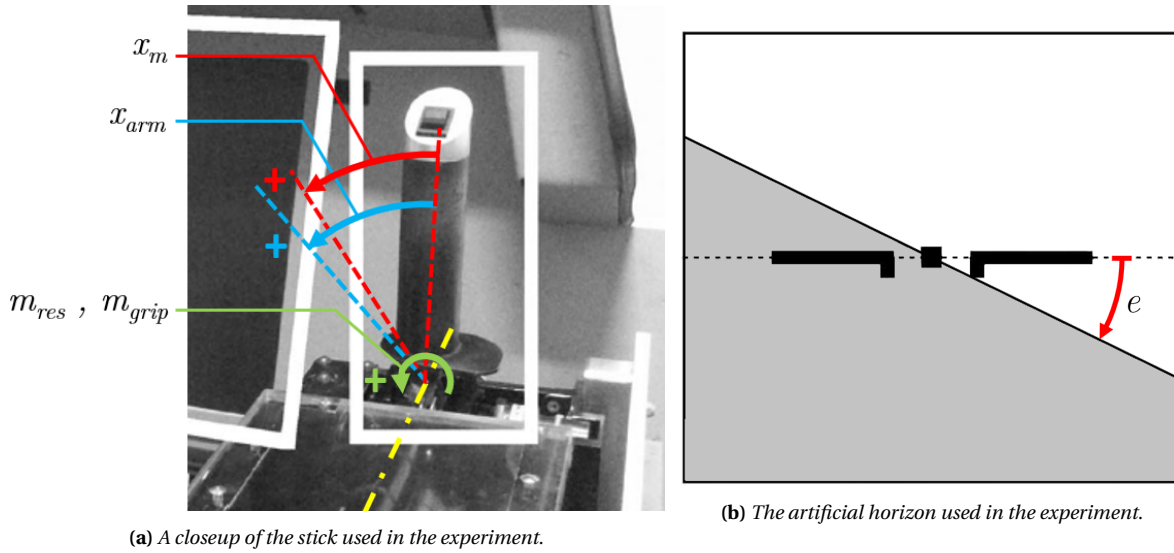


Figure 2.6: The sign conventions used in this thesis (modified images from [14]).

2.5.3. Previous experimental findings

As mentioned in Section 2.5.1, Fu [14] exposed twelve participants to three forcing function variants, whose spectral properties are summarized in Tables 2.2 and 2.3. These forcing functions were tested for the passive stick and for one setting of the active stick. All test runs were conducted using the B747 roll dynamics shown in Equation 2.4, which resulted in a total of six testing conditions.

Fu found out that the full haptic link provides significant benefits to the HC, both in terms of tracking performance and required control effort. These benefits, which become more pronounced for increasingly difficult (i.e., larger bandwidth) forcing functions, can primarily be accredited to a more effective rejection of disturbances. This can be explained by the fact that a direct link between the dynamics of the manipulator and the aircraft removes the need for processing visual, aural and vestibular cues to identify and react to the disturbances that act upon the system. Instead, the disturbance rejection task is now effectively delegated to the neuromuscular system, which has an instant response to the disturbance through the intrinsic mechanical properties of the arm, and a reflexive response (demonstrated in Figure 2.3) that is much quicker than its cognitive counterpart.

As mentioned in Section 2.3, Fu also found out that the haptic cues from the active stick were only helpful up to the HC's crossover region ($\omega_c \approx 5$ rad/s). Haptic cues of higher frequencies caused involuntary arm movements that were considered intrusive, adding to the physical workload. This is why the low-pass filter shown in Equation 2.5 (with $\omega_{lpf,l} = 5$ rad/s, $\omega_{lpf,L} = 8$ rad/s and $\zeta_{lpf} = 0.7$) was applied. As expected by Fu [14], this increased user comfort with no significant change in target tracking performance.

$$H_{lpf}(s) = \frac{\omega_{lpf,l}^2}{\omega_{lpf,L}^2} \cdot \frac{s^2 + 2\zeta_{lpf} \cdot \omega_{lpf,L} + \omega_{lpf,L}^2}{s^2 + 2\zeta_{lpf} \cdot \omega_{lpf,l} + \omega_{lpf,l}^2} \quad (2.5)$$

Besides the fact that reflexive behavior and intrinsic mechanical properties can respond more quickly to disturbances than cognitive behavior, the direct link between the dynamics of the manipulator and the aircraft has a defining impact on the system dynamics that the HC effectively experiences. This is illustrated in Figure 2.7. Whereas this thesis takes into account the intertwined nature of H_e (the response to the visually perceived error) and H_x (the predominantly NMS response to the haptically presented aircraft roll motion), the figure demonstrates clearly how a manipulator whose position is linked to the aircraft's roll **rate** results in an HC effectively experiencing **single** integrator dynamics when moving the stick around.

Similarly, a manipulator whose position would be linked to the aircraft's roll acceleration would

result in the HC effectively experiencing double integrator dynamics. Moreover, it is worth emphasizing that the relationship between a manipulator's position and the vehicle's response (i.e., $\frac{\Phi(s)}{X_m(s)}$ in our situation) is ultimately what defines the HC's conscious impression of the system, regardless of whether that may be the handlebars on a bicycle, the steering wheel in a car or on a ship, or the control column on a flight deck.

To summarize the point made above: the innovative concept of position feedback presented by Fu [14] allows one to transform the CE dynamics effectively experienced by the HC ($\frac{\Phi(s)}{X_m(s)}$) into $\frac{1}{H_{hfb}(s)}$, given that $\frac{X_m(s)}{U(s)} = H_{hfb}(s)H_c(s)$. This enables one to tailor the HC's control experience to the HC's preferred control task, in accordance with the verbal adjustment rules postulated by McRuer and Jex [31].

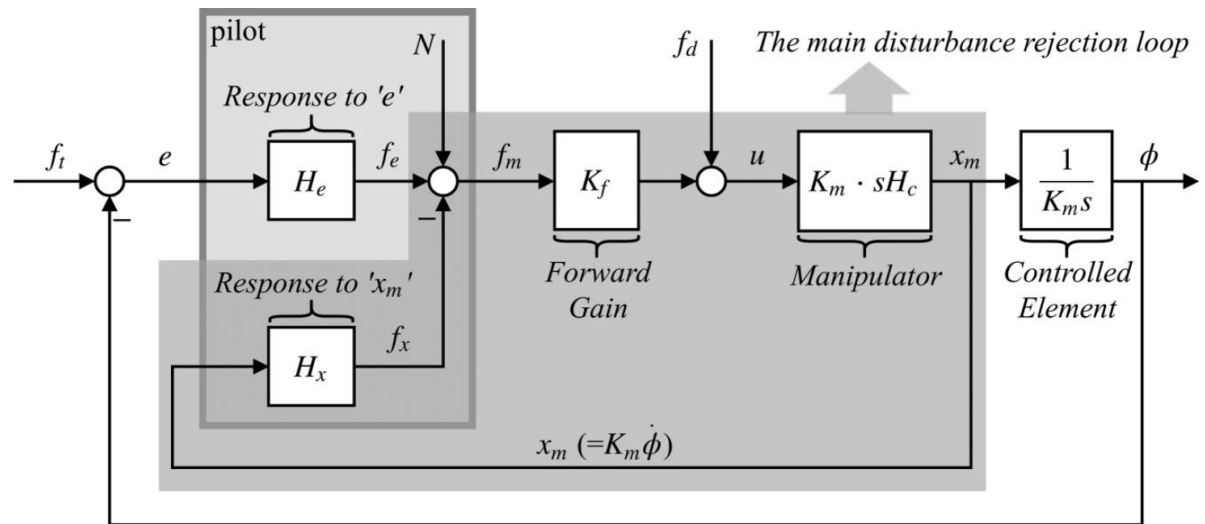


Figure 2.7: A visual explanation of how the identity of the active stick's haptic feedback (i.e., a pure rate feedback $K_m s$ in this case) dictates the CE dynamics that the human controller effectively experiences [14].

2.6. Thesis objective and academic roadmap

This thesis aims to further progress the development of a full haptic link in the context of aircraft control, by reproducing the results generated by Fu [14] and testing various new scenarios involving different aircraft dynamics and haptic feedback settings. Figure 2.8 shows how achieving this result may open the door to:

1. The generalization of a full haptic link for two-dimensional compensatory tracking tasks, thereby incorporating the HC's full range of arm movement with the corresponding neuromuscular characteristics,
2. The feasibility study of a full haptic link in an on-board setting, thereby incorporating the effects of biodynamic feedthrough, and
3. The design of a full haptic link in a dynamical system (both on-board and remotely controlled) whose properties change over time, which can be the result of changing flight conditions or system failures.

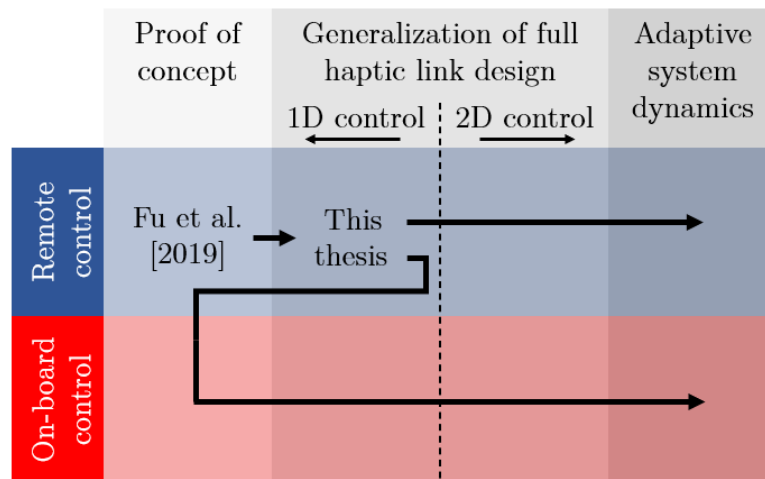


Figure 2.8: A graphical representation of the scientific contribution of this thesis, as well as two possible lines of development that may follow after.

3

Quantifying cognitive and reflexive control behavior

For many control tasks that involve a human controller, the human contribution is modelled in a rather basic fashion. This often means that the collection of internal processes responsible for receiving information, processing information and executing commands are all lumped together in a single, simple transfer function. Besides that, it is uncommon that the occurrence of reflexive behavior is discussed or modelled for a given control task. Since the concept of the full haptic link relies on reflexive behavior for reduced tracking errors and control effort, it makes sense to gain a more profound understanding of said behavior, and how it is related to its cognitive counterpart.

Section 2.4 has provided an introduction to the neuromuscular system, which plays a central role in realizing both types of control behavior. Section 3.1 continues this story by introducing the TU Delft neuromuscular model, which incorporates the various sensors, actuators and links that form the neuromuscular system at a component level. Afterwards, Section 3.2 provides an approximation of the HC's cognitive response, along with an estimation of the nonlinear behavior that HCs may exhibit. Finally, Section 3.3 unifies the information from Sections 3.1 and 3.2 into an 'active stick' model, which will be used for the performance analyses and predictions in Chapter 4.

3.1. Modelling the neuromuscular system

As was mentioned in Section 2.4, the neuromuscular system is composed of the sensors, links and actuators that allow for the coordination of body parts. Previous biophysical research that has been carried out at TU Delft resulted in the proposal of a neuromuscular model that incorporates the dynamics of these sensors, links and actuators separately, in the context of a pilot controlling the manipulator on a flight deck [32]. This model translates the current position of the hand and the supraspinal, conscious reference signal emitted by the brain's motor cortex into a moment force exerted by the hand. De Vlugt et al. combined this model with the findings regarding skin dynamics from Van Paassen [33], which resulted in a neuromuscular model that translates the manipulator's position and the supraspinal reference signal into a moment force exerted on the manipulator [34].

Figure 3.1 provides an illustration of this model. To be able to identify the neuromuscular parameters that form this model, De Vlugt introduced a known disturbance force F on the passive stick H_{st} and participants were instructed to hold the stick in a certain position (i.e., the position task, where u_{sup} was assumed to be zero).

3.1.1. Muscle spindles

Muscle spindles are proprioceptive sensory receptors (proprioceptors) located in the belly of muscles. These 'position sensors' provide information to the central nervous system (CNS) about the muscle stretch and muscle stretch rate, which is used during postural control and facilitates reflexive behavior that prevents muscle overstretching [35]. Its behavior can be approximated using the transfer function:

$$H_{ms}(s) = (K_p + K_v s)e^{-T_{ms}s}, \quad (3.1)$$

where T_{ms} represents the neural transport delay for muscle spindle feedback [36].

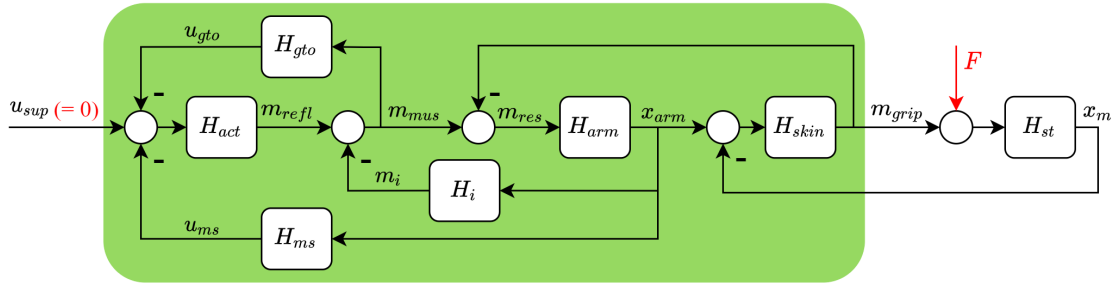


Figure 3.1: The TU Delft neuromuscular model, which includes the red boundary conditions used by De Vlugt et al. [34] to identify the neuromuscular characteristics.

3.1.2. Golgi tendon organs

As the name suggests, the Golgi tendon organs (GTOs) are proprioceptors located on the tendons of muscles. These 'force sensors' provide information to the CNS about the force exerted by a muscle, which assists with postural control and provides reflexive feedback that prevents excessive muscle contraction. Analogous to the muscle spindle dynamics from Equation 3.1, the behavior of GTOs can be approximated by a gain and a neural transport delay (see Equation 3.2);

$$H_{gto}(s) = K_f e^{-T_{gto}s} \quad (3.2)$$

3.1.3. Intrinsic arm properties

The motion of an arm holding on to a side stick is determined by the resultant force acting upon the arm, combined with the inertial properties of the arm. As the side stick only moves laterally in the presented task, the motion of the arm can be approximated by a rotation of the lower arm around a vertical axis located at the elbow [37]. This allows us to represent the physical properties of the arm as a rotational inertia (I_{arm}), combined with effective rotational spring (K_i) and damper (B_i) terms. In line with this assumption, it makes sense to express any forces produced by, or imposed on the arm as moments around this rotational axis.

While it is apparent that the rotational inertia term is defined by the collective body mass of the right arm, the effective spring and damper properties are defined by two other factors. On the one hand, the combination of connective tissues surrounding the fascicles and tendons provide spring and damper properties at all times. On the other hand, the level of muscle cocontraction may also impact the effective spring and damper properties of the arm. This occurs when the agonist and antagonist muscle around a joint are contracted with equal force, i.e., the muscle pair is 'tensed up' by the human controller.

Moreover, the arm is rotated by the sum of moments produced inside the arm minus the external moment induced on the arm by the side stick. In other words:

$$x_{arm} = m_{res} H_{arm}(s) = (m_{mus} - m_{grip}) \left(\frac{1}{I_{arm} s^2} \right), \quad (3.3)$$

where:

$$m_{mus} = m_{refl} - m_i = m_{refl} - (K_i + B_i s) x_{arm} \quad (3.4)$$

3.1.4. Muscle activation

Muscle activation encompasses the transition from signals generated in motor neurons to the production of muscle force m_{mus} , the term in Equation 3.4 that still lacks explanation. The activation of the motor neurons occurs at the spinal cord as the sum of proprioceptive sensor feedback and conscious, supraspinal control originating from the motor cortex (see Equation 3.1.4). This neural signal causes the myofibrils in muscle fibers to contract [38], which effectively exerts a force on the skeleton. According to De Vlugt, this behavior can be estimated accurately by means of a second-order system, which results in Equation 3.5 [39];

$$m_{refl} = u_{tot} H_{act}(s) = u_{tot} \left(\frac{1}{\frac{1}{\omega_{act}^2} s^2 + 2 \frac{b_{act}}{\omega_{act}} s + 1} \right), \quad (3.5)$$

where:

$$u_{tot} = u_{sup} - u_{ms} - u_{gt0} \quad (3.6)$$

3.1.5. Skin dynamics

The transition from arm motion to a moment exerted on the manipulator occurs in the skin of the hand. While the relative motion between the hand and the side stick is small, Van Paassen [33] suggests that the moment exerted on the manipulator can be expressed by this relative motion, combined with a spring-damper model of the interface (i.e., the skin);

$$m_{grip} = (x_{arm} - x_m) H_{skin}(s) = (x_{arm} - x_m) (K_{skin} + B_{skin} s) \quad (3.7)$$

3.2. Modelling cognitive and nonlinear behavior

The model presented in Figure 3.1 provides a detailed description of how manipulator movements induce reflexive grip force and how cognitive commands are translated into grip force. To fully describe the HC's control behavior, a description is needed for how the cognitive, supraspinal target signal u_{sup} comes to be. This cognitive signal is the result of the HC visually perceiving the current tracking error, and determining where the manipulator should move next.

Since this thesis focuses on the interaction between the active stick and reflexive control behavior, the cognitive equalization of the perceived tracking error e is approximated by the widely-used simplified precision model introduced by McRuer and Jex [31]. The visual perception delay T_{visual} is estimated to be 0.25 seconds [40]. The analytical expression for this delay is approximated by a second-order 0.25 s Padé filter:

$$H_{visual}(s) = e^{-T_{visual}s} \approx \frac{s^2 - 24s + 192}{s^2 + 24s + 192} \quad (3.8)$$

The HC's behavior is now fully described, albeit with merely linear approximations for all the components/processes involved. Many of the simple descriptions of HCs add a remnant (i.e., colored noise) to the HC's control output, to account for any nonlinear behavior that may occur.

Figure 3.1 shows how the human response is modelled in a more nuanced way than simply one transfer function, which is why it makes sense to give the sources of nonlinear behavior a similar treatment. The sources of nonlinear behavior are identified and individually assessed as follows:

1. **Sensors providing nonlinear or noisy feedback signals.** Various sources approximate the proprioceptors in experimental settings comparable to the one at hand as linear sensors without any noise term [33] [39] [41], which is why the same approach is taken in this report.
2. **Nonlinear equalization of the perceived tracking error e .** This phenomenon was already studied over 50 years ago by Levison [42], who found out that the spectral shape of the noise signal injected at the perceived error e depends on the system dynamics that the HC is trying to control (i.e., the controlled element or CE dynamics). In general, this noise term can be considered as colored noise, i.e., white noise that is sent through a shaping filter. Levison concluded that CE dynamics resembling K , $\frac{K}{s}$ and $\frac{K}{s^2}$ resulted in white, first-order lag and integrator-shaped forming filters, respectively. These findings are supported by recent research conducted by Van der El [43], who also managed to quantify the parameters that define these forming filters for the fundamental compensatory, pursuit and preview tracking tasks. This includes the following two findings: 1) the noise term for single and double integrator CE dynamics can both be modelled as a first order lag, with corner frequencies $\omega_{c,n,\frac{K}{s}} = 10 \text{ rad/s}$ and $\omega_{c,n,\frac{K}{s^2}} = 0.1 \text{ rad/s}$, respectively and 2) the noise injected at the error has approximately

10% of the power of the perceived error signal, in other words the local signal-to-noise ratio (SNR) $\frac{\sigma_e^2}{\sigma_{n,c}^2} \approx 10$ [43].

To determine what values properly represent the HC's cognitive nonlinear behavior, one needs to consider the effective CE dynamics that the HC experiences and responds to. In the situation of the passive stick this is simply the aircraft roll dynamics H_c which, as can be seen in Equation 2.4, are a second order system. The effective CE dynamics experienced by the HC with the active stick and its roll rate feedback, on the other hand, are a first order system, as is explained in Section 2.5.3 and Figure 2.7. This means that the cognitive noise for the passive and active stick are best estimated by white noise that is filtered by a first order lag with corner frequencies $(\omega_{c,n})_{pas} = 0.1$ rad/s and $(\omega_{c,n})_{act} = 10$ rad/s, respectively. Equation 3.9 shows the probability density function (PDF) related to every discrete variable of the noise term in the simulations, where W_n represents the cognitive noise intensity. Furthermore, Equation 3.10 provides the definition of the shaping filter supported by Levison [42] and Van der El [43].

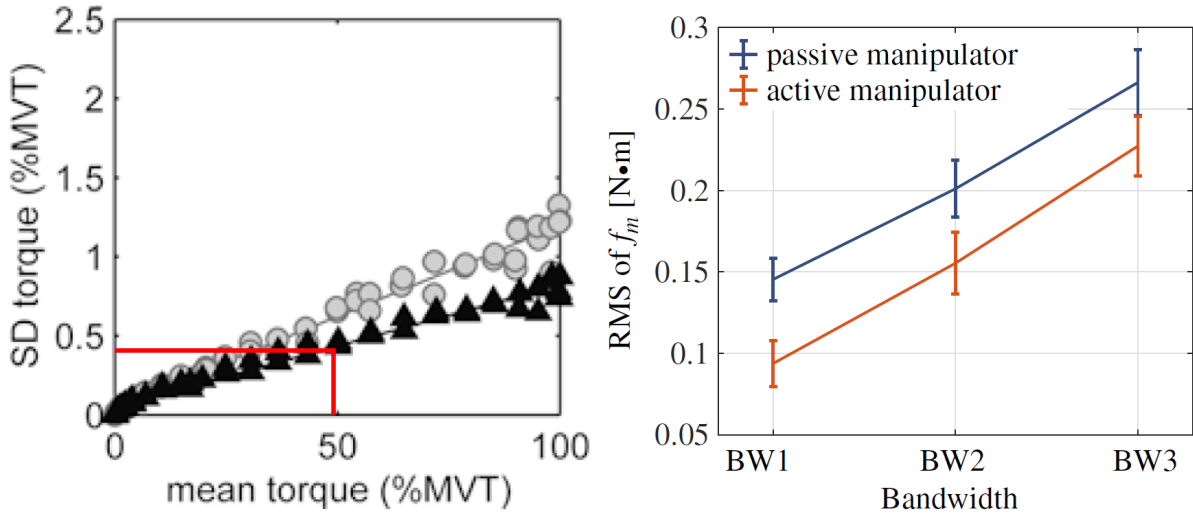
$$f_{f_n[k]}(x) = \sqrt{W_n} \cdot \mathcal{N}(0, 1) \quad (3.9)$$

$$H_n(s) = \frac{1}{\frac{1}{\omega_{c,n}}s + 1} \quad (3.10)$$

3. **Inaccuracies in the execution of a commanded grip force (i.e., motor noise).** Kleinman argued that motor noise can be modelled as Gaussian white noise [44]. Hamilton [45] has quantified the presence of such motor noise as a function of both the mean torque and the amount of motor units present in a muscle (i.e., muscle strength). In the simulations, a distinction is made between a typical 'weak' and 'strong' muscle, whose maximum voluntary torques (MVTs) are 1.79 Nm and 6.79 Nm, respectively. Assuming that the lower arm purely rotates around the elbow and that there is a distance of 0.30 m between the elbow and the side stick, it is safe to conclude that the ensemble of muscles that generates the sideways motion of the stick can be considered as 'strong' (as it would require a sideways force of $> (6.79/0.30)/9.81 = 23$ N at the side stick, which is easily attainable for the average person). This means that the black graph from Figure 3.2a is most helpful to get an impression of the motor noise intensity. The largest average torque estimated in Fu's experimental runs with a 95% confidence interval was around 0.29 Nm, which occurred for the passive stick at the third signal bandwidth (see Figure 3.2b). Such a force would correspond with $100 \cdot (0.29/0.090)/6.79 = 48\%$ MVT. This results in a local SNR of $\frac{\sigma_{mgrip}^2}{\sigma_{n,m}^2} \approx \frac{1}{0.4/100} = 250$. From this it is evident that motor noise has a marginal impact in this situation, which is why it can be omitted from the model.
4. **Operator-centered variables presented by McRuer and Jex [31]** that affect the HC's mental and / or physical state (e.g., being fatigued, stressed, distracted or unmotivated). These undesirable, non-stationary phenomena are inherently difficult to quantify in a model, which is why this will not be done. Instead, the experiment will be designed such that these phenomena will have a minimal chance of impacting the experimental outcome.

3.3. Unification of the theory to model the experiment

The information presented in Sections 3.1, 3.2 and Figure 2.2 was combined to form the active stick model, the schematics of which are demonstrated in Figure 3.3c. This model is used to make observations about the control behavior exhibited by participants from Fu's experiment [14] in Chapter 4, and will play a central role in generating predictions for the new scenarios that are to be tested for the active stick. Figures 3.3a and 3.3b show the schematics of the passive stick and force stick, respectively, as a final demonstration to clarify what the fundamental configurations have in common and what sets them apart.



(a) Simulation of muscle torque standard deviation (i.e., square root of motor noise intensity) as a function of % mean voluntary torque for a weak (gray) and strong (black) muscle [45]. For the experiment at hand, a worst-case scenario noise standard deviation of 0.4% MVT has been identified and indicated in red.

(b) The $RMS(m_{grip})$ values reported with a 95% confidence interval by Fu [14].

What the configurations have in common are the stimuli on which the HC's behavior is based: the visually perceived error e for the cognitive response, and the conscious command signal u_{sup} and stick position x_m for the neuromuscular response. What sets them apart is the way x_m is related to the rest of the control system. As explained in Section 2.1, the passive manipulator moves to a certain position x_m , based on the force the HC applies on the manipulator and the stick's mechanical properties. In this situation, the value measured for x_m is what drives the aircraft's control surfaces. The active stick operates in a fundamentally different way, as is explained in Section 2.3. In this case, the force that the HC applies on the manipulator is what drives the aircraft's control surfaces and x_m is imposed on the HC using servo motors, that base said stick position on the motion of the aircraft.

Finally, Figure 3.3b shows the schematics of the configuration that bridges the conceptual gap between the other two: the force stick. Like the active stick, it involves a manipulator which translates the applied force to a control signal, however its position remains fixed in the neutral position (in other words, it functions as an active stick where $K_{\dot{\phi}} = 0$).

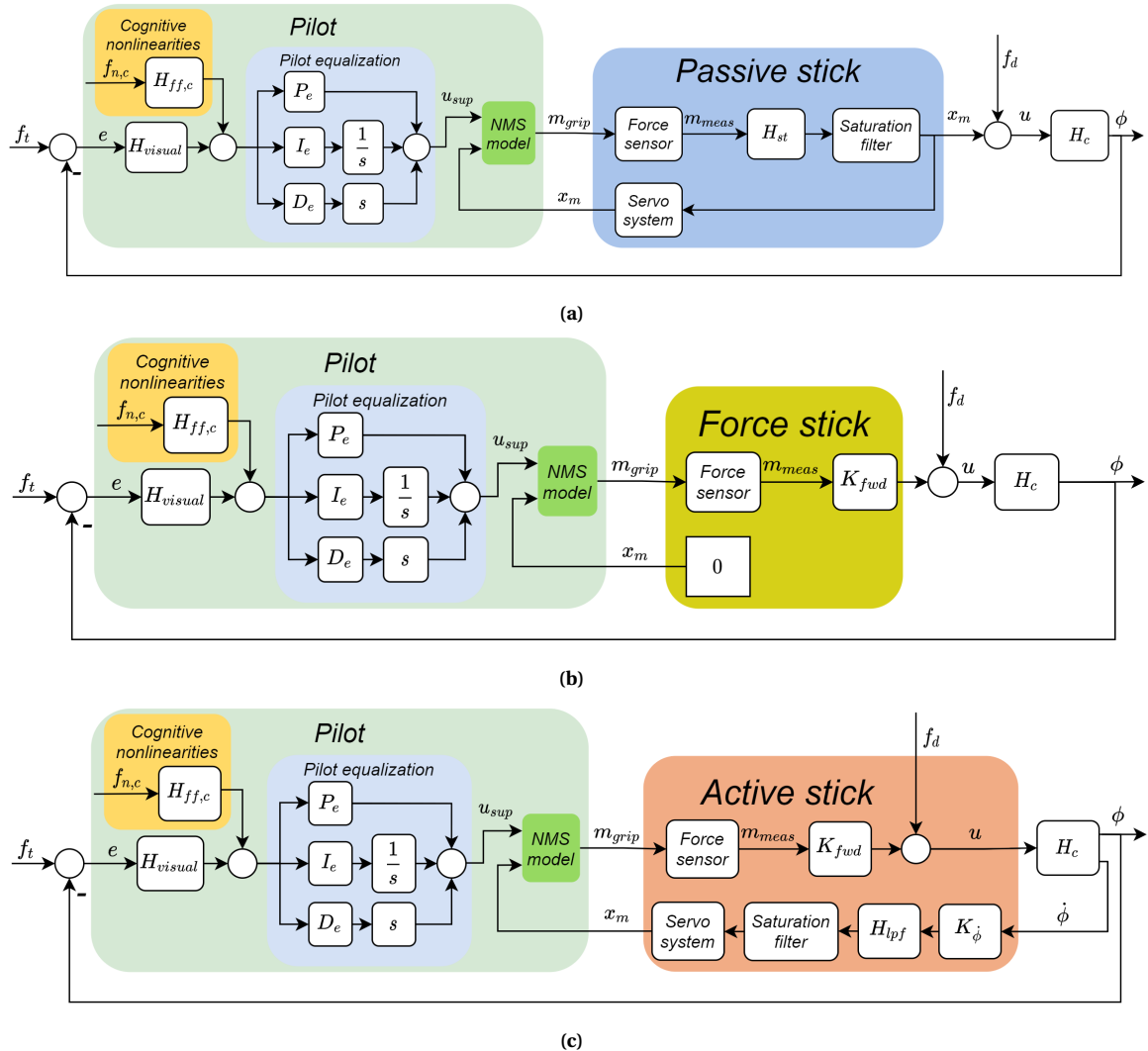


Figure 3.3: A schematic representation of the (a) passive (b) force and (c) active stick model, where the green 'NMS model' block acts as a small substitute for Figure 3.1. The force stick model bridges the conceptual gap between the passive and active stick that were introduced in Sections 2.1 and 2.3, respectively, but the active stick model is the one that will be focused on for the remainder of this thesis.

4

Applying the model and devising a test strategy

With the model of Chapter 3 in place, a wide array of testing conditions can be simulated and ultimately a proposal can be made for the tuning procedure of the active stick. To reach that point, however, a grounded argument needs to be made for the value of all the parameters that define the model and the observations leading up to the proposed tuning procedure and testing conditions. Figure 4.1 provides an overview of how the sections of this chapter have been organized to suit this approach, from the analytical derivation of the active stick model's top level transfer functions to the analysis of the simulation output and, finally, the proposed tuning procedure and testing conditions.

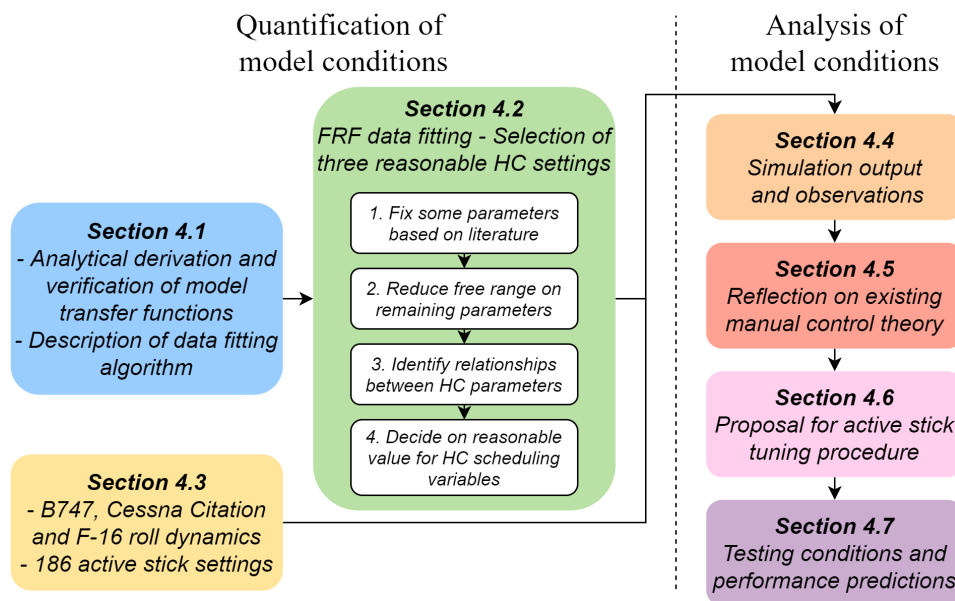


Figure 4.1: An overview of the workflow and the way content is organized in Chapter 4.

4.1. Preparation of the data fitting algorithm

The Delft neuromuscular model that is presented in Section 3.1 is characterized by the twelve parameters shown in Equations 3.1 to 3.7. Combined with the four parameters that characterize the HC's cognitive response (P_e , I_e , D_e and T_{visual}), this brings the total number of HC parameters to sixteen. This number, combined with the adaptive nature for which HCs are known, makes the quantification of a reasonable relaxed, average and tense human controller setting particularly challenging when it comes to simulating testing conditions. Luckily, the experimental data generated by Fu [14] provides us the opportunity to estimate said parameters, by fitting the active stick model on the existing Bode plots that represent the HC's open- and closed-loop responses for tracking the

target signal f_t (i.e., $H_{t,OL}(s) = \frac{\Phi(s)}{E(s)}$ and $H_{t,CL}(s) = \frac{\Phi(s)}{F_t(s)}$) and rejecting the disturbance signal f_d (i.e., $H_{d,OL}(s) = \frac{U_p(s)}{F_d(s)}$ and $H_{d,CL}(s) = \frac{\Phi(s)}{F_d(s)}$).

Before any data fitting can take place, however, the transfer functions of the open- and closed-loop target tracking and disturbance rejection response need to be derived from the model first. Section 4.1.1 merely shows the outcome of this process, but the full derivation can be found in Appendix A. This also includes a derivation and verification of the passive stick model transfer functions which, although not of direct value to this thesis, had been made at an earlier stage in the project and could potentially serve future research. Once the analytical expressions are derived and verified, the algorithm that estimates the HC parameters using said expressions can be explained, which is done in Section 4.1.2.

4.1.1. Analytical derivation and verification of model transfer functions

Upon closer inspection of the active stick model shown in Figure 3.3c, the open- and closed-loop target tracking responses have been determined analytically. Given that $H_{skin} = H_1$, $I_{arm} = H_2$, $H_i = H_3$, $H_{ms} = H_4$, $H_{gto} = H_5$ and $H_{act} = H_6$ and that:

$$\begin{aligned} Q &= H_{1pf} H_{hfb} \\ \Gamma &= 1 + H_1 H_2 \\ \Delta &= H_{visual} \left(P_e + \frac{I_e}{s} + D_e s \right) \\ \Theta &= 1 + H_6 H_5 \\ \Lambda &= H_6 H_4 H_2 + H_3 H_2 \end{aligned}$$

The open- and closed-loop target tracking responses are defined as:

$$\frac{\Phi(s)}{E(s)} = \frac{H_c K_{fwd} H_1 H_2 H_6 \Delta}{(\Gamma + H_1 Q H_c K_{fwd})(\Theta + \Lambda) - H_1 H_2 \Lambda} \quad (4.1)$$

$$\frac{\Phi(s)}{F_t(s)} = \frac{H_c K_{fwd} H_1 H_2 H_6 \Delta}{(\Gamma + H_1 Q H_c K_{fwd})(\Theta + \Lambda) - H_1 H_2 \Lambda + H_c K_{fwd} H_1 H_2 H_6 \Delta} \quad (4.2)$$

The open- and closed-loop disturbance rejection responses are defined as:

$$\frac{U_p(s)}{F_d(s)} = \frac{H_1 H_c K_{fwd}}{\Gamma} \left(H_1 H_2 Q - \frac{H_2 H_6 \Delta \Gamma + \Lambda H_1 H_2 Q}{\Gamma \Theta + \Lambda} - Q \Gamma \right) \quad (4.3)$$

$$\frac{\Phi(s)}{F_d(s)} = \frac{\Gamma}{\Gamma - H_1 H_c K_{fwd} \left(H_1 H_2 Q - \frac{H_2 H_6 \Delta \Gamma + \Lambda H_1 H_2 Q}{\Gamma \Theta + \Lambda} - Q \Gamma \right)} \quad (4.4)$$

To verify these transfer functions, they have been plotted with the Bode plots that were generated from the models directly using the Model Linearizer toolbox in Simulink. As can be seen in Figures 4.2a and 4.2b, the resulting plots from the two methods coincide, which provides the needed confidence about the correctness of the analytical expressions.

4.1.2. The data fitting algorithm

In summary, the algorithm **Datafitter.m** makes use of the MATLAB routine **fmincon.m**, which optimizes the sum of squares cost value C that is calculated during every iteration by **activeStickCostfunc.m**. It operates as follows:

1. Import active stick model constants.
2. Define the vector to be optimized: $\vec{v} = [P_e, I_e, D_e, K_{skin}, B_{skin}, K_i, B_i, K_p, K_v, K_f]$.
3. Apply boundary conditions to the elements of \vec{x} .
4. Generate an initial guess for $\vec{v} \Rightarrow \vec{v}_0$, where every element of \vec{x}_0 is randomly selected from a uniform distribution spanning from the lower to the upper bound of all respective variables.
5. Fmincon.m(**activeStickCostfunc.m**, \vec{v}_0 , BCs of \vec{v}). With every \vec{v} tested by fmincon.m, **activeStickCostfunc.m**:

- (a) Calculates the resulting $H_{t,OL}(s)$, $H_{t,CL}(s)$, $H_{d,OL}(s)$ and $H_{d,CL}(s)$, using the analytical expressions shown in Section 4.1.1.
- (b) Calculates the phasors of these transfer functions at the frequencies tested by Fu [14] (see Tables 2.2 and 2.3).
- (c) Imports the experimental frequency response data generated by Fu [14]. This includes information about the mean value of all data points, as well as their standard deviation.
- (d) Calculates the phasor belonging to every data point's mean value (\vec{x}_μ), as well as the one belonging to every data point's $+1\sigma$ value (i.e., $\vec{x}_{+1\sigma}$). Then, the difference vector $\vec{x}_\mu - \vec{x}_{+1\sigma}$ is calculated, which is clarified visually in Figure 4.3.
- (e) Calculates the average difference vector norm $\|\vec{x}_\mu - \vec{x}_{+1\sigma}\|$ for every Bode plot (i.e., target OL, target CL, disturbance OL and disturbance CL) separately, as well as the standard deviation belonging to those data sets.
- (f) Assigns a weight to every data point, which is based on the relative size of every $\|\vec{x}_\mu - \vec{x}_{+1\sigma}\|$ in a given data set and the standard deviation of said data set. In other words: the more uncertain a data point is compared to the other points in that Bode plot from Fu (e.g., the second point in the OL target tracking Bode plot), the lower the priority becomes for the data fitter algorithm to fit the model on that Bode plot at that specific frequency.

When $\|\vec{x}_\mu - \vec{x}_{+1\sigma}\|$ of a certain data point is perfectly average compared to the other nine points in that Bode plot, its weight will be 1. When $\|\vec{x}_\mu - \vec{x}_{+1\sigma}\|$ is one σ greater than the average of that set (i.e., a relatively inaccurate point), its weight will be 0.5. When $\|\vec{x}_\mu - \vec{x}_{+1\sigma}\|$ is one σ smaller than the average of that set (i.e. a relatively accurate point), its weight will be 2. To summarize algebraically, suppose for a data point in a given Bode plot that:

$$\|\vec{x}_{diff}(N)\| = \|\vec{x}_\mu(N) - \vec{x}_{+1\sigma}(N)\| \quad (4.5)$$

Then the average size and standard deviation of the difference vector for a given Bode plot can be formulated as:

$$\mu_{\|\vec{x}_{diff}\|} = \sum_{N=1}^{10} \frac{\|\vec{x}_{diff}(N)\|}{10} \quad (4.6)$$

$$\sigma_{\|\vec{x}_{diff}\|} = \sqrt{\frac{\sum \left| \|\vec{x}_{diff}\| - \mu_{\|\vec{x}_{diff}\|} \right|^2}{10}} \quad (4.7)$$

For the ten data points in that Bode plot then holds that:

$$W(N) = 2^{-Z_{\|\vec{x}_{diff}\|}(N)}, \quad (4.8)$$

where:

$$Z_{\|\vec{x}_{diff}\|}(N) = \frac{\|\vec{x}_\mu(N) - \vec{x}_{+1\sigma}(N)\| - \mu_{\|\vec{x}_{diff}\|}}{\sigma_{\|\vec{x}_{diff}\|}} \quad (4.9)$$

As is clear from the explanation as well as the equations, the weights for every data point remain *constant*, regardless of what \vec{v} is currently being tested by **fmincon.m**.

- (g) Calculates the difference vector between the phasors generated at step (b) and the mean phasors derived from Fu's experimental data at step (d). The norm of all separate difference vectors is squared, multiplied by their corresponding $W(N)$ and added up to form the total cost C that effectively forms the least squares sum that is being optimized by **fmincon.m**.

4.2. Quantification of human control behavior

As is shown in Figure 4.1, the determination of three reasonable HC settings required a methodical approach that involved several steps. First off, the parameters for which relatively consistent values are reported in literature are assumed to be constant (I_{arm} and visual response time T_{visual}). This also includes the parameters that characterize the neural signal activation (ω_{act} and b_{act}) and neural transport delay (T_{ms} and T_{gto}), as researched by Schouten [32]. Effectively, this reduced the number of free HC parameters from sixteen to ten.

Table 4.1 provides an overview of the boundary conditions that were in place at the start of this procedure, as well as the sources on which they were based. It should be noted that at this point, the direct relationship between K_p , K_v and K_f for the fundamental position, force and relax task (and any task in between) as proposed by Bhoelai [46] was still respected. Whereas this relationship also extended to K_i , the large difference in values reported for this parameter by Bhoelai [46] and Lasschuit [47] are the reason why K_i was set as an independent variable.

Table 4.1: The quantified human controller parameters after iteration 0.

Category	Parameter	Symbol	Value	Unit	Source
Skin dynamics	Stiffness	K_{skin}	[165,400]	[Nm/rad]	Paassen [37], Lam [48]
	Damping	B_{skin}	[0.5,5]	[Nms/rad]	Lasschuit [47]
Intrinsic arm dynamics	Inertia	I_{arm}	0.01	[Nms ² /rad]	Lasschuit [47]
	Damping	B_i	[0.05,1]	[Nms/rad]	Lasschuit [47]
	Stiffness	K_i	[3,11]	[Nm/rad]	Lasschuit [47], Bhoelai [46]
Muscle spindle dynamics	Muscle stretch	K_p	PT: 9, RT: 10^{-10} , FT: -6	[Nm/rad]	Bhoelai [46]
	Muscle stretch rate	K_v	PT: 2, RT: 10^{-10} , FT: 3	[Nms/rad]	Bhoelai [46]
	Neural transport delay	T_{ms}	0.025	[s]	Schouten [32]
Golgi tendon organ dynamics	Muscle force	K_f	PT: -1.5, RT: 10^{-10} , FT: 1.5	[-]	Bhoelai [46]
	Neural transport delay	T_{gto}	0.025	[s]	Schouten [32]
Neuromuscular activation dynamics	Corner frequency	ω_{act}	13.823	[rad/s]	Schouten [32]
	Damping	b_{act}	0.7071	[-]	Schouten [32]
Cognitive response	Proportional gain	P_e	[-15,0]	[-]	Estimated per run
	Integrator gain	I_e	[-15,0]	[-]	
	Differentiator gain	D_e	[-15,0]	[-]	
	Visual response time	T_{visual}	0.25	[s]	Jain [40]

4.2.1. Reduction of upper and lower bounds on remaining parameters

After running the data fitting algorithm presented in Section 4.1.2 in combination with the experimental data for all three bandwidths tested by Fu [14], the following initial observations could be made:

- The skin stiffness K_{skin} was reported earlier at large, yet varying values [37] [48]. The frequency response plots show, however, that its exact value is inconsequential for the HC's control behavior and performance in the frequency band that the HC is exposed to in the experiment at hand. This is why K_{skin} is assumed to be 165 Nm/rad, as reported by Lam [48].
- The skin damping B_{skin} was reported by Lasschuit [47] with relatively large uncertainty earlier. Whereas the cost value C seemed to be insensitive to changes in B_{skin} at some settings (particularly when $K_i \leq 4$), it could sometimes make the difference for closed-loop stability of the system and was maximized in the majority of the scenarios. This is why B_{skin} is assumed to be 5 Nms/rad, which is at the higher end of the estimates reported by Lasschuit [47].
- The intrinsic arm damping B_i is consistently minimized, as it has a great impact on the fit quality of the disturbance rejection FRF in particular. This is why it is set at 0.05 Nms/rad, which is at the lower end of the estimates reported by Lasschuit [47].
- The values reported for the intrinsic arm stiffness K_i by Lasschuit [47] greatly improve the quality of the fit compared to the values reported by Bhoelai [46], which is why the upper and lower limits for K_i are narrowed down in accordance with Lasschuit's measurements ($3 < K_i < 11$ becomes $3 < K_i < 6.5$ [Nm/rad]). By adhering to Lasschuit's values for K_i , the validity of the refined proprioceptor gain limits reported by Bhoelai [46] is jeopardized. This is why the dependencies between K_i , K_p , K_v and K_f are removed, and the proprioceptor upper and lower gain limits are relaxed to the absolute limits determined by Bhoelai at an earlier stage.
- Closed-loop stability of the system seems to depend on $|P_e|$ being smaller or equal to ≈ 4 . This threshold seems to decrease mildly for increasing intrinsic arm stiffness K_i .
- Crossover characteristics as well as time-domain performance seem to drop in accuracy considerably when $|P_e| < 1$.

With this information, the amount of free variables in the pilot model is reduced to seven: the intrinsic arm stiffness K_i , the proprioceptor gains K_p , K_v and K_f , and the cognitive response characterized by P_e , I_e and D_e . Table 4.2 summarizes how the parameter bounds have changed.

4.2.2. Identification of relations between human controller parameters

With the reduced parameters bounds, two sets of scenarios were tested for the intermediate and large bandwidth tested by Fu [14]: 1) $K_i = 4$, $P_e = -1, -1.5, \dots, -4$ and 2) $P_e = -3$, $K_i = 3, 3.5, \dots, 6.5$. These scenarios were tested for the situations of P-, PD- and PID-control, to assess the impact and relevance of D_e and I_e with respect to the quality of the fit. The outcome of these tests is summarized in Tables 4.3 and 4.4.

Since the combination of $K_i = 4$ and $P_e = -4$ resulted in either a marginally stable or unstable system in all scenarios, its distorted results have been omitted from Table 4.3. Also, Figure 4.4 demonstrates how certain tested settings resulted in one disturbance rejection gain crossover point, whereas others resulted in multiple ones. For these situations, the point with the minimal stability margin has been recorded as a second crossover point, of which the most extreme values made it to Tables 4.3 and 4.4.

Table 4.2: *The quantified human controller parameters after iteration 1.*

Category	Parameter	Symbol	Value	Unit	Source
Skin dynamics	Stiffness	K_{skin}	165	[Nm/rad]	Lam [48]
	Damping	B_{skin}	5	[Nms/rad]	Lasschuit [47]
Intrinsic arm dynamics	Inertia	I_{arm}	0.01	[Nms ² /rad]	Lasschuit [47]
	Damping	B_i	0.05	[Nms/rad]	Lasschuit [47]
	Stiffness	K_i	[3,6.5]	[Nm/rad]	Lasschuit [47]
Muscle spindle dynamics	Muscle stretch	K_p	[-30,30]	[Nm/rad]	Bhoelai [46]
	Muscle stretch rate	K_v	[-5,10]	[Nms/rad]	Bhoelai [46]
	Neural transport delay	T_{ms}	0.025	[s]	Schouten [32]
Golgi tendon organ dynamics	Muscle force	K_f	[-20,20]	[-]	Bhoelai [46]
	Neural transport delay	T_{gto}	0.025	[s]	Schouten [32]
Neuromuscular activation dynamics	Corner frequency	ω_{act}	13.823	[rad/s]	Schouten [32]
	Damping	b_{act}	0.7071	[-]	Schouten [32]
Cognitive response	Proportional gain	P_e	[-5,0]	[-]	Estimated per run
	Integrator gain	I_e	[-5,0]	[-]	
	Differentiator gain	D_e	[-5,0]	[-]	
	Visual response time	T_{visual}	0.25	[s]	Jain [40]

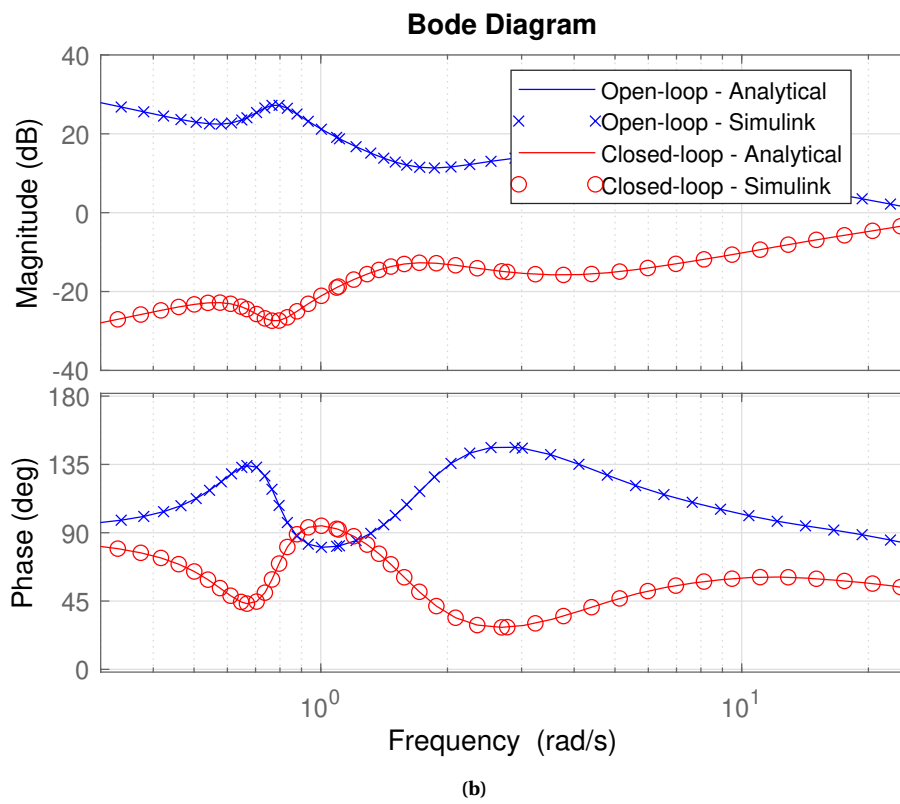
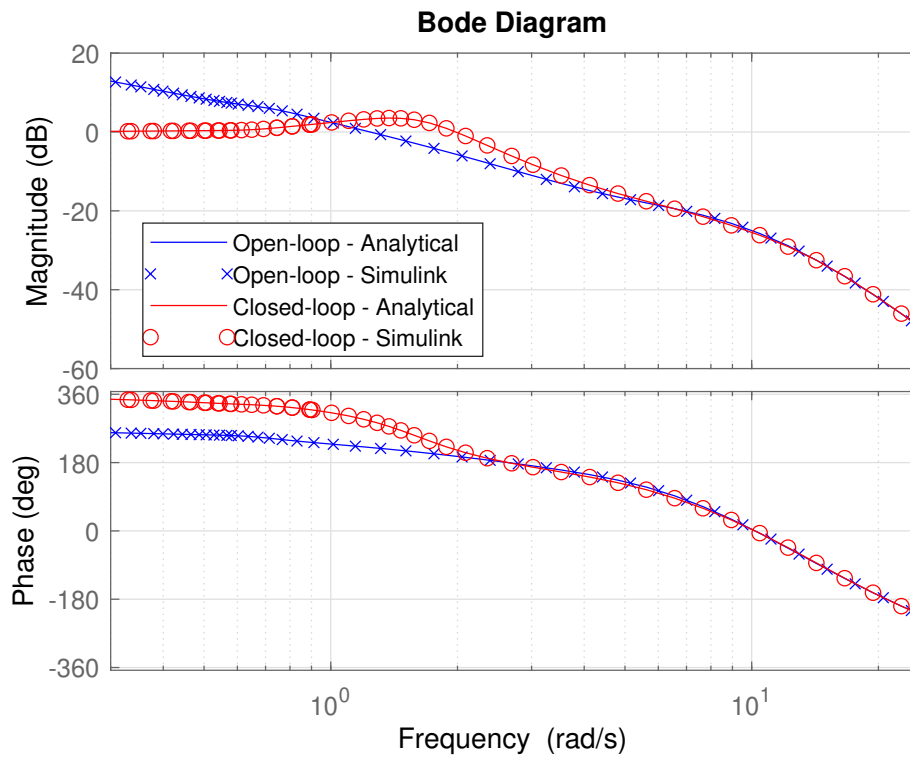


Figure 4.2: Verification of the analytical descriptions for the active stick model, for the open- and closed-loop (a) target tracking and (b) disturbance rejection response.

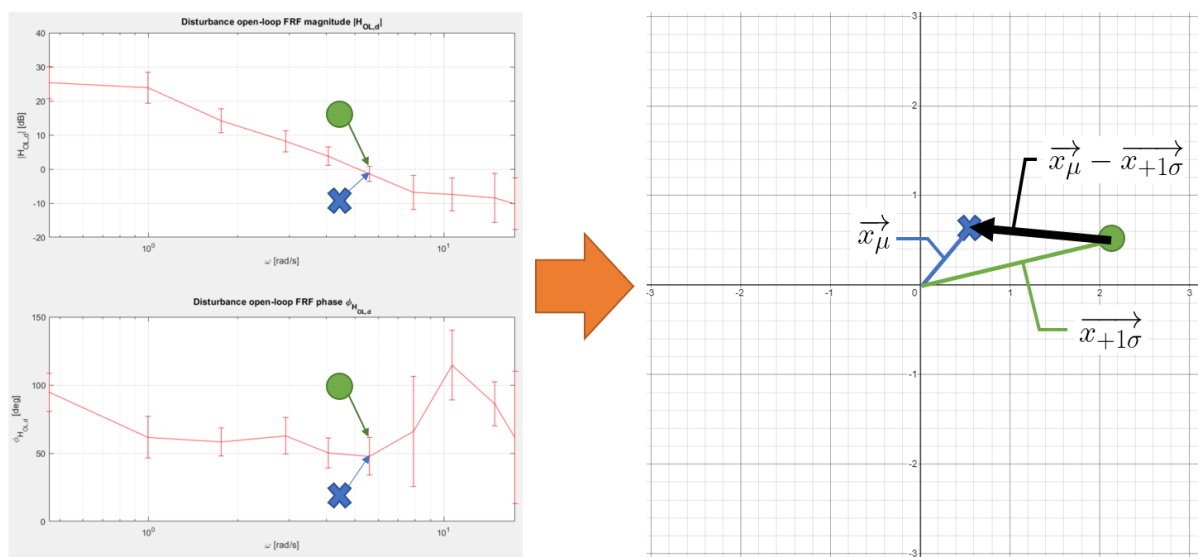


Figure 4.3: A demonstration of how a difference vector is calculated for every experimental frequency response data point generated by Fu [14]. In this example, data point six of ten from the open-loop disturbance rejection Bode plot of Fu's intermediate bandwidth (BW2) is selected.

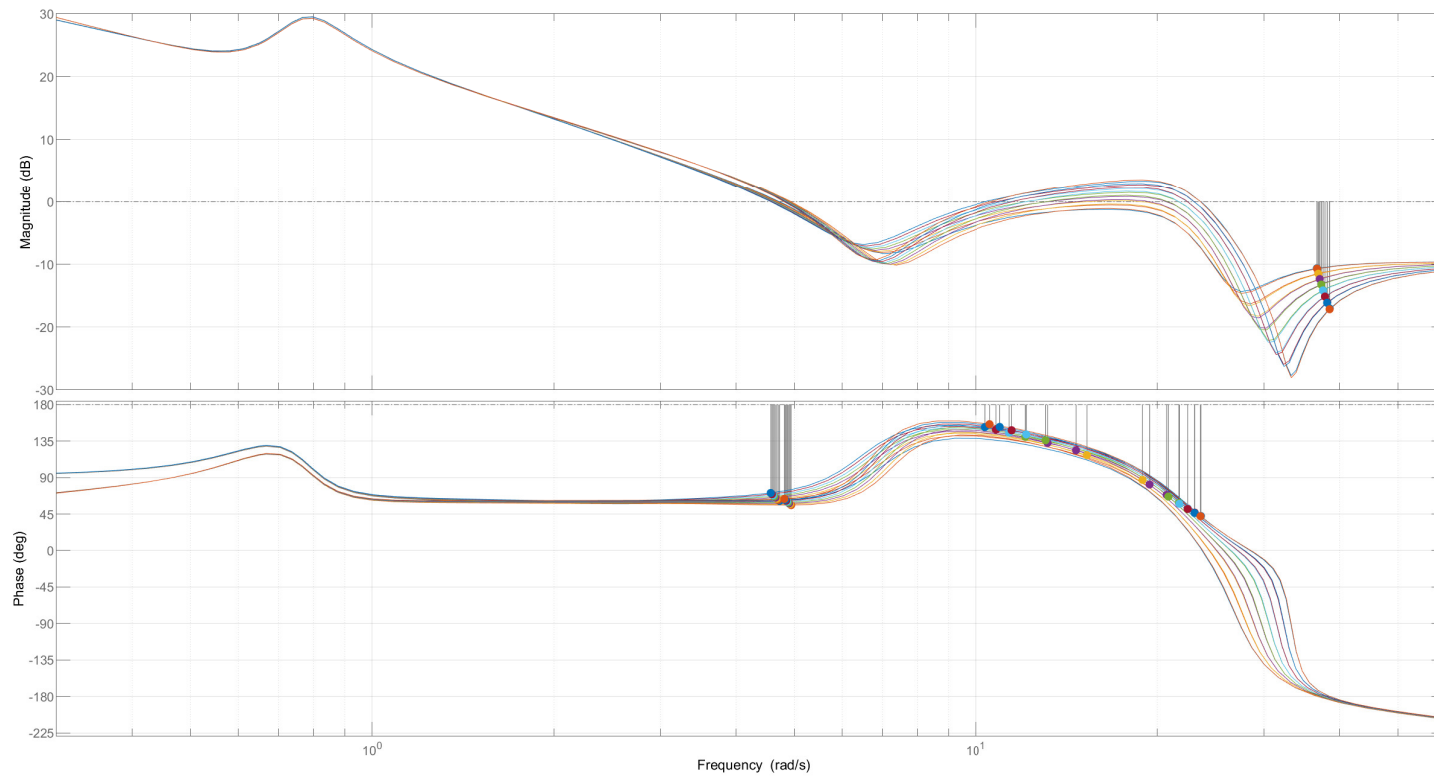


Figure 4.4: Bode plot of the PD and PID open-loop disturbance rejection FRFs summarized in Table 4.4, which demonstrates the presence of multiple gain crossover points at many of the tested settings. For these situations, the most extreme minimal stability margins have been recorded as the second crossover point in Tables 4.3 and 4.4.

P-control vs. PD-control vs. PID-control

- P-control results in a time-domain tracking performance most comparable to the one reported by Fu [14] ($RMS(e)_{Fu} \approx 5.42^\circ$, $4.97 < RMS(e) < 5.51$). The simulated control effort, however, is the furthest off ($RMS(m_{grip})_{Fu} \approx 0.156$ Nm, $0.0456 < RMS(m_{grip}) < 0.0540$).
- The introduction of D_e increases the quality of the fit by a respectable amount ($119 < C < 143$ becomes $77 < C < 92$). The vast majority of this improvement occurs at the closed-loop target tracking response ($50 < C(tCL) < 73$ becomes $5.2 < C(tCL) < 7.2$), along with an improvement of the closed-loop disturbance rejection fit that was already solid ($3.9 < C(dCL) < 7.9$ becomes $1.3 < C(dCL) < 3.0$).
- Interestingly, the crossover characteristics for both target tracking and disturbance rejection improve greatly when D_e is added, despite the apparent lack of improvement in $C(tOL)$ and $C(dOL)$.
- The addition of the integrator I_e considerably increases the quality of the fit ($77 < C < 92$ becomes $13 < C < 20$). The vast majority of the improvement in this case occurs for both open-loop responses ($49 < C(tOL) < 53$ becomes $1.8 < C(tOL) < 3.1$ and $18 < C(dOL) < 29$ becomes $6.9 < C(dOL) < 13$).
- Time- and frequency domain performance remain nearly unchanged when comparing PD- and PID-control, with the exception of a minor increase in $RMS(m_{grip})$ ($0.0613 < RMS(m_{grip}) < 0.108$ becomes $0.0680 < RMS(m_{grip}) < 0.139$). Still, all of the tested settings consistently result in too strong of a tracking performance, whereas the required control effort is consistently too low compared to the experimental data.

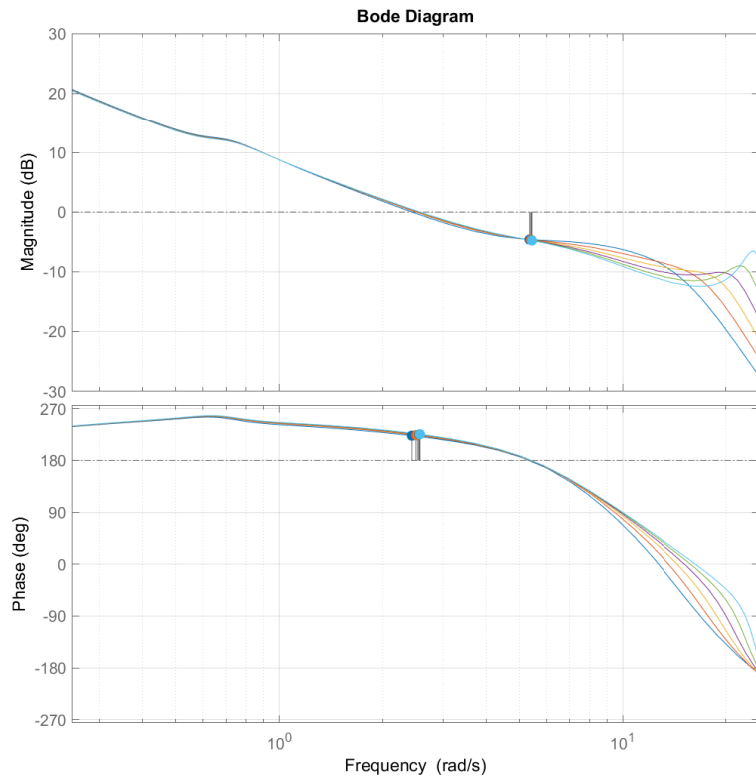
Constant K_i with varying P_e

Within the different control regimes (P-, PD- and PID-control), highly similar performance could be obtained (for the frequency-domain in particular) for a constant K_i and varying P_e . To demonstrate this, Figure 4.5 contains the highly similar Bode plots determined for the PID-control regime, besides from which time-domain performance variations can be summarized as $4.14^\circ < RMS(e) < 4.44^\circ$; 0.0596 Nm $< RMS(m_{grip}) < 0.139$ Nm. To achieve these similar results, the following relations between neuromuscular parameters were observed:

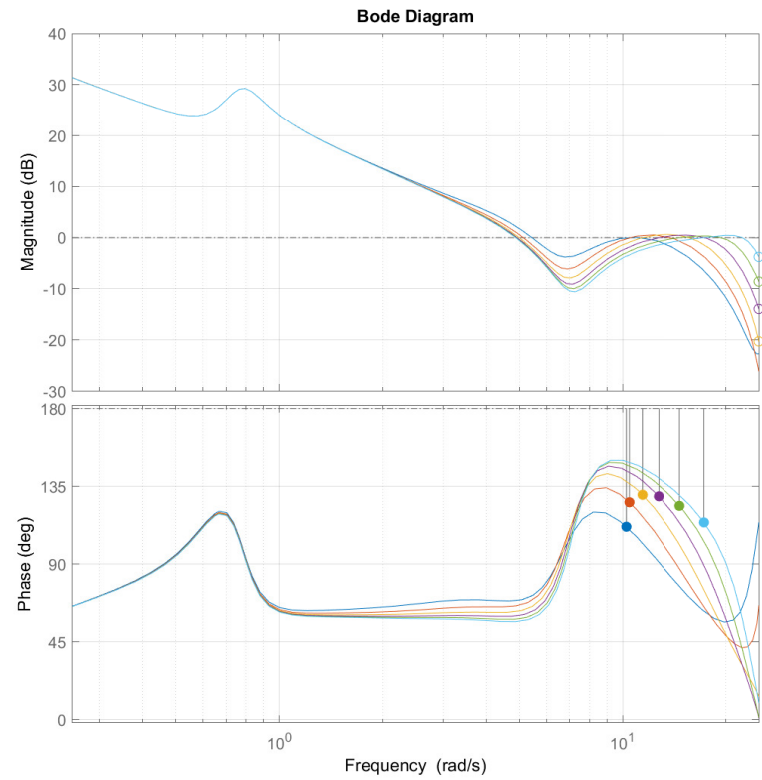
- Both for PD- and PID-control, D_e scales approximately proportional to $\sqrt{P_e}$.
- For PID-control, I_e scales proportional to P_e .
- For all control regimes, a more aggressive cognitive response (i.e., larger values for $|P_e|$, $|I_e|$ and $|D_e|$) resulted in greater values for the muscle spindle gains K_p and K_v . This means that the muscle spindles are set to be more excitatory, which in turn means that both cognitive commands and disturbances from the stick are attenuated more actively by the NMS.
- For all control regimes, a more aggressive cognitive response (i.e., larger values for $|P_e|$, $|I_e|$ and $|D_e|$) resulted in greater values for the Golgi tendon organ gain K_f . This means that the golgi tendon organs are set to be more inhibitory, which in turn means that cognitive commands are attenuated more actively by the NMS, but disturbances from the stick are admitted more easily.

Constant P_e with varying K_i

As was the case in the previous section, highly similar performance could be obtained for a constant P_e and a varying K_i within the different control regimes. The variation in time-domain performance can be summarized as $4.06^\circ < RMS(e) < 4.29^\circ$; 0.0941 Nm $< RMS(m_{grip}) < 0.110$ Nm and Figure 4.9



(a) The open-loop target tracking frequency responses.



(b) The open-loop disturbance rejection frequency responses.

Figure 4.5: Bode plots of all the dynamic systems that the data fitting algorithm converged to, when fitting the model on Fu's intermediate bandwidth data with $P_e = [-3.5, -1]$ and $K_i = 4$.

demonstrates the similarity between the resulting open-loop Bode plots. To achieve the similar results, the following relations between neuromuscular parameters were observed here:

- The combination of a relatively large P_e (≥ 3) and K_i (≥ 4) gives too much disturbance rejection open-loop gain in the high frequencies ($8 < \omega < 25$ rad/s).
- $RMS(e)$ remains comparable, however the $RMS(m_{grip})$ increases notably for a higher K_i .
- $|D_e|$ increases slightly for increasing K_i , which may act as a slight compensation for the reduced neuromuscular amplification through additional cognitive amplification.
- In the case of PID-control, I_e remains nearly unaffected by K_i .
- Muscle spindle gains reduce for higher K_i , thereby becoming more inhibitive. This increases NMS signal amplification through the muscle spindle feedback loop to compensate for the intrinsic arm feedback loop, which has become more excitatory due to the larger K_i .
- Interestingly, GTO gains remain unaffected by changes in K_i .

Table 4.3: An overview of the upper and lower limits reached while fitting the model on the existing experimental data for $K_i = 4$ Nm/rad and $P_e = -1, -1.5, -2, \dots, -3.5$ for Fu's intermediate bandwidth.

		Data Fu BW2 [14]	$K_i = 4$ Nm/rad, $P_e = -1, -1.5, \dots, -3.5$		
			P-control	PD-control	PID-control
Separate costs	C(tOL)		[39, 48]	[49, 53]	[1.8, 3.1]
	C(tCL)		[51, 73]	[5.7, 6.1]	[1.2, 2.4]
	C(dOL)		[18, 23]	[20, 24]	[8.0, 9.2]
	C(dCL)		[4.4, 7.9]	[1.6, 2.6]	[1.0, 1.8]
Total cost C			[121, 143]	[81, 82]	[13.9, 14.4]
	$\omega_{c,t}$ [rad/s]	2.49	[2.05, 2.18]	[2.48, 2.57]	[2.50, 2.57]
	$\phi_{m,t}$ [deg]	42.8	[33.1, 41.3]	[41.4, 43.7]	[43.9, 45.6]
	$RMS(e)$ [deg]	5.42	[4.97, 5.51]	[4.10, 4.17]	[4.14, 4.32]
	$RMS(m_{grip})$ [Nm]	0.156	[0.0456, 0.0540]	[0.0613, 0.108]	[0.0680, 0.139]
	$\omega_{c,d}$ [rad/s]	5.16	[4.33, 12.4]	1) [4.65, 5.00], 2) [10.1, 18.4]	1) [4.88, 5.13], 2) [10.5, 17.3]
	$\phi_{m,d}$ [deg]	-128.9	[-61.3, -103]	1) [-103, -118] 2) [-51.8, -74.6]	1) [-113, -123], 2) [-49.9, -65.8]

Findings summarized

Moreover, similar performance can be obtained when a more aggressive cognitive response (larger $|P_e|$) is coupled with more inhibitive muscle spindles (K_p and K_v decrease in value) and more inhibitive Golgi tendon organs (K_f increases). Such inhibitive settings make the NMS more compliant, but also attenuate cognitive commands. This makes sense when considering the various extreme tasks (PT, RT, and FT), as an HC always needs to find a balance in the intensity of the control behavior. Being able to move the stick around aggressively comes at the cost of experiencing disturbance more aggressively as well.

4.2.3. Definition of three human controller settings

Figures 4.6 and 4.7 show the linear relations through which highly similar performance was obtained. These linear relations have been approximated (as shown in Table 4.5), after which the

Table 4.4: An overview of the upper and lower limits reached while fitting the model on the existing experimental data for $P_e = -3$ and $K_i = 3, 3.5, \dots, 6.5$ Nm/rad for Fu's intermediate bandwidth. Only one gain crossover point existed for some of the open-loop disturbance FRFs, hence the 'N.A.' entries as an extremity of the second crossover points (see Figure 4.4 for visual clarification).

		Data Fu BW2 [14]	$P_e = -3, K_i = 3, 3.5, \dots, 6.5$ Nm / rad		
			P-control	PD-control	PID-control
Separate costs	C(tOL)		[44, 48]	[52.5, 53.0]	[2.4, 3.1]
	C(tCL)		[50, 65]	[5.2, 7.2]	[2.2, 2.5]
	C(dOL)		[16, 24]	[18, 29]	[6.9, 13]
	C(dCL)		[3.9, 7.8]	[1.3, 3.0]	[0.8, 2.0]
Total cost C			[119, 141]	[77, 92]	[13, 20]
	$\omega_{c,t}$ [rad/s]	2.49	[2.13, 2.17]	[2.56, 2.57]	[2.55, 2.58]
	$\phi_{m,t}$ [deg]	42.8	[36.9, 41.6]	[42.9, 43.6]	[45.3, 45.3]
	$RMS(e)$ [deg]	5.42	[4.97, 5.29]	[4.02, 4.16]	[4.06, 4.29]
	$RMS(m_{grip})$ [Nm]	0.156	[0.0502, 0.0533]	[0.0874, 0.0976]	[0.0941, 0.111]
	$\omega_{c,d}$ [rad/s]	5.16	1) [4.40, 5.00], 2) [N.A., 21.1]	1) [4.57, 4.73], 2) [N.A., 15.3]	1) [4.80, 4.94], 2) [N.A., 14.7]
	$\phi_{m,d}$ [deg]	-128.9	1) [-66, -101], 2) [N.A., -117]	1) [-109, -119], 2) [N.A., -62.3]	1) [-116, -124], 2) [N.A., -56.2]

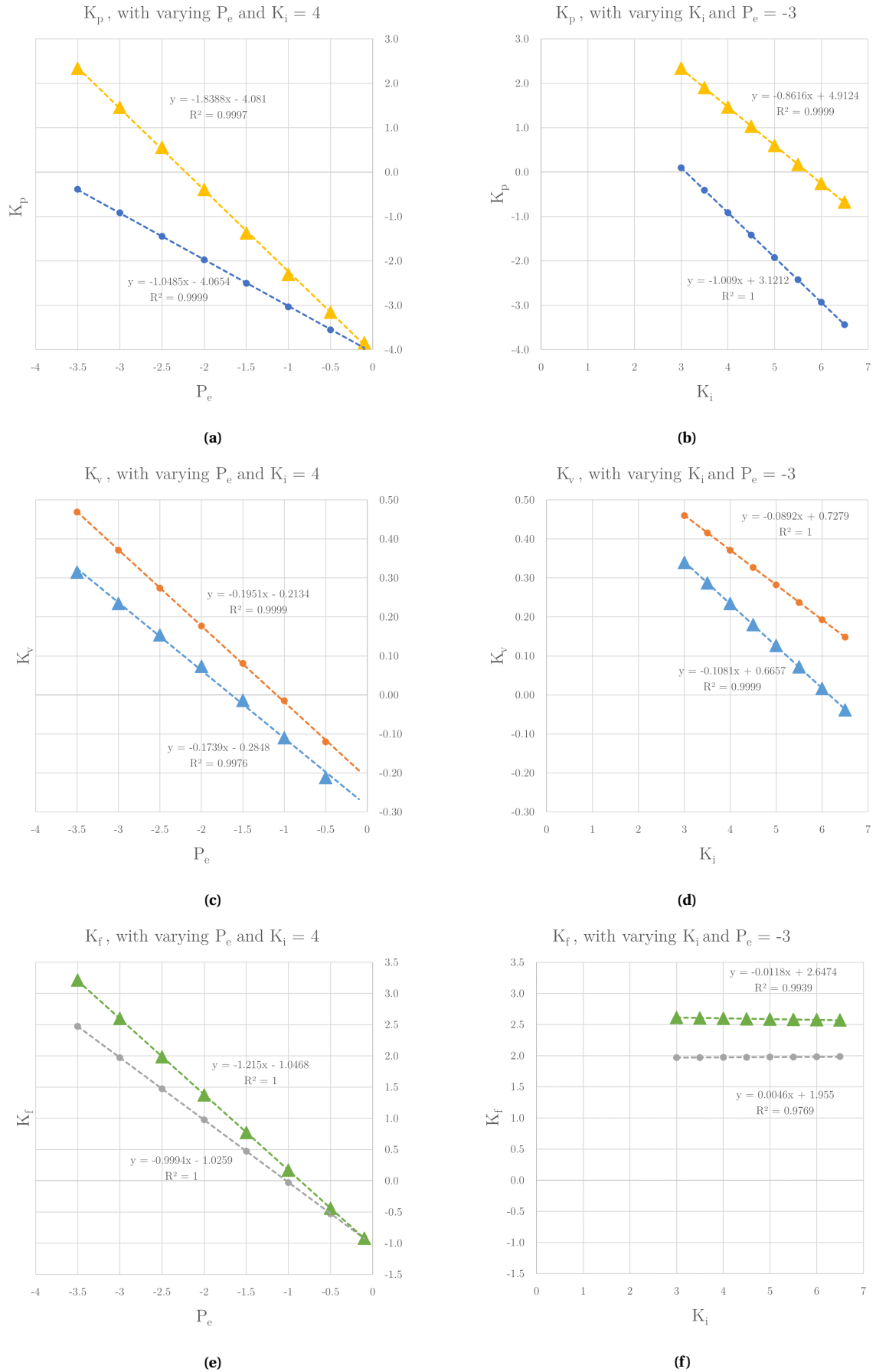


Figure 4.6: An overview of all the possible proprioceptor gains that realized a target tracking crossover frequency of $\omega_{c,t} \approx 1.7$ rad/s (circles) and $\omega_{c,t} \approx 2.5$ rad/s (triangles).

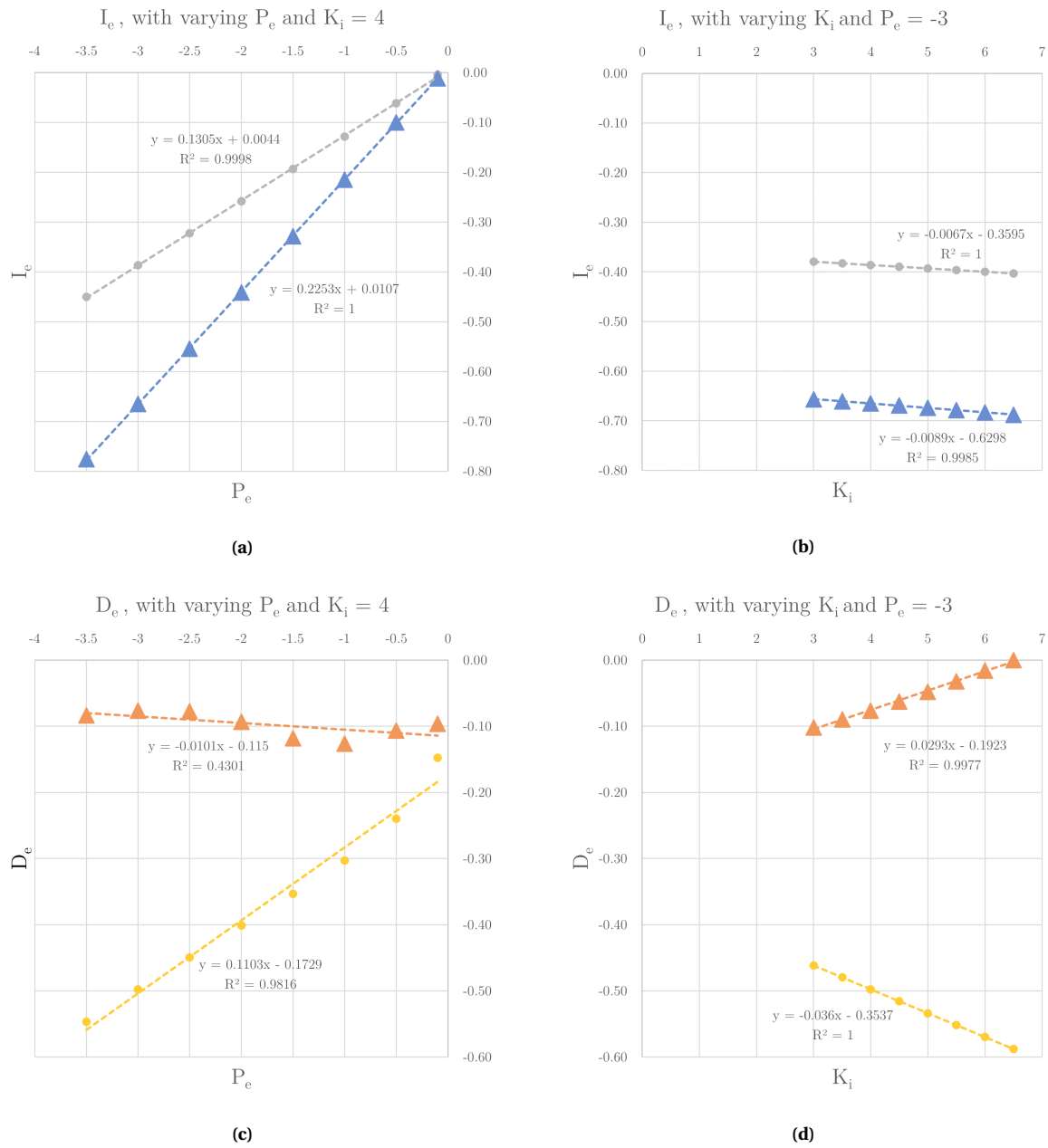


Figure 4.7: An overview of all the possible cognitive response gains that realized a target tracking crossover frequency of $\omega_{c,t} \approx 1.7$ rad/s (circles) and $\omega_{c,t} \approx 2.5$ rad/s (triangles).

Table 4.5: A summary of the relations shown in Figures 4.6 and 4.7, the approximations that were used and the 'average controller' setting that was derived from the approximation of the other two settings.

	HC setting	P_e	K_i	Linear regression	R^2	Approximation
K_p	Relaxed ($\omega_{c,t} \approx 1.7$ rad/s)	Free -3 Free	4 Free Free	$K_p = -1.8388P_e - 4.081$ $K_p = -0.8616K_i + 4.9124$	0.9997 0.9999	$K_p \approx -1.85P_e - 4$ $K_p \approx -0.86K_i + 5$ $K_p \approx -1.85P_e - 0.86K_i - 0.55$
	Tense ($\omega_{c,t} \approx 2.5$ rad/s)	Free -3 Free	4 Free Free	$K_p = -1.0485P_e - 4.0654$ $K_p = -1.009P_e + 3.1212$	0.9999 1	$K_p \approx -1.05P_e - 4$ $K_p \approx -1.01K_i + 3.1$ $K_p \approx -1.05P_e - 1.01K_i$
	Average ($\omega_{c,t} \approx 2.0$ rad/s)	Free	Free			$K_p \approx -1.45P_e - 0.94K_i - 0.28$
K_v	Relaxed ($\omega_{c,t} \approx 1.7$ rad/s)	Free -3 Free	4 Free Free	$K_v = -0.1739P_e - 0.2848$ $K_v = -0.1081K_i + 0.6657$	0.9976 0.9999	$K_v \approx -0.17P_e - 0.25$ $K_v \approx -0.11K_i + 0.67$ $K_v \approx -0.17P_e - 0.11K_i + 0.2$
	Tense ($\omega_{c,t} \approx 2.5$ rad/s)	Free -3 Free	4 Free Free	$K_v = -0.1951P_e - 0.2134$ $K_v = -0.0892K_i + 0.7279$	0.9999 1	$K_v \approx -0.2P_e - 0.25$ $K_v \approx -0.09K_i + 0.75$ $K_v \approx -0.2P_e - 0.09K_i + 0.15$
	Average ($\omega_{c,t} \approx 2.0$ rad/s)	Free	Free			$K_v \approx -0.185P_e - 0.1K_i + 0.175$
K_f	Relaxed ($\omega_{c,t} \approx 1.7$ rad/s)	Free -3 Free	4 Free Free	$K_f = -1.215P_e - 1.0468$ $K_f = -0.0118K_i + 2.6474$	1 0.9939	$K_f \approx -1.2P_e - 1$ $K_f \approx 2.6$ $K_f \approx -1.2P_e - 1$
	Tense ($\omega_{c,t} \approx 2.5$ rad/s)	Free -3 Free	4 Free Free	$K_f = -0.9994P_e - 1.0259$ $K_f = 0.0046K_i + 1.995$	1 0.9769	$K_f \approx -P_e - 1$ $K_f \approx 2$ $K_f \approx -P_e - 1$
	Average ($\omega_{c,t} \approx 2.0$ rad/s)	Free	Free			$K_f \approx -1.1P_e - 1$
I_e	Relaxed ($\omega_{c,t} \approx 1.7$ rad/s)	Free -3 Free	4 Free Free	$I_e = 0.2253P_e + 0.0107$ $I_e = -0.0089K_i - 0.6298$	1 0.9985	$I_e \approx 0.23P_e$ $I_e \approx -0.69$ $I_e \approx 0.23P_e$
	Tense ($\omega_{c,t} \approx 2.5$ rad/s)	Free -3 Free	4 Free Free	$I_e = 0.1305P_e + 0.0044$ $I_e = -0.0067K_i - 0.3595$	0.9998 1	$I_e \approx 0.13P_e$ $I_e \approx -0.39$ $I_e \approx 0.13P_e$
	Average ($\omega_{c,t} \approx 2.0$ rad/s)	Free	Free			$I_e \approx 0.18P_e$
D_e	Relaxed ($\omega_{c,t} \approx 1.7$ rad/s)	Free -3 Free	4 Free Free	$D_e = -0.0101P_e - 0.115$ $D_e = 0.0293K_i - 0.1923$	0.4301 0.9977	$D_e \approx -0.1$ $D_e \approx 0.029K_i - 0.2$ $D_e \approx 0.029K_i - 0.2$
	Tense ($\omega_{c,t} \approx 2.5$ rad/s)	Free -3 Free	4 Free Free	$D_e = 0.1103P_e - 0.1729$ $D_e = -0.036K_i - 0.3537$	0.9816 1	$D_e \approx 0.1P_e - 0.2$ $D_e \approx -0.036K_i - 0.35$ $D_e \approx 0.1P_e - 0.036K_i - 0.05$
	Average ($\omega_{c,t} \approx 2.0$ rad/s)	Free	Free			$D_e \approx 0.05P_e - 0.0035K_i - 0.125$

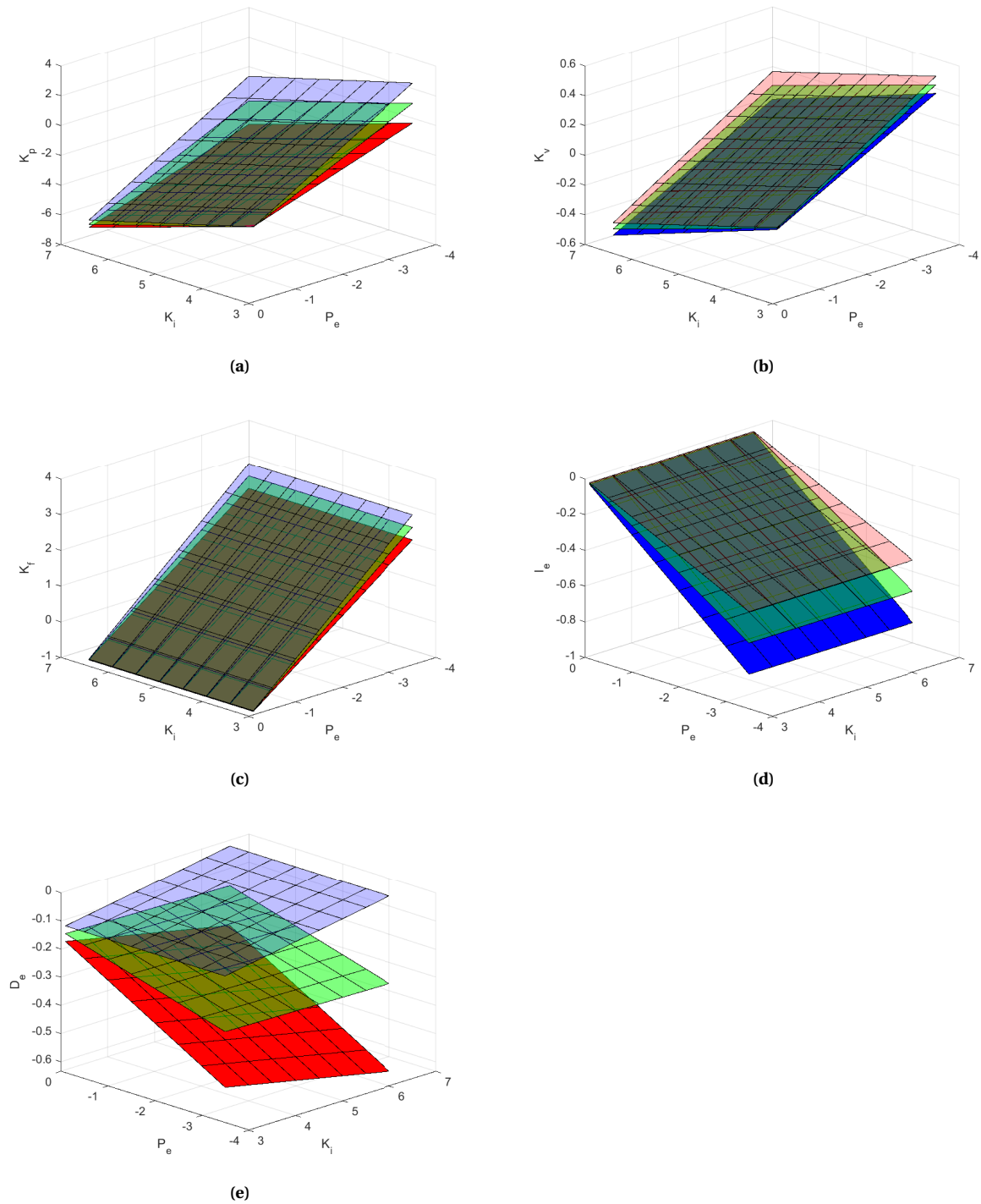
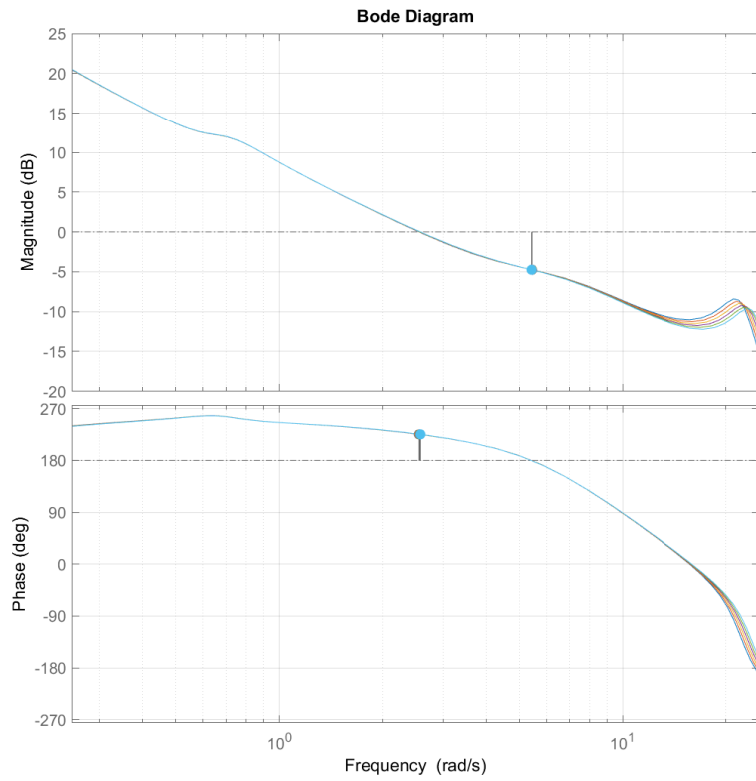
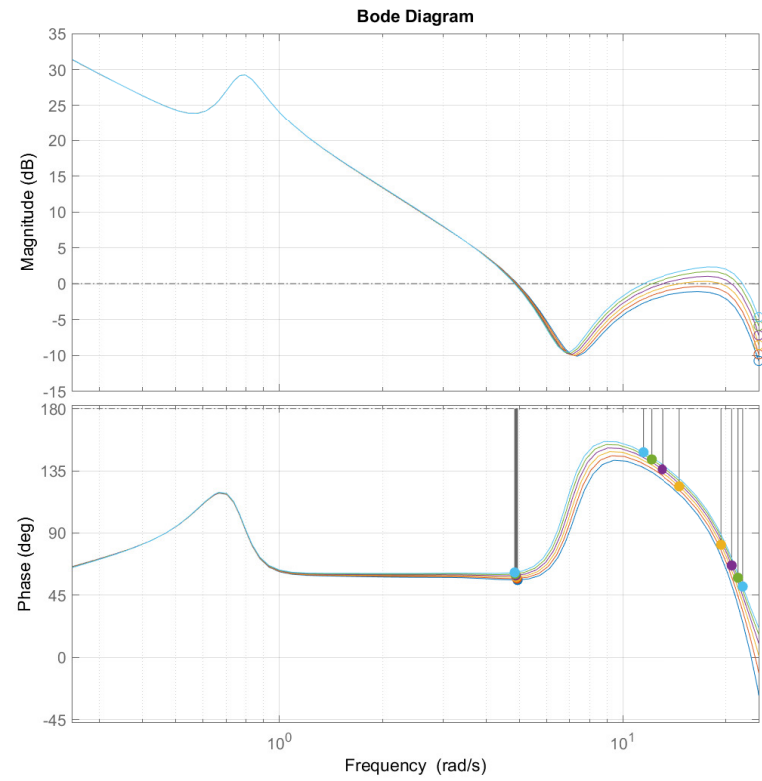


Figure 4.8: A graphical representation of all the bold functions from Table 4.5, where the blue, green and red planes correspond with the relaxed, average and tense controller, respectively. It should be noted that Figures 4.8d and 4.8e are rotated by 90 degrees with respect to the other plots, such that visibility of the planes is improved.



(a) The open-loop target tracking frequency responses.



(b) The open-loop disturbance rejection frequency responses.

Figure 4.9: Bode plots of all the dynamic systems that the data fitting algorithm converged to, when fitting the model on Fu's intermediate bandwidth data with $P_e = -3$ and $K_i = [3, 3.5, \dots, 6.5]$.

degrees of freedom P_e and K_i were combined to form two-dimensional functions for all HC parameters. Considering the participants in the experiment conducted by Fu [14] were able to achieve an $\omega_{c,t}$ ranging from approximately 1.8 to 2.5 rad/s, these functions were considered suitable candidates for the 'relaxed' and 'tense' controller settings. As the name suggests, the 'average' controller setting was determined, by taking the average of the tense and relaxed functions. While it was expected to result in a target tracking gain crossover frequency of 2.1 rad/s, an $\omega_{c,t}$ of 2.00 – 2.05 rad/s was achieved instead. Despite the minor difference in expected outcome, the result was still deemed suitable as an 'average' controller setting. Figure 4.8 provides a 3D representation of the functions indicated in bold in Table 4.5.

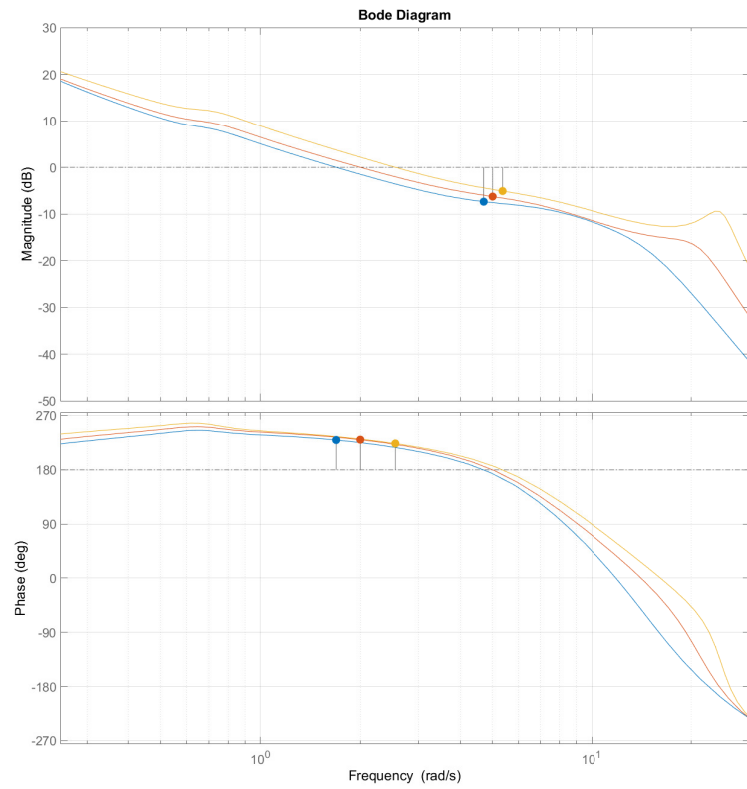
The final step in determining three reasonable HC settings involved the selection of the two variables that are considered the 'scheduling' variables: the proportional gain P_e that represents the intensity of the cognitive response and the intrinsic arm stiffness K_i , which is related to the amount of muscle co-contraction that the HC applies in his/her arm to reduce admittance. To determine these values, two assumptions were made:

1. An aggressive cognitive response (i.e., large $|P_e|$) is coupled with a high level of muscle co-contraction (i.e., large K_i).
2. The participants in the experiment conducted by Fu [14] exhibited a broad range of control behavior to realize their performance across the various scenarios. In other words, this means two things: 1) it is assumed that for the three HC settings, K_i varies across the range recorded by Lasschuit [47] and 2) P_e varies across the range that resulted in system stability **and** a representative time-domain performance in the simulations.

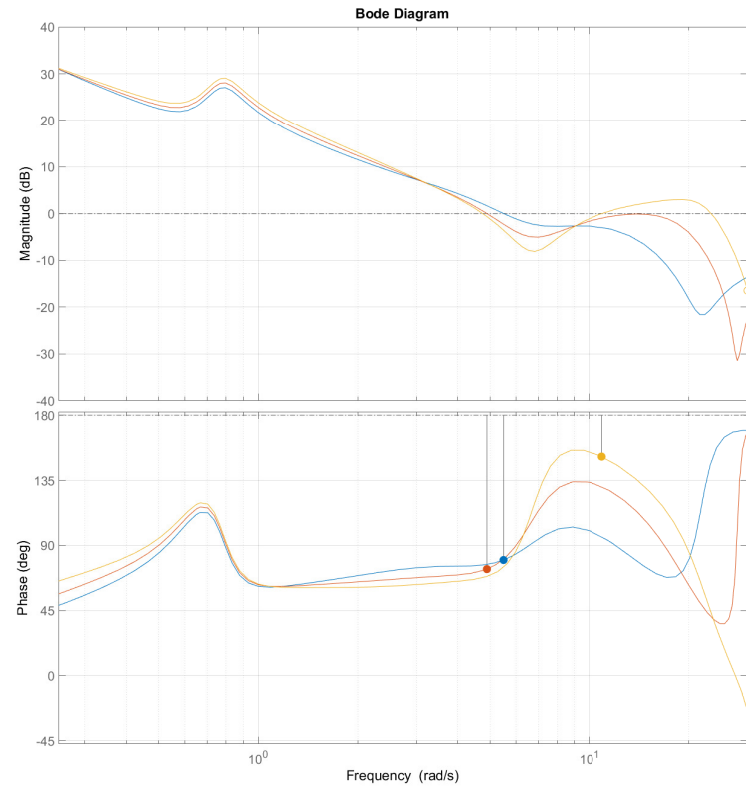
This resulted in the distinctive settings summarized in Table 4.6, of which the open-loop responses have been plotted in Figure 4.10.

Table 4.6: *The distinctive parameters for the relaxed, average and tense controller. The specific crossover characteristics belong to the scenario of the Boeing 747 roll dynamics, where $K_{fwd} = 2.5$ and $K_{\dot{\phi}} = -0.2857$.*

HC parameter	Relaxed	Average	Tense
P_e	-1	-2	-3
I_e	-0.23	-0.36	-0.39
D_e	-0.113	-0.241	-0.566
K_i	3	4.5	6
K_p	-1.28	-1.61	-2.91
K_v	0.04	0.095	0.21
K_f	0.2	1.2	2
$\omega_{c,t}$ [rad/s]	1.69	2.00	2.55
$\phi_{m,t}$ [°]	49.5	50.1	43.7
$\omega_{c,d}$ [rad/s]	5.50	4.90	1) 4.75, 2) 10.9
$\phi_{m,d}$ [°]	-100	-106	1) -112, 2) -28.6



(a) The open-loop target tracking frequency responses.



(b) The open-loop disturbance rejection frequency responses.

Figure 4.10: A Bode plot of the relaxed (blue), average (red) and tense (yellow) controller for the open-loop (a) target tracking and (b) disturbance rejection response for the Boeing 747, where $K_{fwd} = 2.5$ and $K_{\phi} = -0.2857$.

4.3. Quantification of aircraft dynamics and active stick settings

To determine whether there is any relation between the best active stick settings and the controlled element dynamics, the roll dynamics of three aircraft were tested in simulation:

1. The adjusted Boeing 747 dynamics that were also tested by Fu [14],
2. The Cessna 500 Citation roll dynamics, as identified by the faculty of Aerospace Engineering at TU Delft at 30000 ft altitude and a velocity of 398 ft/s ($V = 121.3$ m/s, $M = 0.4$) [49], and
3. The F-16 roll dynamics, which were linearized at the same flight condition using the 'low fidelity' model programmed by Russell [50], which is based on the work of Stevens and Lewis [51].

The adjusted Boeing 747 roll dynamics have already been introduced in Equation 2.4, but are repeated here for the sake of clarity:

$$\begin{aligned}
 H_{c,B747}(s) &= H_{ac,B747}(s) \cdot \frac{\Phi_{B747}(s)}{\Delta_{a,B747}(s)} \\
 &= \frac{1}{0.083s + 1} \cdot K_{c,B747} \cdot \frac{2.259s^2 + 0.821s + 1}{s(0.4s + 1)(1.647s^2 + 0.336s + 1)} \\
 &= \frac{1}{0.083s + 1} \cdot \frac{-12s^2 - 4.362s - 5.313}{s^4 + 2.704s^3 + 1.117s^2 + 1.518s} \\
 &= \frac{-7.906s^2 - 2.873s - 3.5}{0.05468s^5 + 0.8067s^4 + 1.842s^3 + 0.819s^2 + s}
 \end{aligned}$$

For the Cessna 500 Citation in the presented flight condition, it was determined that:

$$W = \frac{4b\mu_b(K_X^2 K_Z^2 - K_{XZ}^2)}{V} = \frac{4 \cdot 13.36 \cdot 32(0.013 \cdot 0.037 - 0.002^2)}{121.3} = 0.0067 \quad (4.10)$$

With this lemma, the state-space system representing the aircraft's asymmetric response for the presented flight condition was identified to be:

$$\begin{aligned}
 \begin{bmatrix} \dot{\beta} \\ \dot{\phi} \\ \frac{p b}{2V} \\ \frac{r b}{2V} \end{bmatrix} &= \begin{bmatrix} y_\beta & y_\phi & y_p & y_r \\ 0 & 0 & 2\frac{V}{b} & 0 \\ l_\beta & 0 & l_p & l_r \\ n_\beta & 0 & n_p & n_r \end{bmatrix} \begin{bmatrix} \beta \\ \phi \\ \frac{p b}{2V} \\ \frac{r b}{2V} \end{bmatrix} + \begin{bmatrix} 0 \\ 0 \\ l_{d_\alpha} \\ n_{d_\alpha} \end{bmatrix} \delta_\alpha \\
 &= \begin{bmatrix} \frac{(V/b)C_{Y\beta}}{2\mu_b} & \frac{(V/b)C_L}{2\mu_b} & \frac{(V/b)C_{Yp}}{2\mu_b} & \frac{(V/b)C_{Yr} - 4\mu_b}{2\mu_b} \\ 0 & 0 & 2V/b & 0 \\ \frac{C_{l_\beta} K_Z^2 + C_{n_\beta} K_{XZ}}{W} & 0 & \frac{C_{l_p} K_Z^2 + C_{n_p} K_{XZ}}{W} & \frac{C_{l_r} K_Z^2 + C_{n_r} K_{XZ}}{W} \\ \frac{C_{l_\beta} K_{XZ} + C_{n_\beta} K_X^2}{W} & 0 & \frac{C_{l_p} K_{XZ} + C_{n_p} K_X^2}{W} & \frac{C_{l_r} K_{XZ} + C_{n_r} K_X^2}{W} \end{bmatrix} \begin{bmatrix} \beta \\ \phi \\ \frac{p b}{2V} \\ \frac{r b}{2V} \end{bmatrix} + \begin{bmatrix} 0 \\ 0 \\ \frac{C_{l_{\delta_\alpha}} K_Z^2 + C_{n_{\delta_\alpha}} K_{XZ}}{W} \\ \frac{C_{l_{\delta_\alpha}} K_{XZ} + C_{n_{\delta_\alpha}} K_X^2}{W} \end{bmatrix} \delta_\alpha \\
 &= \begin{bmatrix} -0.1880 & 0.09270 & -0.01870 & -18.10 \\ 0 & 0 & 18.16 & 0 \\ -0.5341 & 0 & -2.026 & 0.9055 \\ 0.3229 & 0 & -0.1028 & -0.3211 \end{bmatrix} \begin{bmatrix} \beta \\ \phi \\ \frac{p b}{2V} \\ \frac{r b}{2V} \end{bmatrix} + \begin{bmatrix} 0 \\ 0 \\ -1.299 \\ -0.3119 \end{bmatrix} \delta_\alpha
 \end{aligned} \quad (4.11)$$

Assuming the Cessna's actuator dynamics to be the same as the Boeing 747, this resulted in the following roll dynamics:

$$\begin{aligned}
H_{c,CC}(s) &= H_{ac,CC}(s) \cdot \frac{\Phi_{CC}(s)}{\Delta_{a,CC}(s)} \\
&= \frac{1}{0.083s+1} \cdot K_{c,CC} \cdot \frac{0.1211s^2 + 0.08795s + 1}{(68.49s-1) \cdot (0.1580s^2 + 0.05309s + 1) \cdot (0.4525s + 1)} \\
&= \frac{1}{0.083s+1} \cdot \frac{-23.58s^2 - 17.13s - 194.9}{s^4 + 2.535s^3 + 7.019s^2 + 13.87s - 0.2035} \\
&= \frac{-23.58s^2 - 17.13s - 194.9}{0.083s^5 + 1.21s^4 + 3.118s^3 + 8.17s^2 + 13.86s - 0.2035}
\end{aligned} \tag{4.12}$$

For the F-16, the program made by Russell [50] was used to linearize the F-16's dynamics around the same flight condition as the Cessna Citation, which was verified to be inside the F-16's flight envelope. Reducing the produced 18-state system for the rolling motion that is being tested in this thesis gives the following:

$$\begin{bmatrix} \dot{\beta} \\ \dot{\phi} \\ \frac{\dot{pb}}{2V} \\ \frac{\dot{rb}}{2V} \end{bmatrix} = \begin{bmatrix} -0.09576 & 0.07853 & 0.2376 & -0.9685 \\ 0 & 0 & 1 & 0.2438 \\ -13.75 & 0 & -0.9537 & 0.5489 \\ 2.111 & 0 & -0.02454 & -0.1622 \end{bmatrix} \begin{bmatrix} \beta \\ \phi \\ \frac{pb}{2V} \\ \frac{rb}{2V} \end{bmatrix} + \begin{bmatrix} 8.162 \cdot 10^{-5} \\ 0 \\ -0.1705 \\ -0.009847 \end{bmatrix} \delta_\alpha \tag{4.13}$$

With the F-16's actuator dynamics that were found to be $H_{act,F16}(s) = \frac{1}{0.0495s+1}$ and a conversion from radians to degrees, this resulted in:

$$\begin{aligned}
H_{c,F16}(s) &= H_{ac,F16}(s) \cdot \frac{\Phi_{F16}(s)}{\Delta_{a,F16}(s)} \\
&= \frac{1}{0.0495s+1} \cdot K_{c,F16} \cdot \frac{0.3394s^2 + 0.1018s + 1}{(90.09s+1)(1.481s+1)(0.1915s^2 + 0.1007s + 1)} \cdot \frac{180}{\pi} \\
&= \frac{1}{0.0495s+1} \cdot \frac{-31.12s^2 - 9.354s - 92.11}{3.142s^4 + 3.807s^3 + 17.55s^2 + 11.27s + 0.123} \\
&= \frac{-31.12s^2 - 9.354s - 92.11}{0.1555s^5 + 3.33s^4 + 4.675s^3 + 18.11s^2 + 11.27s + 0.123}
\end{aligned} \tag{4.14}$$

Figure 4.11 and Table 4.7 show how these CE dynamics compare. What made these CE dynamics particularly interesting to compare are their different crossover frequencies and phase margins, while the Bode plots of the B747 and F-16 are strikingly similar in the human crossover region that is known for this compensatory roll task (5-8 rad/s) [1].

Table 4.7: The crossover characteristics of the controlled element dynamics shown in Figure 4.11.

Aircraft	Gain crossover frequency ω_c [rad/s]	Phase margin ϕ_m [°]
Boeing 747	3.03	22.3
F16	3.51	9.35
Cessna Citation	4.10	-2.36

These aircraft dynamics were simulated with a variety of active stick settings, which are characterized by the feedforward gain K_{fwd} and the roll rate feedback gain K_ϕ . The setting ranges were extended up to the point where the system became unstable for nearly all aircraft dynamics and HC settings, which resulted in a setting range of $K_{fwd} = [0.5, 1, \dots, 10.5]$ and $K_\phi = [-0.075, -0.150, \dots, -0.600]$.

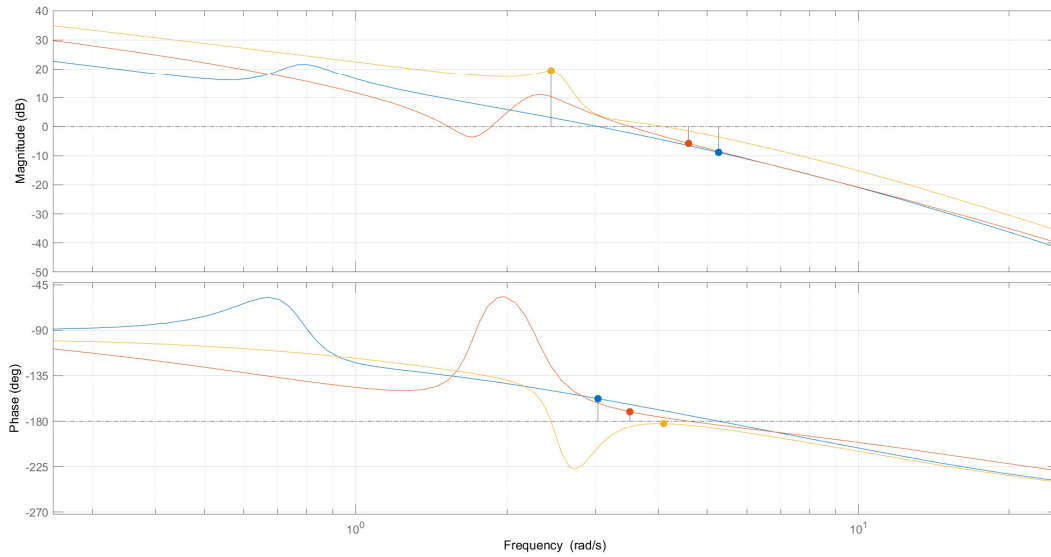


Figure 4.11: *The controlled element dynamics that are simulated in this thesis: the Boeing 747 (blue), the F-16 (red) and the Cessna 500 Citation (yellow).*

4.4. Simulation output and observations

The factorial combination of the three HC settings, three aircraft and 186 active stick settings presented in Sections 4.2.3 and 4.3 amounted to a total of 1674 model conditions that were simulated with the model. These conditions were all simulated with identical forcing functions that were based on the intermediate signal bandwidth tested by Fu [14]. The exact amplitudes and phase angles of the forcing functions are shown in Tables 4.8 and 4.9.

Due to the stochastic nature of the cognitive noise term that is present in the model (see Section 3.2 for more information), the output of the simulation is stochastic as well. To ensure a representative simulation output, the SNR of 0.10 at the error signal e (as suggested by Van der El [43]) played a decisive role. The output of a simulation run at any given condition was only accepted whenever the aforementioned SNR fell between 0.0995 and 0.1005. Whenever a run was rejected, the cognitive noise intensity W_n was adjusted by few %, depending on the magnitude of the deviation. For every model condition, the output of 30 accepted runs was averaged to determine the values presented in Figures 4.14, 4.15 and 4.16.

When looking at the tables, some model conditions have been blocked out with three different shades of gray. This is done for the following reasons:

- **Dark gray:** system instability. Whenever MATLAB detected an unstable system, the model condition was skipped. For all aircraft, this occurred for feedback gains that were too gentle ($|K_{\dot{\phi}}| < 0.075$) and this limit moved up towards $|K_{\dot{\phi}}| \approx 0.15$ as the HC became more aggressive. For the slower F-16 and B747, a low feed-forward gain does seem to reduce the minimum $|K_{\dot{\phi}}|$ required for stability, although the model conditions at this edge of the stable region do result in relatively poor performance.

Besides that, there is an apparent limit for K_{fwd} , past which system instability occurs. This limit seems to depend on two factors. For all aircraft, it is clear that a more ambitious HC setting reduces the value for K_{fwd} at which the system becomes unstable. Besides that, the limit for K_{fwd} also seems to depend on the CE dynamics. Whereas the F-16 only seems to be slightly more restrictive in this regard compared to the Boeing 747, it is evident that the more nervous dynamics of the Cessna Citation prove to be much more restrictive.

- Light gray: systems that appeared stable in terms of target tracking, but were realized with control signals that were of extremely high frequency and intensity (see Figures 4.13a and 4.13b for clarification). Some of these model conditions produced an $RMS(e)$ that seemed representative, however their $RMS(m_{grip})$ of $10^2 - 10^3$ Nm was a clear indication that these results were not physically possible, given the standard $RMS(m_{grip})$ range for this task of $0 - 0.3$ Nm. It is interesting to see that the CE dynamics seem to play a decisive role in the active stick settings where such behavior occurs, whereas the HC's control behavior seems to have no impact on this at all. What these conditions will produce in practice, however, remains uncertain for now.
- Gray: model conditions at the edge of system stability that produced unrealistically strong performance. On some rare occasions, model conditions that bordered the areas deemed unstable due to their gentle feedback gains produced $RMS(e)$'s and $RMS(m_{grip})$'s that were both 3-10 times stronger than the most potent active stick settings of that aircraft / HC setting matrix. While the plausibility of such performance is questionable in itself, tuning one's system to such a precarious setting seems unwise or downright irresponsible regardless.

Besides the observations with regards to system stability, the following points can be made with regards to the simulated HC performance:

1. As Figures 4.14, 4.15 and 4.16 suggest, the value for $K_{\dot{\phi}}$ that produces the best results in terms of tracking performance and control effort seems to be virtually independent of the pilot setting and CE dynamics, hovering at a value of ≈ -0.225 .
2. For K_{fwd} , an optimal value seems to become more pronounced for all aircraft as the pilot becomes more aggressive. These values are very similar for the Boeing 747 and F-16 (≈ 3.5 and ≈ 4 , respectively), whereas the optimal value for the Cessna Citation is approximately half of that (≈ 2).
3. As was stated by Fu [14], the introduction of the haptic roll rate feedback made the system feel sluggish, an undesirable feature for which the feed-forward gain could compensate. The simulation output supports this finding, as model conditions where $K_{fwd} \leq 1$ consistently result in poor performance, both in terms of target tracking and required control effort. For the more nervous Cessna Citation dynamics, a sluggish feed-forward gain of $K_{fwd} = 0.5$ even resulted in system instability for the model conditions where $|K_{\dot{\phi}}| \leq 0.3$.
4. The increasing minimum required value for $|K_{\dot{\phi}}|$ for increasing pilot aggressiveness, combined with observation 1, implies a human performance plateau for the active stick configuration.
5. Figure 4.12 and Table 4.10 show the best recorded settings for all HC setting / aircraft matrices. What can be noted from Figures 4.14, 4.15 and 4.16 is that these settings are mostly achieved near the edge of the oscillatory region, except for the cases where the pilot acts as an aggressive controller. In those situations, the minimal value for m_{grip} served as the basis on which the 'best recorded' setting was determined.
6. For any given feedback gain, pilot performance seems to increase for an increasing K_{fwd} (except for the situations with aggressive pilot settings), however the added returns diminish as the oscillatory zone is approached. Whereas the practical consequences of entering this zone are unknown at this point, it is safest to assume for now that these conditions will result in system instability. Approaching this zone would thereby decrease stability margins. Selecting an 'optimal' K_{fwd} based on the model condition that resulted in the lowest $RMS(m_{grip})$ for an aggressive pilot setting resulted in a safety factor on K_{fwd} of at least 1.5 for all aircraft before the oscillatory zone was reached, which was deemed acceptable.
7. As Figure 4.12 and the colors from Figures 4.14, 4.15 and 4.16 suggest, the pilot seems to reap most (if not all) performance benefits from the active stick configuration as a relaxed con-

troller already. Whereas there seems to be some tracking performance to be gained from being a more aggressive pilot for the relatively slow Boeing 747, the pilot seems to be simply better off by being less aggressive when controlling the more nervous Cessna Citation.

Table 4.8: The target forcing function that is used in the simulations.

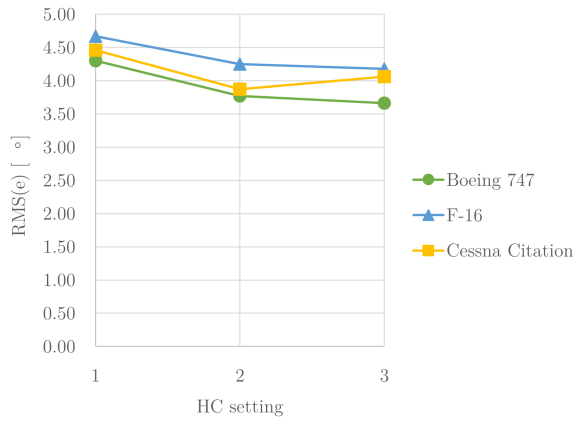
f_t				
k	Period	ω_t [rad/s]	A_t [rad]	θ_t [rad/s]
1	5	0.3835	0.1984	2.3319
2	11	0.8437	0.1645	5.5352
3	21	1.6107	0.0724	0.6807
4	37	2.8379	0.0248	5.8910
5	51	3.9117	0.0134	3.2216
6	71	5.4456	0.0074	0.9325
7	101	7.7406	0.0045	5.6708
8	137	10.5078	0.0036	1.1480
9	191	14.6495	0.0032	4.4054
10	224	17.1806	0.0032	4.0862

Table 4.9: The disturbance forcing function that is used in the simulations.

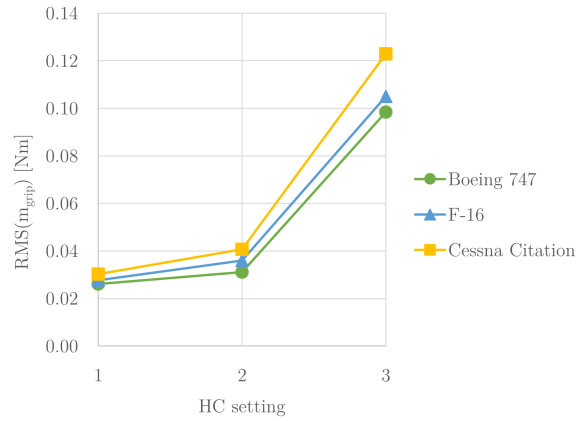
f_d				
k	Period	ω_d [rad/s]	A_d [rad]	θ_d [rad/s]
1	6	0.4602	0.0273	5.1081
2	13	0.9971	0.0213	4.1567
3	23	1.7641	0.0258	3.8964
4	38	2.9146	0.0220	1.1398
5	53	4.0650	0.0209	3.2806
6	73	5.5990	0.0221	3.5648
7	103	7.9000	0.0289	1.8805
8	139	10.6612	0.0462	1.6206
9	194	14.8796	0.0964	2.2507
10	227	17.4107	0.1430	4.3722

Table 4.10: The best recorded settings for all aircraft, for all three pilot settings.

Aircraft	1. Relaxed controller		2. Average controller		3. Tense controller	
	$RMS(e)$ [°]	$RMS(m_{grip})$ [Nm]	$RMS(e)$ [°]	$RMS(m_{grip})$ [Nm]	$RMS(e)$ [°]	$RMS(m_{grip})$ [Nm]
B747	4.30	0.0261	3.77	0.0311	3.66	0.0985
F-16	4.67	0.0277	4.25	0.0360	4.18	0.105
CC	4.46	0.0303	3.87	0.0407	4.06	0.123

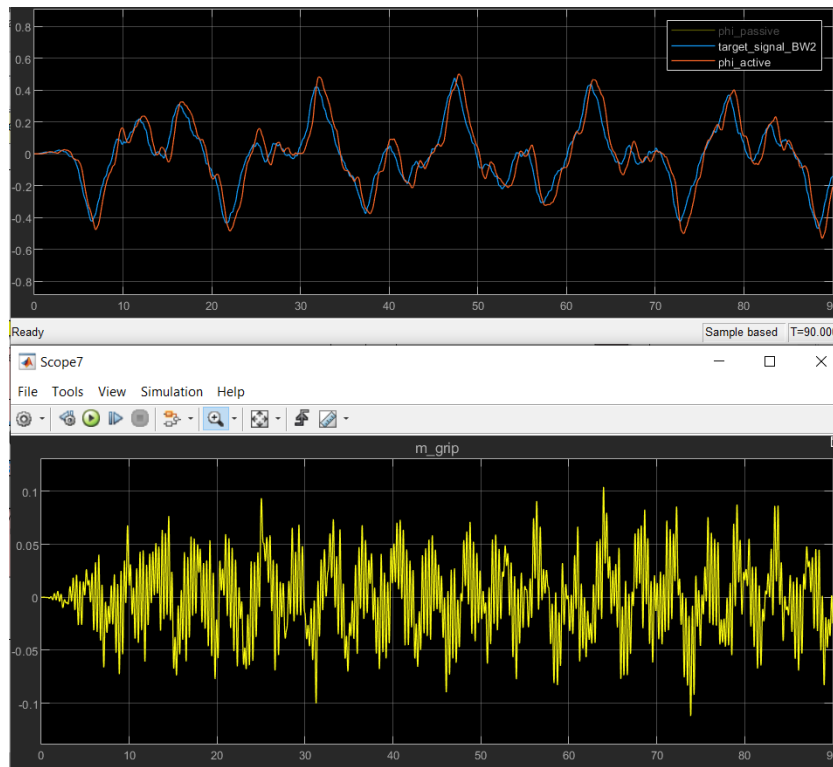


(a)

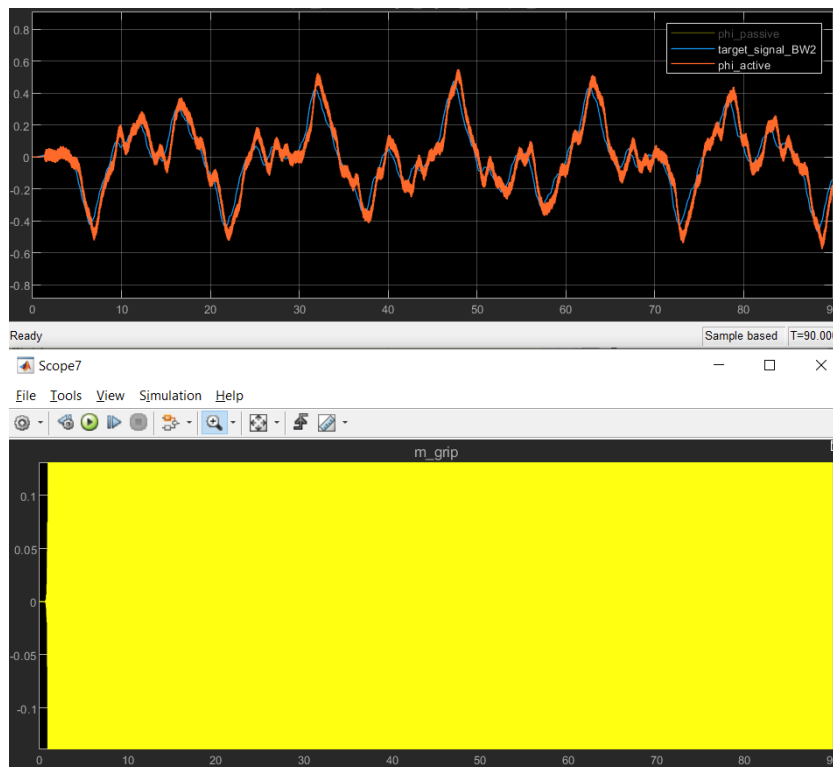


(b)

Figure 4.12: The (a) $RMS(e)$ and (b) $RMS(m_{grip})$ values from Table 4.10 plotted in a graph, to emphasize the highly similar performance that can be achieved for the Boeing 747, the F-16 and the Cessna Citation.



(a)



(b)

Figure 4.13: A clarification of what (a) a regular, stable model condition and (b) a light gray, oscillatory model condition produced as simulation output. Here, the blue and red graph represent the target forcing function f_t and aircraft roll angle ϕ , respectively, and the yellow graph shows the m_{grip} that realized this response.

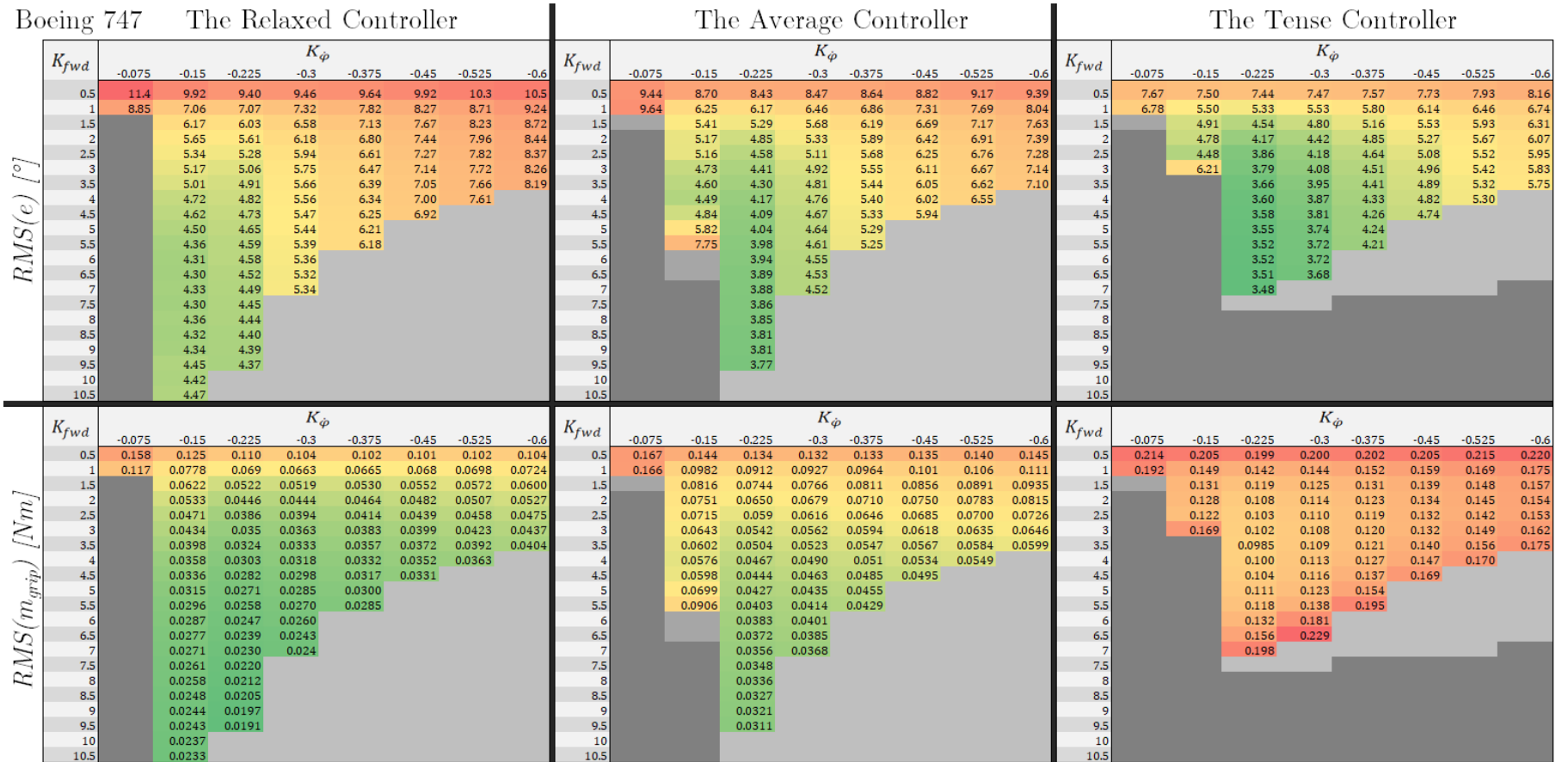


Figure 4.14: Simulation output for the Boeing 747.

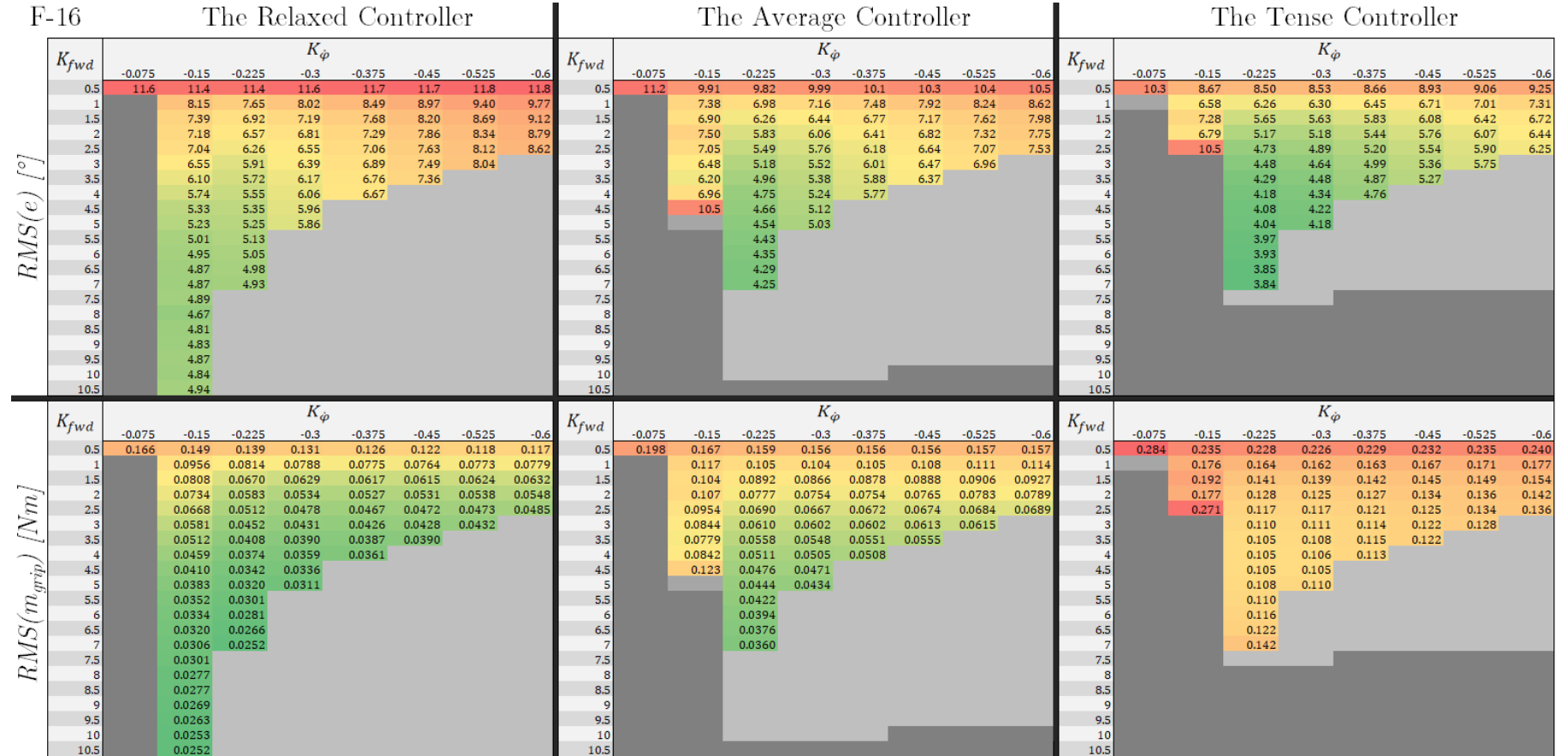


Figure 4.15: Simulation output for the F-16.

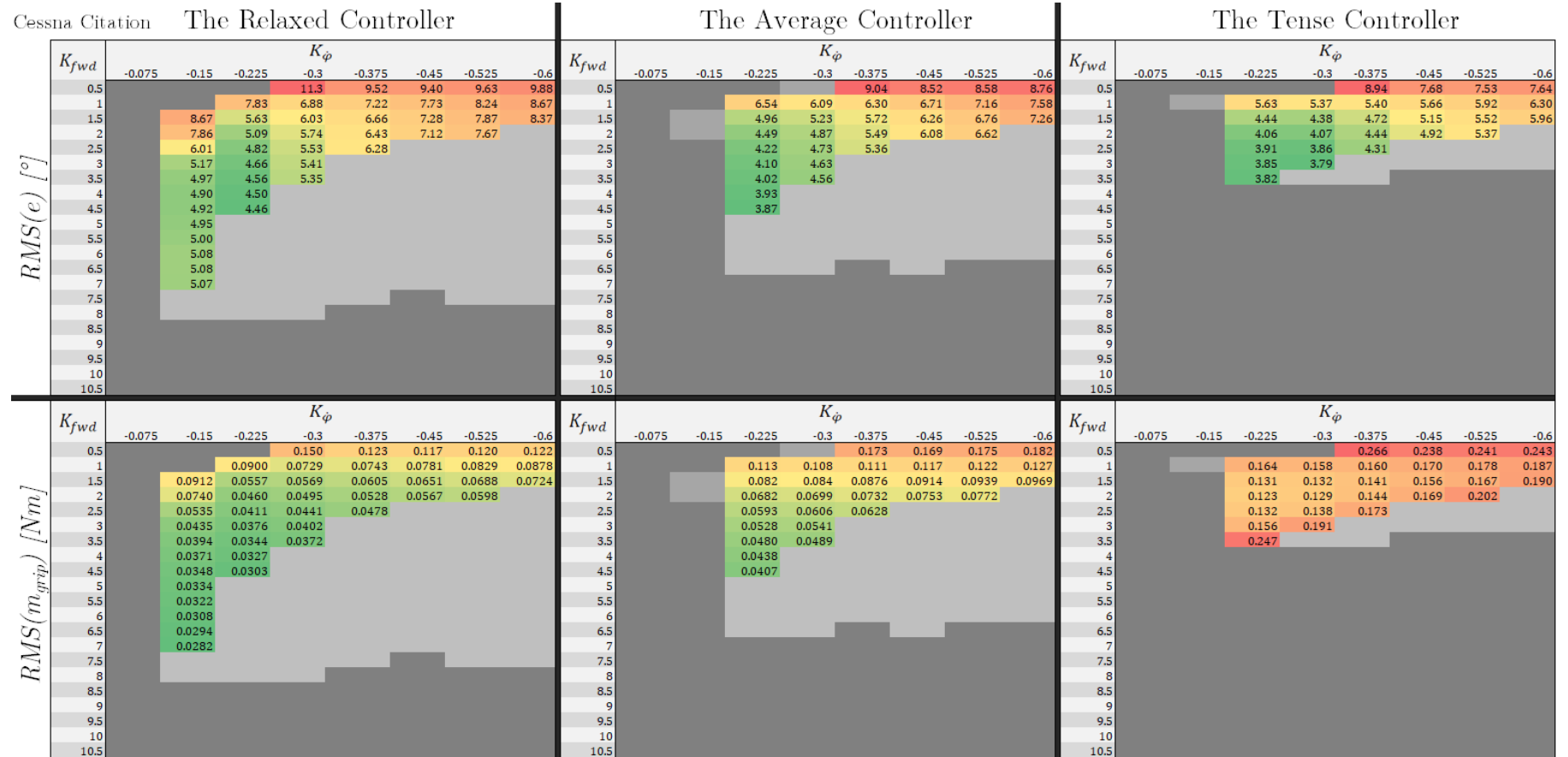


Figure 4.16: Simulation output for the Cessna 500 Citation.

4.5. Reflection on existing manual control theory

When reflecting upon the observations from Section 4.4 (in particular the ones that hint at some optimal value for $K_{\dot{\phi}}$ and K_{fwd}), a combination of the existing findings from Fu [14] and the fundamental manual control theory postulated by McRuer [1] could provide an explanation why certain trends in the simulation output occur. One of the most interesting questions to ask is: *why does $(K_{\dot{\phi}})_{opt}$ remain nearly unchanged for different CE dynamics and pilot settings?*

To answer this question, we can consider two points. The first point is related to the adaptive nature as well as the preferences of the HC, which have been recorded through the extensive set of experimental conditions tested by McRuer for a compensatory tracking task [1]. What makes McRuer's findings particularly valuable for this thesis is that they involve a **control setting** identical to the one tested in this thesis, which is defined by the pure lateral motion of a side stick (as supported by the comparison of Figure 4.17 with Figures 2.4 and 2.6a). As is stated by McRuer, HCs perform best when the CE dynamics for a compensatory tracking task resemble single integrator dynamics in the human crossover region. Besides that, McRuer has shown that for CE dynamics of a given form, such as $H_c(s) = \frac{K_c}{s}$, HCs compensate through their own behavior (Y_p) for any variation in K_c , effectively converging to the same preferred open-loop dynamics $|Y_p H_c|$. There seemed to be only a slight variation in the preferred $|Y_p H_c|$ based on the forcing function bandwidth, which is shown in Figure 4.18a. With the HC effectively producing single integrator open-loop dynamics in the human crossover region, the transfer function approximating these dynamics ($\frac{\omega_c}{s}$, see Figure 4.18a) can be defined based on the ω_c values highlighted in Figure 4.18b, for which McRuer reported an average value of $\omega_c = 4.75$ rad/s [1].

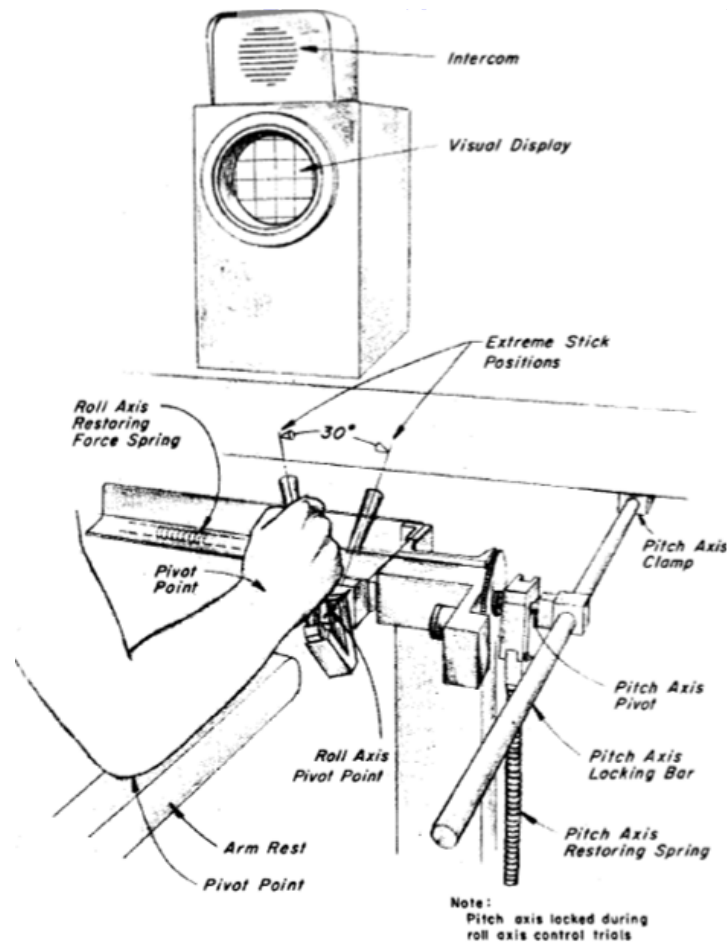
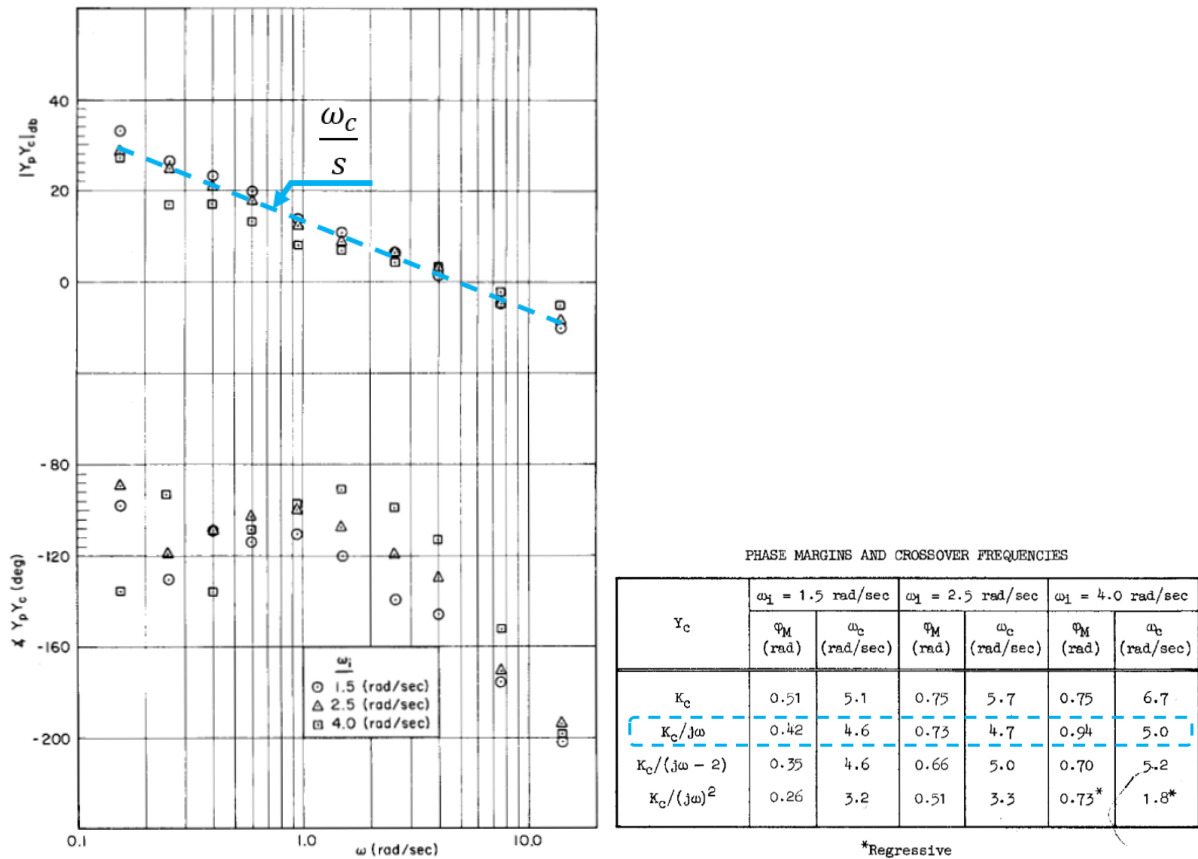


Figure 4.17: The control setting used by McRuer [1].



(a) Bode plots of the averaged open-loop describing functions, where the CE dynamics $Y_c(s)$ are equal to $\frac{K_c}{s}$, for forcing functions having different signal bandwidths ω_i (Figure 48 from [1]). The resulting $|Y_p Y_c|$ can be approximated by $\frac{\omega_c}{s}$.

(b) A table showing the crossover characteristics for the various CE dynamics (Y_c) that were tested (Table 8 from [1]). The highlighted row belongs to the single integrator CE dynamics Bode plots that are shown in Figure 4.18a.

Figure 4.18

The second point is related to the working principle behind the active stick, which is illustrated in Figure 2.7. As is stated by Fu [14], the nature of the active stick’s haptic feedback has a decisive impact on the CE dynamics that the HC *effectively* experiences when holding the stick, in that the effective CE dynamics are defined as the inverse of the haptic feedback transfer function. In essence, this provides a great amount of design freedom for control configurations involving the active stick.

Combining the active stick’s ability to shape the effectively experienced CE dynamics and McRuer’s findings regarding the HC’s preference for single integrator CE dynamics in the human crossover region, this suggests that haptic feedback involving a single differentiator (i.e., **rate** feedback) is desirable. In Figure 2.7, ‘ $K_m s$ ’ represents the rate feedback that is employed in this thesis as $K_{\dot{\phi}}$, which results in **single** integrator dynamics effectively being experienced by the HC (i.e. $H_{c,eff} = \frac{1}{K_{\dot{\phi}} s}$).

On top of this, one could argue that the open-loop dynamics that the HC prefers to converge to for a given control setting ($\frac{\omega_c}{s}$) would imply that the optimal haptic rate feedback gain for said setting is the inverse of ω_c , which in our case means that:

$$|(K_{\dot{\phi}})_{opt}| = \frac{1}{\omega_c} \approx \frac{1}{4.75} = 0.2105 \tag{4.15}$$

Due to the sign convention related to aircraft roll dynamics, it would mean for this thesis that $(K_{\dot{\phi}})_{opt}$ would equal -0.2105. The simulation output shown in Figures 4.14, 4.15 and 4.16 does seem to support this suggestion, as the closest simulated feedback of $K_{\dot{\phi}} = -0.225$ provides the most promising results across the board. The different values reported for ω_c in Figure 4.18b for various forcing

function bandwidths (which can be related to the general difficulty of the mission) would suggest a slight variation in $(K_{\dot{\phi}})_{opt}$. This ranges from about $(K_{\dot{\phi}})_{opt} = 0.20$ for high bandwidth (difficult) forcing functions to $(K_{\dot{\phi}})_{opt} = 0.22$ for low bandwidth (easy) forcing functions, however the difference between these values seems to be small enough to neglect this dependency. Therefore, for the practical design of a control system involving an active stick configuration, it is proposed that:

Hypothesis 1: *The optimal haptic rate feedback gain is primarily a function of the control setting, and should thereby be constant for a given control setting.*

Whereas the simulations clearly point towards a certain feedback setting as the most suitable, the same cannot be said for the feed-forward gain K_{fwd} . As is stated in observation 6 from Section 4.4, the simulation output suggests on various occasions that the most promising model conditions are located at the edge of the oscillatory zone. This seems like an unnecessarily risky choice, considering the practical consequences of entering this zone are unknown at this point, combined with the reduced added returns that are obtained when approaching this zone. Selecting $(K_{fwd})_{opt}$ based on the minimal $RMS(m_{grip})$ required from an aggressive pilot therefore seems like the most sensible option at this point, considering a pronounced optimum does seem to form in $RMS(m_{grip})$ for all aircraft as the pilot becomes more aggressive.

To determine why the simulations suggest a $(K_{fwd})_{opt}$ of about 3.5, 4 and 2 for the Boeing 747, the F-16 and the Cessna Citation, respectively, a possible explanation could once again be found in the findings from McRuer [1]. McRuer determined that the character of the CE dynamics inside the human crossover region play a decisive role when designing for and assessing human performance in manual control tasks. This human crossover region is related to the maximum speed at which HCs are able to consciously exert control commands on the manipulator, which means that this frequency band may depend on the body parts involved in the control task as well as the trajectory along which said body parts have to move (hence, the control setting). McRuer [1] found out that the human crossover region for the compensatory roll task involving a side stick (identical to the setting used in this thesis) stretched from approximately 5 to 8 rad/s.

Even though Equations 2.4, 4.12 and 4.14 show that the combined actuator / aircraft roll dynamics form third-order systems, the three aircraft all resemble second-order systems in the human crossover region for this task, which means that HCs will likely have the impression that they are controlling a second-order system. Figure 4.20 shows the Bode plots of the three aircraft once again, but now combined with the second-order transfer functions $(H_c(s) = \frac{K_d}{s^2})$ that approximate the aircraft dynamics in this region, where K_d for all aircraft was calculated by dividing the highest-order numerator term from Equations 2.4, 4.14 and 4.12 by the second-highest-order denominator term. As $K_{d,B747} = 9.800$, $K_{d,F16} = 9.345$ and $K_{d,CC} = 19.49$, the relation $K_d \cdot (K_{fwd})_{opt} = C_{fwd}$ could be a possible explanation as to why $(K_{fwd})_{opt,CC}$ is about half the value of the other two, with $(K_{fwd})_{opt,B747}$ being only slightly smaller than $(K_{fwd})_{opt,F16}$.

Whereas the rationale behind the value for C_{fwd} is still unknown, the simulation output suggests that for CE dynamics resembling 1) *second-order systems* inside the crossover region related to 2) *this specific control setting*, a value of $C \approx 37$ would be called for. To formalize this suggestion for the active stick's tuning procedure in a way that stays within the scope of what will be experimented with in this thesis, it is proposed that:

Hypothesis 2: *The optimal haptic feed-forward gain is inversely proportional to the gain K_d that is used in the basic transfer function $\left(H_c(s) = \frac{K_d}{s^2}\right)$ that approximates the controlled element dynamics in the human crossover region for the compensatory roll task involving a side stick.*

While the findings regarding $(K_{fwd})_{opt}$ leave something to be desired, there is a silver lining to be found when considering the work carried out by Fu [14]. After selecting a certain feedback gain ($|K_{\dot{\phi}}| = 0.2857$), Fu selected K_{fwd} based on manual trial and error in the simulator, which resulted in the selection of $K_{fwd} = 2.5$. Figure 4.19 supports that the modeled 'aggressive' pilot is best able to replicate the HC's performance from the experiment for the forcing function signal bandwidth that is used in this thesis. Looking at the rightmost matrices in Figure 4.14, one can notice how closely Fu was able to approach the simulated optimum for $RMS(m_{grip})$ given that feedback gain, with the closest simulated feedback gain ($K_{\dot{\phi}} = -0.3$) resulting in $RMS(m_{grip}) = 0.110$ Nm, while $(RMS(m_{grip}))_{opt} = 0.108$ Nm for $K_{\dot{\phi}} = -0.3$.

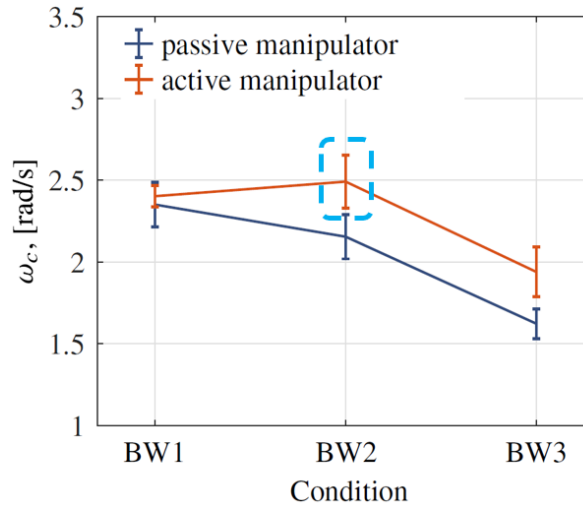


Figure 4.19: The average target tracking crossover frequencies achieved by participants in the experiment conducted by Fu [14]. The highlighted data point is most relevant, as the intermediate bandwidth forcing functions (see Tables 2.2 and 2.3) are used in this thesis as well.

4.6. Proposal of active stick tuning procedure

Based on the findings stated in Section 4.5, the following tuning procedure is proposed for control systems involving an active stick configuration:

1. For a given control setting, determine $(K_{\dot{\phi}})_{opt}$ first:
 - Perform a single integrator CE dynamics $\left(H_c(s) = \frac{K_c}{s}\right)$ compensatory tracking task with a passive stick, similar to the experiment conducted by McRuer [1] in the 1960s.
 - Determine the average gain crossover frequency ω_c to which HCs prefer to converge for various values of K_c .
 - Calculate $(K_{\dot{\phi}})_{opt} = \frac{1}{\omega_c}$.
2. Then, for a given control setting with some CE dynamics:
 - Determine $(K_{fwd})_{opt}$ through manual trial and error in the simulator.
 - From this, $(K_{fwd})_{opt}$ can be inferred for other CE dynamics that are of comparable character in the human crossover region of said control setting.

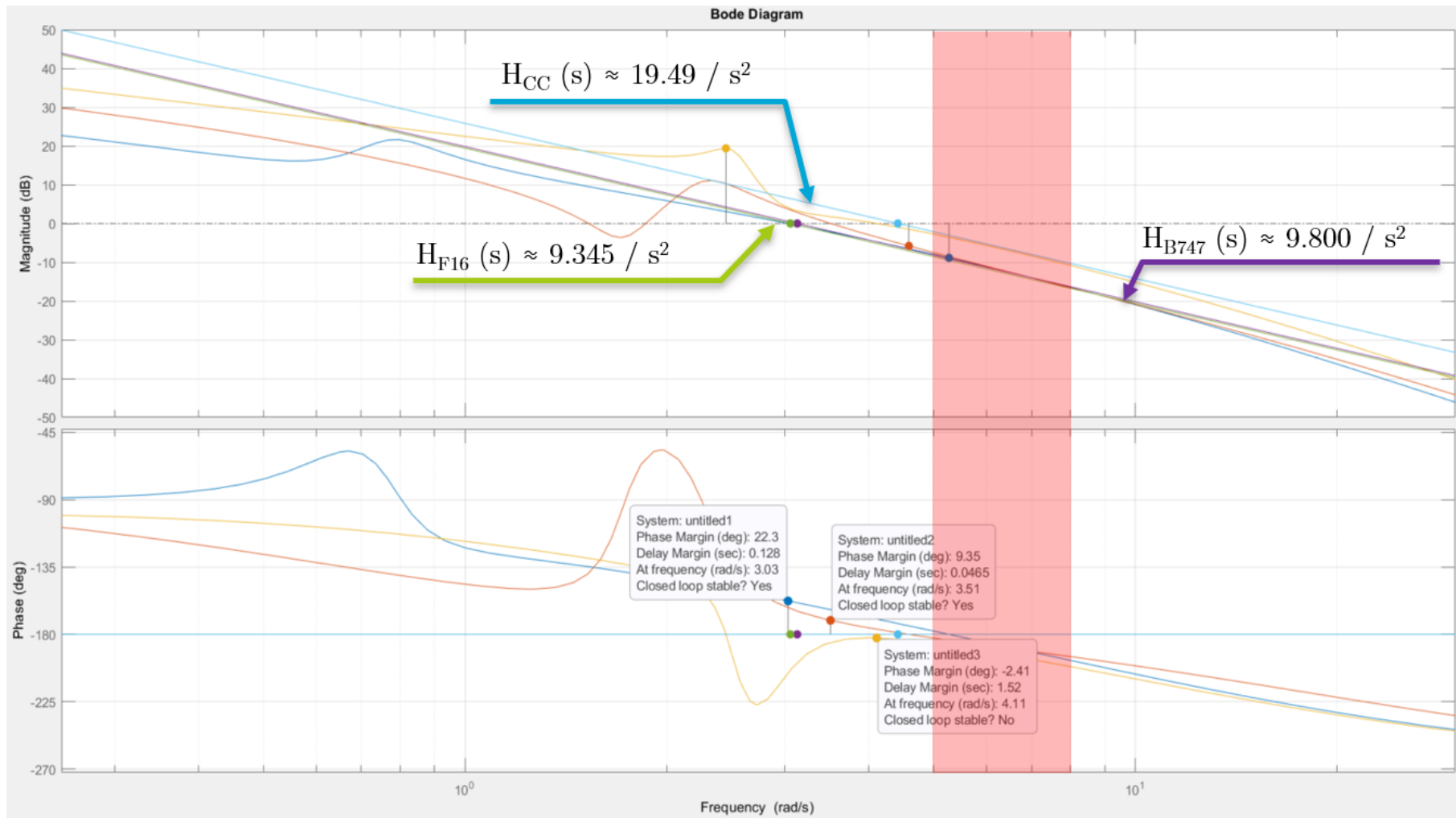


Figure 4.20: The CE dynamics shown earlier in Figure 4.11, combined with the second-order transfer functions that approximate the three aircraft in the human crossover region (indicated in red).

4.7. Testing conditions and performance predictions

In order to gain as much information as possible about the validity of the tuning procedure proposed in Section 4.6, there are three parameters that will be varied during the upcoming experiment: the active stick settings K_{fwd} and $K_{\dot{\phi}}$, as well as the CE dynamics. As Fu [14] stated earlier, about 15-20 minutes of simulator time was required per testing condition per participant to generate consistent data. To keep the required amount of simulator time within reasonable bounds and to make sure that participants will not suffer from loss of concentration and/or motivation, it was therefore decided that a maximum of 6-8 conditions would be tested per participant. This resulted in the testing conditions shown in Table 4.11, where all participants will be exposed to the six green conditions and to one of the four yellow *experimental* conditions.

Table 4.11: *The conditions to be tested in the experiment. The six green scenarios will be tested by all participants, whereas every participant will only test one of the four yellow experimental conditions.*

Aircraft	$K_{\dot{\phi}}$	K_{fwd}		
		$(K_{fwd})_{opt}$	$2 \cdot (K_{fwd})_{opt}$	$3 \cdot (K_{fwd})_{opt}$
B747	$(K_{\dot{\phi}})_{opt} (= -0.2105)$	1	2	7
	$2 \cdot (K_{\dot{\phi}})_{opt} (= -0.4210)$	3	8	
Cessna Citation	$(K_{\dot{\phi}})_{opt} (= -0.2105)$	4	5	9
	$2 \cdot (K_{\dot{\phi}})_{opt} (= -0.4210)$	6	10	

Testing conditions rationale

As this thesis is focused on finding an approach for determining the most promising settings for K_{fwd} and $K_{\dot{\phi}}$, it means that testing all three simulated aircraft is simply not feasible. The simulated Boeing 747 and F-16 resulted in similar HC performance and called for nearly the same active stick settings based on the proposed tuning procedure, which is why one of them is the most suitable candidate to be left out. To increase consistency with the data generated by Fu [14] earlier using the Boeing 747, said aircraft made it through the selection together with the Cessna Citation.

Naturally, both aircraft will be tested with the active stick settings that are deemed optimal based on the information presented in Sections 4.4, 4.5 and 4.6, which corresponds with conditions 1 and 4. The feedback gain related to these scenarios is identical, in line with the first hypothesis that is stated in Section 4.5. The feed-forward gains, on the other hand, are different per aircraft ($K_{fwd} = 3.5$ for the Boeing 747 and $K_{fwd} = 2$ for the Cessna Citation), in line with the second hypothesis stated in Section 4.5 and the observations made in Section 4.4. Besides that, alternative active stick settings are tested to validate the performance trends that are visible in the simulation output. These include a feed-forward gain that is double the optimal value (conditions 2 and 5) and a feedback gain that is double the optimal value (conditions 3 and 6).

The oscillatory behavior that occurred for the light gray model conditions introduced in Figures 4.14, 4.15 and 4.16 of Section 4.4 raises questions about what happens for these hardware settings in practice. To gain a better understanding of this, four more 'exotic' settings involving a higher collective open-loop gain are being tested as well, albeit with only a quarter of the participants each. For the first exotic conditions, the feed-forward gain is three times the optimal value (conditions 7 and 9). For the second exotic conditions, both the feed-forward and feedback gain are double their optimal value (conditions 8 and 10). To maximize our understanding of what happens inside the oscillatory zone, the first exotic conditions have been defined such that they are just barely within said zone, whereas the second exotic conditions are located well within it. Figure 4.21 provides a visual representation of where these testing conditions are located inside the simulation output matrices shown earlier in Figures 4.14 and 4.16.

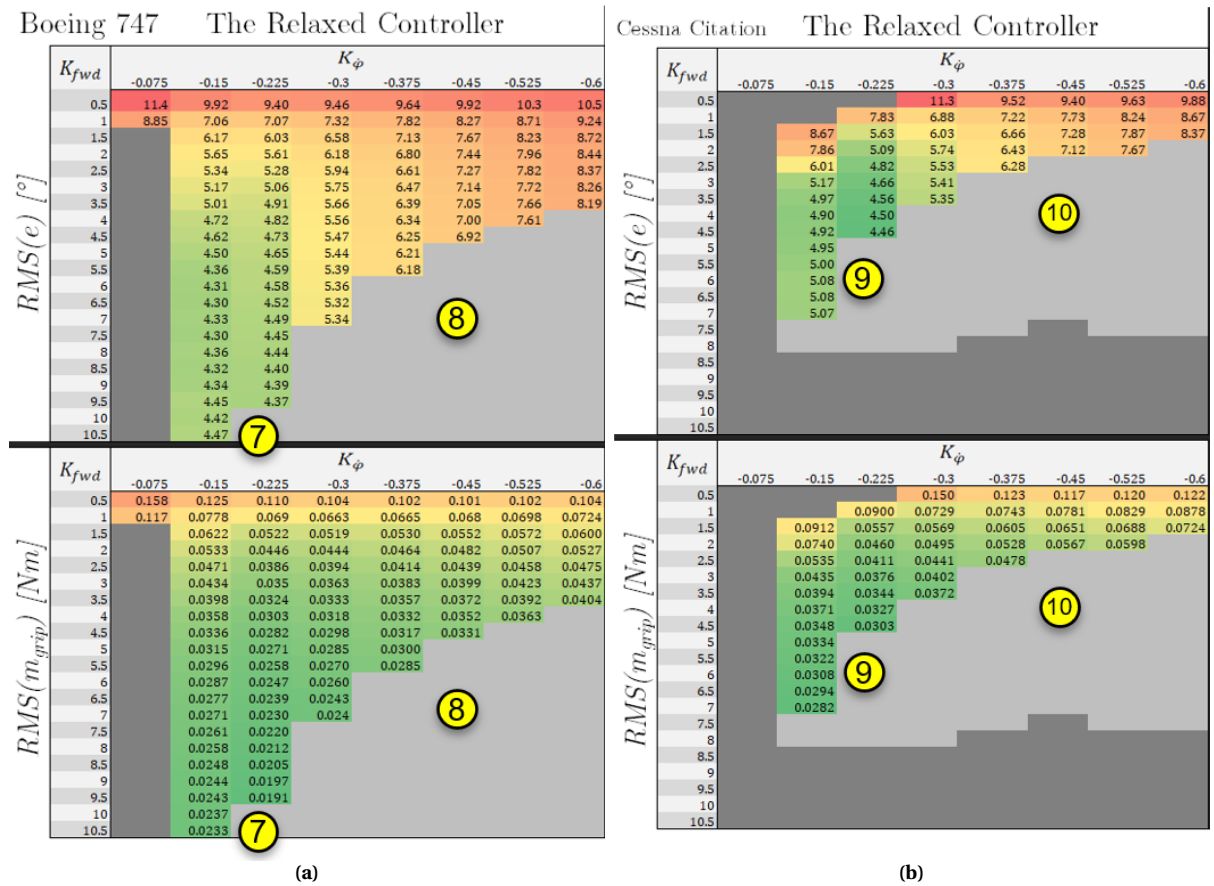


Figure 4.21: An illustration of where inside the oscillatory zone of the simulation output the 'exotic' testing conditions are located for (a) the Boeing 747 and (b) the Cessna Citation.

Performance predictions

To predict the performance of the HC for the various testing conditions, assumptions need to be made first regarding the aggressiveness of the HC's control behavior. Based on the experimental results shown in Figure 4.19, it is deemed reasonable that the HCs will act most like the modeled 'tense' pilot for the testing conditions that have an optimal feed-forward and feedback gain (conditions 1 and 2). For the conditions that have a somewhat larger collective open-loop gain (conditions 3 to 6), the HC is assumed to behave like the average controller. For the more exotic testing conditions that have an even larger open-loop gain (conditions 7 to 10), the relaxed pilot setting is deemed the most reasonable, as the simulation output suggests that these conditions in particular are prone to system instability. Performance predictions for all testing conditions with their respective HC settings have been generated in the same way that data was generated for the model conditions, as explained at the start of Section 4.4. This resulted in the performance predictions shown in Figure 4.22. Looking at the figure, several things can be noticed:

- Among the testing conditions where an average pilot setting is employed (conditions 2, 3, 5 and 6), the conditions involving the supposed $(K_{\phi})_{opt}$ seem to outperform the settings involving the supposed $(K_{fwd})_{opt}$ greatly, which is also supported by the previous simulation output from Section 4.4.
- When the HC becomes more aggressive, the performance changes differently depending on the CE dynamics. For the slower Boeing 747, there still seems to be a bit of tracking performance to be gained (which can be seen by comparing point 2 and 1), however the HC actually seems to be worse off in this regard for the more nervous Cessna Citation, not to mention the extra effort that is required to control both aircraft.

- As mentioned before in observation 6 from Section 4.4, active stick settings involving a higher K_{fwd} combined with more relaxed pilot control behavior do seem to provide superior overall performance (which is supported by comparing conditions 1 and 4 with conditions 2 and 5), however this assessment does not assign any value to the stability margins of the resulting system. Poorly trained pilots who control the aircraft too aggressively should to a reasonable extent be protected from destabilizing the system, which is why a comparison of conditions 1, 2 & 7 and 4, 5 & 9 will hopefully provide valuable insight as to what value for K_{fwd} is preferred.

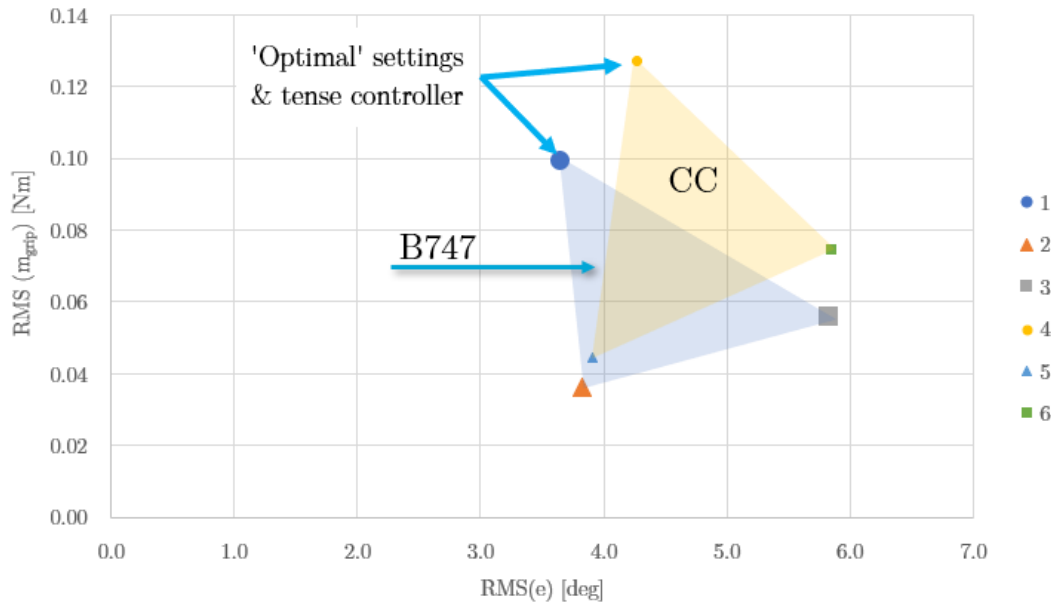


Figure 4.22: A prediction of the HC's performance for testing conditions 1 to 6, which are introduced in Table 4.11.

Reflection on the possible extent to which the proposed tuning procedure is validated with the presented experiment

The primary objective of this thesis is to determine design guidelines for the active stick configuration. Considering this concept relies heavily on the HC's reflexive response, this was done by fitting the existing experimental data on a model that contains a detailed description of the NMS, combined with a relatively simple representation of the HC's cognitive response as a PID-block, as the latter is less critical for the active stick's working principle. The simulation output that came as a result of this, combined with the existing findings about the active stick and the available crossover theory from McRuer [1], does provide clues for active stick design guidelines, however there are numerous experimental dimensions that need to be checked or accounted for, before a strong case for these guidelines can be made. If the experimental results turn out as expected, it would provide a respectable amount of support for the proposed tuning procedure, as it would indicate $(K_{\phi})_{opt}$'s independence of H_c as well as the pilot's control behavior (whose supposed dependency seems small enough to be neglected, as stated in Section 4.5). It would also provide more insight as to what the optimal setting for K_{fwd} is, which *does* seem to be affected by both the CE dynamics and the HC's control behavior.

A follow-up experiment which is omitted in this thesis (due to the added amount of work) is one where a different control setting is tested (i.e., the same side stick, but in pure pitch motion). If the preferred ω_c is found for that setting for single integrator CE dynamics and the corresponding K_{ϕ} as proposed in this thesis ($= 1/\omega_c$) provides the best results, that would add considerable credibility to the tuning procedure introduced in Section 4.6. This could then be expanded to a roll-pitch compensatory tracking task (in accordance with the roadmap laid out in Figure 2.8), to check whether the best settings for the separate DOFs are also the best ones for the 2-DOF control task.

5

Experiment design

Throughout the previous chapters, many aspects of the upcoming experiment have already been revealed. Section 5.1 serves as a summary that revisits all relevant aspects that define the experiment through references to previous sections, and provides additional information where necessary. This is followed by Section 5.2, which revolves around the envisioned data analysis that will take place after the experiment.

5.1. Summary of the experimental setting

The upcoming experiment is defined by the following elements:

- **Experimental hardware.** Section 2.5 summarizes the experimental setting that was used by Fu [14] and will be used for this thesis, as well as the test scenarios and findings produced by Fu earlier. Participants are seated in the HMI-lab, a fixed-base simulator environment at the TU Delft. Figure 2.4 shows the hardware that is used for carrying out the task: an 18-inch LCD screen and a two-axis hydraulically-driven manipulator.
- **Control task.** The participants are tasked with a one-dimensional control task, where they only have to control the aircraft's roll angle ϕ . For this reason, the servo motor responsible for the manipulator's pitch motion is constrained in the neutral position. Participants need to keep the aircraft level with the horizon, which they do based on the artificial that is shown to them on the LCD screen. As Figure 2.6b shows, participants can only base their cognitive response on the perceived error angle e , which means that this can be classified as a compensatory tracking task, like the one shown in Figure 2.1.
- **Controlled element dynamics.** The participants will control two different sets of aircraft dynamics: the adjusted Boeing 747 dynamics that were used by Fu [14] earlier (see Equation 2.4) and those of the Cessna Citation, whose dynamics were identified by the TU Delft at 30000 ft standard altitude and a velocity of 398 ft/s ($V = 121.3$ m/s, $M = 0.4$) [49]. Section 4.3 describes how the stability and control derivatives have been translated into the final transfer function shown in Equation 4.12.
- **Forcing functions.** The target and disturbance forcing functions f_t and f_d are both the sum of ten sinusoids, whose amplitudes and frequency components are shown in Tables 4.8 and 4.9, respectively. To prevent the participants from recognizing any patterns in the signal (thereby to a certain degree turning the compensatory tracking task into a preview tracking task, see Section 2.1), the phase angles of all sinusoid components are randomized for every test run.
- **Testing programme.** Table 4.11 shows the six testing conditions that will be tested by all participants, after which every participant will test one of the four exotic conditions. Every test run lasts 90 seconds, of which the last 81.92 seconds are used for data analysis. It is expected that the same amount of test runs per participant per condition is needed to generate consistent data, as was the case for Fu [14] (8-10 runs). Considering sufficient time for breaks between test runs and the possibility of the exotic condition being outright unstable, the average simulator time required for every participant is estimated to be ≈ 2.5 hours. Given that six conditions are to be tested thoroughly, a participant count of twelve is desired, such that a Latin square can be filled by the participants effectively.

5.2. Envisioned data analysis

The signals that will be measured during the experiment are:

- The tracking error e
- The grip force applied to the manipulator m_{grip}

After the experiment, the root-mean-square (RMS) of both variables will be determined for every participant in every condition, by taking the average of the measured RMS-values over five consecutive runs. The tracking error will undergo a frequency-domain analysis, which will produce a:

- Target tracking frequency response function (FRF), which in turn produces a target tracking gain crossover frequency and phase margin as well.
- Disturbance rejection FRE, which in turn produces a disturbance rejection gain crossover frequency and phase margin as well.

For the Bode plots also holds that the plots from five consecutive runs will be averaged to determine the final plots belonging to a given participant for a given condition. For every testing condition, these data of all twelve participants will be combined to determine a grand mean and standard deviation for every data point in every Bode plot. As such, the Bode plots will be used to compare HC performance for the various testing conditions in the frequency-domain.

For the crossover characteristics, the averaged values for every participant in every condition will be collected to determine the grand mean of these parameters for every condition. Assuming that the data is normally distributed due to the number of participants involved, a 95% confidence interval will be reported that is based on $\pm 1.96\sigma$ of the respective data sets.

To determine whether the active stick settings and the used aircraft dynamics have a significant impact on the HC's tracking performance (which can be related to $RMS(e)$, ω_c and ϕ_m) and on the physical workload (i.e., $RMS(m_{grip})$), the data of all participants will be subjected to a three-way repeated-measures analysis of variance (ANOVA). Mauchly's test will first be used to check whether the assumption of sphericity among the data is violated. If a significance value of < 0.05 is reported for any of the parameters that is varied (i.e., the aircraft, K_{fwd} or K_{ϕ}), their corresponding DOF-value (which are all equal to: 2 setting levels - 1 = 1) needs to be scaled either using the relatively conservative Greenhouse-Geisser correction or the Huynh-Feldt correction [52]. Afterwards, the (potentially corrected) F-ratios will tell whether any of the involved parameters has a significant impact on the experimental outcome and whether there are any significant interactions between said parameters.

Finally, a very short questionnaire may quantify the participant's subjective response as to how they experienced controlling the different aircraft at different settings in terms of difficulty and user comfort.

6

Conclusion

This report contains a research proposal for the determination of design guidelines for the 'active stick' configuration that has been introduced by Hosman [15] and was further studied by Fu [14] more recently. The proposed tuning procedure, on which the presented testing conditions are based, was determined through several steps that can best be summarized as:

1. A literature review, most notably of the active stick's working principle as expanded upon by Fu [14], the concepts inherently related to said principle (i.e., the neuromuscular system) and the control task at hand.
2. The construction of a Simulink model that replicates the experiment that was conducted by Fu [14], and which will be conducted in this thesis. The majority of attention in terms of modelling detail is paid to the neuromuscular system, as this system plays a pivotal role in the active stick's working principle. To facilitate this, the Delft neuromuscular model as presented by De Vlugt [34] forms the core element of the Simulink model.
3. The estimation of the eighteen coefficients that define the pilot's control behavior in the model, by fitting the Simulink model on the existing experimental data generated by Fu [14]. The different forcing function bandwidths tested by Fu allowed for the estimation of three different pilot settings, to account for the fact that pilots may exert a wide range of control behavior due to their adaptive nature.
4. The identification of trends in performance, by simulating 186 different active stick settings for three different aircraft (the Boeing 747 as used by Fu [14], the F-16 fighter jet and the Cessna 500 Citation) with the three pilot settings that were determined previously.
5. The reflection on existing manual control theory as well as the findings produced by Fu [14], which provided a possible explanation for the performance trends and formed the basis on which the proposed tuning procedure was formed.

Bibliography

- [1] Duane T. McRuer et al. *Human Pilot Dynamics in Compensatory Systems. Theory, Models, and Experiments with Controlled Element and Forcing Function Variations. Technical Report AFFDL-TR-65-15*. Tech. rep. Air Force Flight Dynamics Laboratory, 1965.
- [2] British Ministry of Aviation. “British Aircraft Corporation Ltd. BAC 1-11 Series 200 G-ASGH Accident Report No. EW/C/039”. In: *ICAO Circular 78-AN/66* (1964), pp. 55–67.
- [3] P.R. Kurzhals. *Active Controls in Aircraft Design*. NATO Advisory Group for Aerospace Research and Development, 1978. ISBN: 92-835-0225-6.
- [4] George R. Schmidt, Geoffrey A. Landis, and Steven R. Oleson. “HERRO Missions to Mars and Venus using Telerobotic Surface Exploration from Orbit”. In: *NASA Glenn Research Center* (2012).
- [5] Dana R. Yoerger and Jean-Jacques E. Slotine. “Supervisory Control Architecture for Underwater Teleoperation”. In: *Proceedings. 1987 IEEE International Conference on Robotics and Automation* (1987). DOI: [10.1109/ROBOT.1987.1087890](https://doi.org/10.1109/ROBOT.1987.1087890).
- [6] Anthony R. Lanfranco et al. “Robotic Surgery: A Current Perspective”. In: *Annals of Surgery* 239 (1 Jan. 2004), pp. 14–21. ISSN: 00034932. DOI: [10.1097/01.sla.0000103020.19595.7d](https://doi.org/10.1097/01.sla.0000103020.19595.7d).
- [7] Issam El Rassi and Jean Michel El Rassi. “A review of haptic feedback in tele-operated robotic surgery”. In: *Journal of Medical Engineering and Technology* 44 (5 July 2020), pp. 247–254. ISSN: 1464522X. DOI: [10.1080/03091902.2020.1772391](https://doi.org/10.1080/03091902.2020.1772391).
- [8] Joao Rebelo et al. “Bilateral robot teleoperation: A wearable arm exoskeleton featuring an intuitive user interface”. In: *IEEE Robotics and Automation Magazine* 21 (4 Dec. 2014), pp. 62–69. ISSN: 10709932. DOI: [10.1109/MRA.2014.2360308](https://doi.org/10.1109/MRA.2014.2360308).
- [9] Micah Steele and Brent Gillespie. “Shared Control between Human and Machine: Using a Haptic Steering Wheel to Aid in Land Vehicle Guidance”. In: *Proceedings of the Human Factors and Ergonomics Society Annual Meeting* 45 (Oct. 2001), pp. 1671–1675. DOI: [10.1177/154193120104502323](https://doi.org/10.1177/154193120104502323).
- [10] Paul G. Griffiths and R. Brent Gillespie. “Sharing Control Between Humans and Automation Using Haptic Interface: Primary and Secondary Task Performance Benefits”. In: *Human Factors* 47 (3 2005), pp. 574–590. ISSN: 0018-7208. DOI: [10.1518/001872005774859944](https://doi.org/10.1518/001872005774859944).
- [11] David A. Abbink, Mark Mulder, and Erwin R. Boer. “Haptic shared control: Smoothly shifting control authority?” In: *Cognition, Technology and Work* 14 (1 Mar. 2012), pp. 19–28. ISSN: 14355558. DOI: [10.1007/s10111-011-0192-5](https://doi.org/10.1007/s10111-011-0192-5).
- [12] Joost Ellerbroek et al. “Design and evaluation of a Flight Envelope Protection haptic feedback system”. In: *IFAC-PapersOnLine* 49 (19 2016), pp. 171–176. ISSN: 24058963. DOI: [10.1016/j.ifacol.2016.10.481](https://doi.org/10.1016/j.ifacol.2016.10.481).
- [13] Dirk van Baelen et al. “Design of a haptic feedback system for flight envelope protection”. In: *Journal of Guidance, Control, and Dynamics* 43 (4 2020), pp. 700–714. ISSN: 15333884. DOI: [10.2514/1.G004596](https://doi.org/10.2514/1.G004596).
- [14] Wei Fu, M.M. (René) van Paassen, and Max Mulder. “Developing Active Manipulators in Aircraft Flight Control”. In: *Journal of Guidance, Control, and Dynamics* 42.8 (Aug. 2019), pp. 1755–1767. ISSN: 1533-3884. DOI: [10.2514/1.G004186](https://doi.org/10.2514/1.G004186). URL: <https://arc.aiaa.org/doi/10.2514/1.G004186>.
- [15] Ruud J.A.W. Hosman and J.C. (Hans) van der Vaart. “Active and passive side stick controllers: Tracking task performance and pilot control behavior”. In: *AGARD Conference Proceedings No. 425: The Man-Machine Interface in Tactical Aircraft Design and Combat Automation* (1987). URL: <https://www.researchgate.net/publication/309013900>.

- [16] Wei Fu. “Evidence-based development and evaluation of haptic interfaces for manual control.” In: (2019). DOI: [10.4233/uuid:b5953a17-322d-49e6-87ba-e299673e8b84](https://doi.org/10.4233/uuid:b5953a17-322d-49e6-87ba-e299673e8b84).
- [17] Lawrence K. Loftin Jr. *Quest for Performance: the Evolution of Modern Aircraft*. Tech. rep. NASA Report NAS 1.21:468, 1985.
- [18] Jan Smisek et al. “Neuromuscular-System-Based Tuning of a Haptic Shared Control Interface for UAV Teleoperation”. In: *IEEE Transactions on Human-Machine Systems* 47 (4 Aug. 2017), pp. 449–461. ISSN: 21682291. DOI: [10.1109/THMS.2016.2616280](https://doi.org/10.1109/THMS.2016.2616280).
- [19] Sujit Rajappa, Heinrich Bülthoff, and Paolo Stegagno. “Design and implementation of a novel architecture for physical human-UAV interaction”. In: *International Journal of Robotics Research* 36 (5-7 June 2017), pp. 800–819. ISSN: 17413176. DOI: [10.1177/0278364917708038](https://doi.org/10.1177/0278364917708038).
- [20] Giulia D’intino et al. “Haptic assistance for helicopter control based on pilot intent estimation”. In: *Journal of Aerospace Information Systems* 17 (4 2020), p. 193. ISSN: 23273097. DOI: [10.2514/1.I010773](https://doi.org/10.2514/1.I010773).
- [21] Michele Maimeri et al. “On effects of failures in haptic and automated pilot support systems”. In: American Institute of Aeronautics and Astronautics Inc, AIAA, 2016. ISBN: 9781624103872. DOI: [10.2514/6.2016-1181](https://doi.org/10.2514/6.2016-1181).
- [22] Joost Venrooij et al. “A biodynamic feedthrough model based on neuromuscular principles”. In: *IEEE Transactions on Cybernetics* 44 (7 2014), pp. 1141–1154. ISSN: 21682267. DOI: [10.1109/TCYB.2013.2280028](https://doi.org/10.1109/TCYB.2013.2280028).
- [23] Emmanuel Sunil et al. “Validation of a tuning method for haptic shared control using neuromuscular system analysis”. In: vol. 2014-January. Institute of Electrical and Electronics Engineers Inc., 2014, pp. 1499–1504. DOI: [10.1109/smc.2014.6974128](https://doi.org/10.1109/smc.2014.6974128).
- [24] Samantha M.C. Alaimo et al. “Evaluation of direct and indirect Haptic aiding in an obstacle avoidance task for tele-operated systems”. In: vol. 44. IFAC Secretariat, 2011, pp. 6472–6477. ISBN: 9783902661937. DOI: [10.3182/20110828-6-IT-1002.02790](https://doi.org/10.3182/20110828-6-IT-1002.02790).
- [25] Samantha M.C. Alaimo, Lorenzo Pollinit, and Heinrich H. Buelthoff. “Admittance-based bilateral teleoperation with time delay for an unmanned aerial vehicle involved in an obstacle avoidance task”. In: American Institute of Aeronautics and Astronautics Inc., 2011, pp. 19–37. ISBN: 9781624101540. DOI: [10.2514/6.2011-6243](https://doi.org/10.2514/6.2011-6243).
- [26] Derek G. Beeftink et al. “Haptic Support for Aircraft Approaches with a Perspective Flight-Path Display”. In: Institute of Electrical and Electronics Engineers Inc., July 2018, pp. 3016–3021. ISBN: 9781538666500. DOI: [10.1109/SMC.2018.00512](https://doi.org/10.1109/SMC.2018.00512).
- [27] Frank M. Nieuwenhuizen and Heinrich H. Bülthoff. “Evaluation of haptic shared control and a highway-in-the-sky display for personal aerial vehicles”. In: American Institute of Aeronautics and Astronautics Inc., 2014. ISBN: 9781624102974. DOI: [10.2514/6.2014-0808](https://doi.org/10.2514/6.2014-0808).
- [28] Samantha M.C. Alaimo et al. “Preliminary evaluation of a haptic aiding concept for remotely piloted vehicles”. In: vol. 6192 LNCS. 2010, pp. 418–425. ISBN: 3642140742. DOI: [10.1007/978-3-642-14075-4_62](https://doi.org/10.1007/978-3-642-14075-4_62).
- [29] Ruud J.A.W. Hosman, Bart Benard, and Helene Fourquet. “Active and passive side-stick controllers in manual aircraft control”. In: *Proceedings of the IEEE International Conference on Systems, Man and Cybernetics* (Nov. 1990), pp. 527–529. ISSN: 08843627. DOI: [10.1109/icsmc.1990.142165](https://doi.org/10.1109/icsmc.1990.142165).
- [30] Winfred Mugge et al. “A rigorous model of reflex function indicates that position and force feedback are flexibly tuned to position and force tasks”. In: *Experimental Brain Research* 200 (3-4 Jan. 2010), pp. 325–340. ISSN: 00144819. DOI: [10.1007/s00221-009-1985-0](https://doi.org/10.1007/s00221-009-1985-0).

- [31] Duane T. McRuer and Henry R. Jex. "A Review of Quasi-Linear Pilot Models". In: *IEEE Transactions on Human Factors in Electronics* 8 (3 1967), pp. 231–249.
- [32] Alfred C. Schouten. "Proprioceptive reflexes and neurological disorders". PhD thesis. Delft University of Technology, 2004.
- [33] M.M. (René) van Paassen. "Biophysics in aircraft control: A model of the neuromuscular system of the pilot's arm". PhD thesis. Delft University of Technology, 1994. ISBN: 90-9007265-9.
- [34] Erwin de Vlugt, Alfred C. Schouten, and Frans C.T. van der Helm. "Quantification of intrinsic and reflexive properties during multijoint arm posture". In: *Journal of Neuroscience Methods* 155.2 (Sept. 2006), pp. 328–349. ISSN: 01650270. DOI: [10.1016/j.jneumeth.2006.01.022](https://doi.org/10.1016/j.jneumeth.2006.01.022).
- [35] E. R. Kandel, James H Schwartz, and Thomas M Jessell. *Principles of Neural Science*. 4th ed. McGraw-Hill, 2000, pp. 106–170. ISBN: 0838577016. URL: <http://www.amazon.com/Principles-Neural-Science-Eric-Kandel/dp/0838577016>.
- [36] Frans C.T. van der Helm et al. "Identification of intrinsic and reflexive components of human arm dynamics during postural control". In: *Journal of Neuroscience Methods* 119.1 (2002), pp. 1–14. ISSN: 01650270. DOI: [10.1016/S0165-0270\(02\)00147-4](https://doi.org/10.1016/S0165-0270(02)00147-4). URL: www.elsevier.com/locate/jneumeth.
- [37] M.M. (René) van Paasen, J.C. (Hans) van der Vaart, and J.A. (Bob) Mulder. "Model of the Neuromuscular Dynamics of the Human Pilot's Arm". In: *Journal of Aircraft* 41.6 (Nov. 2004), pp. 1482–1490. ISSN: 0021-8669. DOI: [10.2514/1.14434](https://doi.org/10.2514/1.14434). URL: <https://arc.aiaa.org/doi/10.2514/1.14434>.
- [38] A. Sandow. "Excitation-contraction coupling in muscular response." In: *The Yale journal of biology and medicine* 25.3 (Dec. 1952), pp. 176–201. ISSN: 0044-0086.
- [39] Erwin de Vlugt. "Identification of Spinal Reflexes". PhD thesis. Delft University of Technology, 2004, pp. 1–256. ISBN: 9077595422.
- [40] Aditya Jain et al. "A comparative study of visual and auditory reaction times on the basis of gender and physical activity levels of medical first year students". In: *International Journal of Applied and Basic Medical Research* 5 (2 2015), p. 124. ISSN: 2229-516X. DOI: [10.4103/2229-516x.157168](https://doi.org/10.4103/2229-516x.157168).
- [41] Henry R. Jex. "Problems in Modeling Man-Machine Control Behavior in Biodynamic Environments". In: *Seventh Annual Conference on Manual Control* (1972), pp. 3–12.
- [42] William H. Levison and David L. Kleinman. "A Model for Human Controller Remnant". In: *IEEE Transactions on Man-Machine Systems* 10 (4 1969).
- [43] Kasper van der El, Daan M. Pool, and Max Mulder. "Analysis of Human Remnant in Pursuit and Preview Tracking Tasks". In: *IFAC-PapersOnLine* 52 (19 2019), pp. 145–150. ISSN: 24058963. DOI: [10.1016/j.ifacol.2019.12.165](https://doi.org/10.1016/j.ifacol.2019.12.165).
- [44] David L. Kleinman, S. Baron, and William H. Levison. "An Optimal Control Model of Human Response Part I: Theory and Validation". In: *Automatica* 6 (1970), pp. 357–369.
- [45] Antonia F. de C. Hamilton, Kelvin E. Jones, and Daniel M. Wolpert. "The scaling of motor noise with muscle strength and motor unit number in humans". In: *Experimental Brain Research* 157 (4 2004), pp. 417–430. ISSN: 00144819. DOI: [10.1007/s00221-004-1856-7](https://doi.org/10.1007/s00221-004-1856-7).
- [46] Anand K. Bhoelai et al. "Design of Test Signals for Identification of Neuromuscular Admittance". In: *IFAC-PapersOnLine* 49 (19 2016), pp. 266–271. ISSN: 24058963. DOI: [10.1016/j.ifacol.2016.10.544](https://doi.org/10.1016/j.ifacol.2016.10.544).
- [47] Joost Lasschuit. "Modeling the Neuromuscular System Dynamics for Haptic Interface Design; Identification of the NMS in multiple directions". Unpublished MSc thesis. Delft University of Technology, 2007.

-
- [48] Thanh M. Lam. “Haptic Interface for UAV Teleoperation”. In: PhD thesis. Delft University of Technology, 2009. ISBN: 978-90-9024199-9.
- [49] J.A. (Bob) Mulder et al. *Aircraft Responses to Atmospheric Turbulence Lecture Notes AE4304*. 2016.
- [50] Richard S. Russell. *Non-linear F-16 Simulation using Simulink and Matlab*. University of Minnesota, June 2003.
- [51] Brian L. Stevens and Frank L. Lewis. *Aircraft Control and Simulation*. 1st ed. Wiley Interscience, 1992. ISBN: 9780471613978.
- [52] Andy Field. *Discovering statistics using IBM SPSS statistics*. 4th ed. SAGE Publications Ltd, 2013. ISBN: 978-1-4462-4917-8.

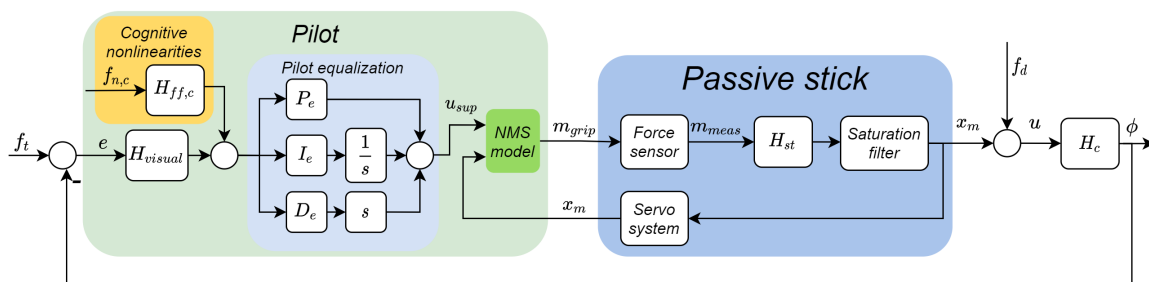
III

Preliminary thesis appendix (previously
graded under AE4020)

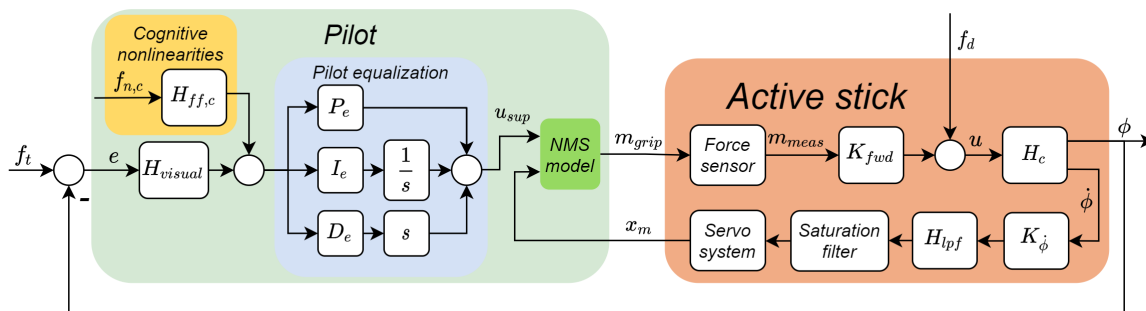
A

Analytical transfer function derivations

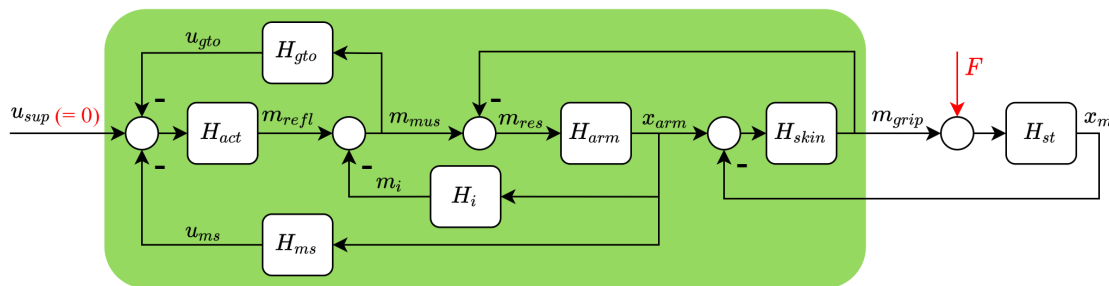
This appendix contains the analytical derivations for the passive and active stick models presented in Figures 3.3a and 3.3c, which have been repeated here respectively for convenience. The derivations largely revolve around the TU Delft neuromuscular model introduced in Figure 3.1, which has been repeated here as well.



(a) The passive stick model (Figure 3.3a).



(b) The active stick model (Figure 3.3c).



(c) The TU Delft neuromuscular model (Figure 3.1).

For all derivations holds that $H_{skin} = H_1$, $I_{arm} = H_2$, $H_i = H_3$, $H_{ms} = H_4$, $H_{gto} = H_5$ and $H_{act} = H_6$, which means that:

$$\begin{aligned} m_{grip} &= H_1(x_{arm} - x_m) \\ x_{arm} &= H_2(m_{mus} - m_{grip}) \\ m_i &= H_3x_{arm} \\ u_{ms} &= H_4x_{arm} \\ u_{gto} &= H_5m_{mus} \\ m_{refl} &= H_6(u_{sup} - u_{ms} - u_{gto}) \end{aligned}$$

For the sake of brevity and clarity, some recurring sets of variables have been defined as:

$$\begin{aligned} Q &= H_{lpf}H_{hfb} \\ \Gamma &= 1 + H_1H_2 \\ \Delta &= H_{visual} \left(P_e + \frac{I_e}{s} + D_e s \right) \\ \Theta &= 1 + H_6H_5 \\ \Lambda &= H_6H_4H_2 + H_3H_2 \end{aligned}$$

Target tracking

What set the two models apart are the relations that define the output ϕ and stick position x_m :

$$\begin{aligned} \phi_{act} &= H_c K_{fwd} m_{grip} \\ x_{m_{act}} &= H_{lpf} H_{hfb} \phi_{act} \\ \phi_{pas} &= H_c x_{m_{pas}} \\ x_{m_{pas}} &= H_{st} m_{grip} \end{aligned}$$

Active stick open-loop

Using the above information, the following derivations can be made for the active stick:

$$\begin{aligned} m_{grip} &= H_1(x_{arm} - x_m) \\ &= H_1 \left(H_2(m_{mus} - m_{grip}) - H_{lpf} H_{hfb} \phi_{act} \right) \\ &= H_1 \left(H_2(m_{mus} - m_{grip}) - Q\phi_{act} \right) \\ \Rightarrow m_{grip}(1 + H_1H_2 + H_1QH_cK_{fwd}) &= m_{grip}(\Gamma + H_1QH_cK_{fwd}) \\ &= H_1H_2m_{mus} \end{aligned} \tag{1}$$

$$\begin{aligned} m_{mus} &= H_6u_{sup} - H_6H_4x_{arm} - H_6H_5m_{mus} - H_3x_{arm} \\ &= H_6u_{sup} - H_6H_4H_2(m_{mus} - m_{grip}) - H_6H_5m_{mus} \\ &\quad - H_3H_2(m_{mus} - m_{grip}) \\ \Rightarrow m_{mus}(1 + H_6H_5 + H_6H_4H_2 + H_3H_2) &= H_6u_{sup} + (H_6H_4H_2 + H_3H_2)m_{grip} \\ \Rightarrow m_{mus}(\Lambda + \Theta) &= H_6u_{sup} + \Lambda m_{grip} \end{aligned}$$

$$\Rightarrow m_{mus} = \frac{H_6u_{sup} + \Lambda m_{grip}}{\Theta + \Lambda} \tag{2}$$

Substituting relation [2] into [1] gives:

$$\begin{aligned}
 m_{grip}(\Gamma + H_1 Q H_c K_{fwd}) &= \frac{H_1 H_2 H_6 u_{sup} + H_1 H_2 \Lambda m_{grip}}{\Theta + \Lambda} \\
 \Rightarrow m_{grip} \left(\Gamma + H_1 Q H_c K_{fwd} - \frac{H_1 H_2 \Lambda}{\Theta + \Lambda} \right) &= \frac{H_1 H_2 H_6}{\Theta + \Lambda} u_{sup} \\
 \Rightarrow \frac{m_{grip}}{u_{sup}} &= \frac{H_1 H_2 H_6}{(\Gamma + H_1 Q H_c K_{fwd})(\Theta + \Lambda) - H_1 H_2 \Lambda} \quad [3]
 \end{aligned}$$

Consequently, the active stick open-loop target tracking transfer function becomes:

$$\frac{\Phi_{act}(s)}{E_{act}(s)} = \frac{H_c K_{fwd} H_1 H_2 H_6 \Delta}{(\Gamma + H_1 Q H_c K_{fwd})(\Theta + \Lambda) - H_1 H_2 \Lambda}$$

Passive stick open-loop

For the passive stick, relation [1] needs to be changed to:

$$\begin{aligned}
 m_{grip} &= H_1 \left(H_2 (m_{mus} - m_{grip}) - H_{st} m_{grip} \right) \\
 \Rightarrow m_{grip} (\Gamma + H_1 H_{st}) &= H_1 H_2 m_{mus}
 \end{aligned}$$

Relation [2] remains unchanged, which means that [3] only needs a minor modification:

$$\begin{aligned}
 \Rightarrow m_{grip} \left(\Gamma + H_1 H_{st} - \frac{H_1 H_2 \Lambda}{\Theta + \Lambda} \right) &= \frac{H_1 H_2 H_6}{\Theta + \Lambda} u_{sup} \\
 \Rightarrow \frac{m_{grip}}{u_{sup}} &= \frac{H_1 H_2 H_6}{(\Gamma + H_1 H_{st})(\Theta + \Lambda) - H_1 H_2 \Lambda}
 \end{aligned}$$

Consequently, the passive stick open-loop target tracking transfer function becomes:

$$\frac{\Phi_{pas}(s)}{E_{pas}(s)} = \frac{H_c H_{st} H_1 H_2 H_6 \Delta}{(\Gamma + H_1 H_{st})(\Theta + \Lambda) - H_1 H_2 \Lambda}$$

Closed-loop

Since the loop is closed with unity feedback for both the active and passive stick, and $H_{OL} = \frac{A}{B}$, this means that $H_{CL} = \frac{\frac{A}{B}}{1 + \frac{A}{B}} = \frac{A}{B+A}$. Therefore, the active and passive stick closed-loop target tracking responses become:

$$\frac{\Phi_{act}(s)}{F_t(s)} = \frac{H_c K_{fwd} H_1 H_2 H_6 \Delta}{(\Gamma + H_1 Q H_c K_{fwd})(\Theta + \Lambda) - H_1 H_2 \Lambda + H_c K_{fwd} H_1 H_2 H_6 \Delta}$$

$$\frac{\Phi_{pas}(s)}{F_t(s)} = \frac{H_c H_{st} H_1 H_2 H_6 \Delta}{(\Gamma + H_1 H_{st})(\Theta + \Lambda) - H_1 H_2 \Lambda + H_c H_{st} H_1 H_2 H_6 \Delta}$$

Disturbance rejection

The open-loop disturbance rejection transfer function is defined as $H_{d,OL}(s) = \frac{U_p(s)}{F_d(s)}$. It is important to note that for the passive stick $u_{pas} = x_m$, whereas for the active stick $u_{pact} = K_{fwd} m_{grip}$. As the system is being cut at a different location compared to the open-loop target tracking response, these relations now apply:

$$\begin{aligned} x_{m_{act}} &= QH_c f_d \\ u_{sup} &= -\Delta H_c f_d \end{aligned}$$

Active stick open-loop

For the active stick, the open-loop disturbance rejection derivation is as follows:

$$\begin{aligned} m_{grip} &= H_1(x_{arm} - x_m) \\ x_{arm} &= H_2(m_{mus} - m_{grip}) \\ &= H_2\left(m_{mus} - H_1(x_{arm} - x_m)\right) \\ \Rightarrow \Gamma \cdot x_{arm} &= H_2 m_{mus} + H_1 H_2 Q H_c f_d \\ \Rightarrow x_{arm} &= \frac{H_2}{\Gamma} m_{mus} + \frac{H_1 H_2 Q H_c}{\Gamma} f_d \end{aligned} \quad [4]$$

$$\begin{aligned} m_{mus} &= H_6(u_{sup} - H_4 x_{arm} - H_5 m_{mus}) - H_3 x_{arm} \\ \Rightarrow \Theta \cdot m_{mus} &= H_6 u_{sup} - (H_6 H_4 + H_3) x_{arm} \end{aligned} \quad [5]$$

Substituting relation [4] into [5] gives:

$$\begin{aligned} \Theta \cdot m_{mus} &= -H_6 \Delta H_c f_d - (H_6 H_4 + H_3) \left(\frac{H_2}{\Gamma} m_{mus} + \frac{H_1 H_2 Q H_c}{\Gamma} f_d \right) \\ &= -H_6 \Delta H_c f_d - \frac{\Lambda}{\Gamma} m_{mus} - \frac{\Lambda H_1 Q H_c}{\Gamma} f_d \\ \Rightarrow \left(\Theta + \frac{\Lambda}{\Gamma} \right) m_{mus} &= - \left(H_6 \Delta H_c + \frac{\Lambda H_1 Q H_c}{\Gamma} \right) f_d \\ \Rightarrow m_{mus} &= \frac{- \left(H_6 \Delta H_c + \frac{\Lambda H_1 Q H_c}{\Gamma} \right)}{\Theta + \frac{\Lambda}{\Gamma}} f_d \end{aligned} \quad [6]$$

Substituting [6] back into [4] yields:

$$\begin{aligned} x_{arm} &= - \frac{H_2}{\Gamma} \left(\frac{H_6 \Delta H_c + \frac{\Lambda H_1 Q H_c}{\Gamma}}{\Theta + \frac{\Lambda}{\Gamma}} \right) f_d + \frac{H_1 H_2 Q H_c}{\Gamma} f_d \\ &= - \left(\frac{H_2 H_c (H_6 \Delta + \frac{\Lambda H_1 Q}{\Gamma})}{\Theta \Gamma + \Lambda} \right) f_d + \frac{H_1 H_2 Q H_c}{\Gamma} f_d \\ m_{grip} &= H_1(x_{arm} - x_m) \\ \Rightarrow m_{grip} &= - \left(\frac{H_1 H_2 H_c (H_6 \Delta + \frac{\Lambda H_1 Q}{\Gamma})}{\Theta \Gamma + \Lambda} \right) f_d + \frac{H_1 H_1 H_2 Q H_c}{\Gamma} f_d - H_1 Q H_c f_d \end{aligned}$$

Rearranging the terms, this becomes:

$$\begin{aligned} \frac{m_{grip}}{f_d} &= H_1 H_c \left(\frac{H_1 H_2 Q}{\Gamma} - \left(\frac{H_2 H_6 \Delta + \frac{\Lambda H_1 H_2 Q}{\Gamma}}{\Gamma \Theta + \Lambda} \right) - Q \right) \\ \Rightarrow \frac{U_{p_{act}}(s)}{F_d(s)} &= H_1 H_c K_{fwd} \left(\frac{H_1 H_2 Q}{\Gamma} - \left(\frac{H_2 H_6 \Delta + \frac{\Lambda H_1 H_2 Q}{\Gamma}}{\Gamma \Theta + \Lambda} \right) - Q \right) \\ &= \frac{H_1 H_c K_{fwd}}{\Gamma} \left(H_1 H_2 Q - \frac{H_2 H_6 \Delta \Gamma + \Lambda H_1 H_2 Q}{\Gamma \Theta + \Lambda} - Q \Gamma \right) \end{aligned}$$

Passive stick open-loop

For the passive stick, the open-loop disturbance rejection response is essentially identical to the open-loop target tracking response, but it is flipped by 180 degrees. Figure A.2 shows how both transfer functions are the product of the same elements, with the exception of the '-1' multiplication that only occurs for the disturbance rejection, due to the compensator located at the very left of Figure 3.3a.

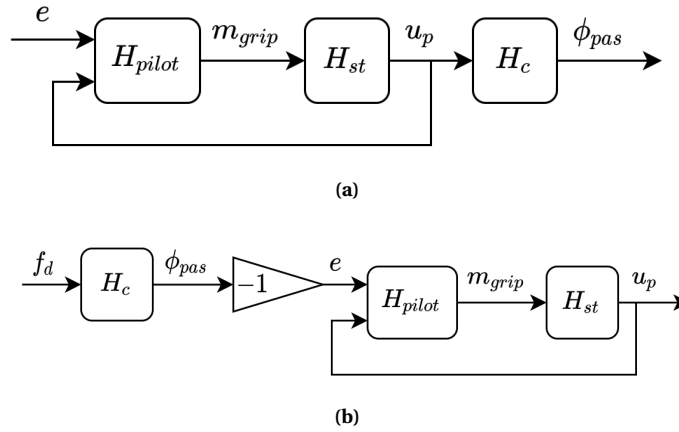


Figure A.2: A simplified block diagram of the passive stick a) target tracking and b) disturbance rejection open-loop response, that aims to highlight their similarity.

This leads to a passive stick open-loop disturbance rejection response of:

$$\frac{U_{p_{pas}}(s)}{F_d(s)} = \frac{-H_c H_{st} H_1 H_2 H_6 \Delta}{(\Gamma + H_1 H_{st})(\Theta + \Lambda) - H_1 H_2 \Lambda}$$

Closed-loop

The closed-loop disturbance rejection transfer function is defined as the system's response in terms of roll angle ϕ to a disturbance that is introduced *after* the controlled element dynamics. Regardless of the fact that in this thesis the disturbance signal is introduced *before* the CE dynamics (as can be seen in Figures 3.3a and 3.3c), the closed-loop disturbance rejection responses can be derived from their open-loop counterparts in a straightforward manner. Considering the point above, the fact that there is a *summation point* and *not* a compensator at the location where f_d is introduced into the system (in other words, the closed-loop system has a *positive* feedback loop) and the fact that there is unity feedback in the outer loop, the closed-loop disturbance rejection response can be summarized as:

$$H_{d_{CL}}(s) = \frac{1}{1 - H_{d_{OL}}(s)}$$

This means that the active and passive stick closed-loop disturbance rejection response can be defined as:

$$\begin{aligned} \frac{\Phi_{act}(s)}{F_d(s)} &= \frac{1}{1 - \frac{H_1 H_c K_{fwd}}{\Gamma} \left(H_1 H_2 Q - \frac{H_2 H_6 \Delta \Gamma + \Lambda H_1 H_2 Q}{\Gamma \Theta + \Lambda} - Q \Gamma \right)} \\ &= \frac{\Gamma}{\Gamma - H_1 H_c K_{fwd} \left(H_1 H_2 Q - \frac{H_2 H_6 \Delta \Gamma + \Lambda H_1 H_2 Q}{\Gamma \Theta + \Lambda} - Q \Gamma \right)} \end{aligned}$$

$$\begin{aligned} \frac{\Phi_{pas}(s)}{F_d(s)} &= \frac{1}{1 - \frac{-H_c H_{st} H_1 H_2 H_6 \Delta}{(\Gamma + H_1 H_{st})(\Theta + \Lambda) - H_1 H_2 \Lambda}} \\ &= \frac{(\Gamma + H_1 H_{st})(\Theta + \Lambda) - H_1 H_2 \Lambda}{(\Gamma + H_1 H_{st})(\Theta + \Lambda) - H_1 H_2 \Lambda + H_c H_{st} H_1 H_2 H_6 \Delta} \end{aligned}$$

Whereas the verification of these analytical expressions has already been shown in Figures 4.2a and 4.2b for the active stick, the graphs that verify the passive stick expressions are shown down below.

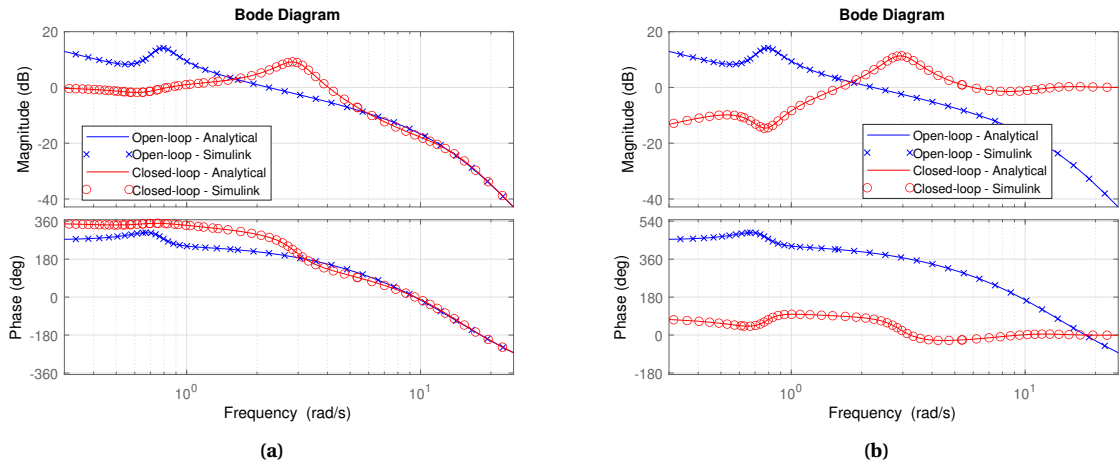


Figure A.3: Verification of the analytical descriptions for the passive stick model, for the open- and closed-loop (a) target tracking and (b) disturbance rejection response.

IV

Paper appendix

B

Clarification of the pilot model

This appendix provides a more detailed overview of the pilot model that has been used for all simulations. A schematic of the model is presented in Figure B.1, and the values associated to all model coefficients are shown in Table B.1.

Before this model was fitted on the experimental frequency response functions produced by Fu, some of the coefficients were first fixed as constants based on literature (iteration 0). After testing an array of different boundary conditions for the FRFs available for the low, medium and high signal bandwidth test runs conducted by Fu, observations were made with regards of the quality of the fit (iteration 1). As a result, more coefficients were set as constants. Furthermore, the linear dependencies that were first present between K_p , K_v and K_f were removed, as this greatly increased the quality of the fit. At the same time, the more conservative upper and lower bounds of said variables according to Bhoelai [46] were selected, although this ended up having almost no effect on the gain settings that were finally selected.

In case the full explanation is desired behind the definition of the data fitting algorithm and the reasoning towards the values presented in Table B.1, the reader is referred to Sections 4.1 and 4.2 in the preliminary thesis, respectively.

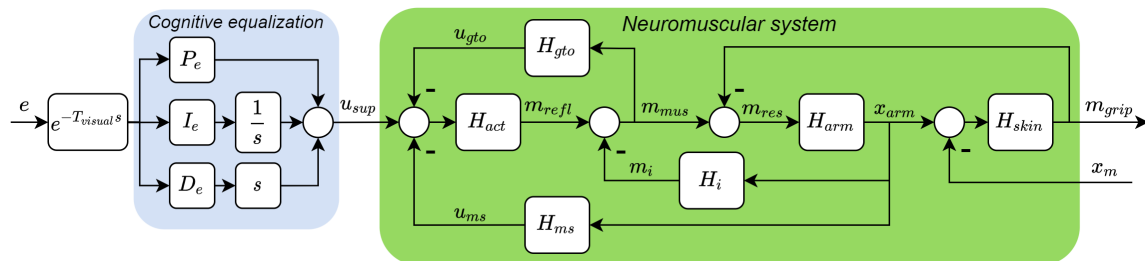


Figure B.1: A more detailed overview of the pilot model that is used in the simulations.

Table B.1: An overview of the pilot coefficients that were defined as constants (green), and the remaining ones that were estimated for each pilot control style.

Category	Parameter	Symbol	Iteration		Pilot control style			Unit
			0	1	Rlx.	Avg.	Amb.	
Skin dynamics (H_{skin})	Stiffness	K_{skin}	[165, 400]	165				[Nm / rad]
	Damping	B_{skin}	[0.5, 5]	5				[Nms / rad]
Arm dynamics (H_{arm})	Inertia	I_{arm}	0.01	0.01				[Nms ² / rad]
Other intrinsic arm dynamics (H_i)	Damping	B_i	[0.05, 1]	0.05				[Nms / rad]
	Stiffness	K_i	[3, 11]	[3, 6.5]	3	4.5	6	[Nm / rad]
Muscle spindle dynamics (H_{ms})	Muscle stretch	K_p	[-6, 9]	[-30, 30]	-1.28	-1.61	-2.91	[Nm / rad]
	Muscle stretch rate	K_v	[0, 3]	[-5, 10]	0.04	0.095	0.21	[Nms / rad]
	Neural transport delay	T_{ms}	0.025	0.025				[s]
Golgi tendon organ dynamics (H_{gto})	Muscle force	K_f	[-1.5, 1.5]	[-20, 20]	0.2	1.2	2	[-]
	Neural transport delay	T_{gto}	0.025	0.025				[s]
NM activation dynamics (H_{act})	Corner frequency	ω_{act}	13.823	13.823				[rad / s]
	Damping	b_{act}	0.7071	0.7071				[-]
Cognitive response	Proportional gain	P_e	[-15, 0]	[-5, 0]	-1	-2	-3	[-]
	Integrator gain	I_e	[-15, 0]	[-5, 0]	-0.23	-0.36	-0.39	[-]
	Differentiator gain	D_e	[-15, 0]	[-5, 0]	-0.113	-0.241	-0.566	[-]
	Visual response time	T_{visual}	0.25	0.25				[s]

C

Participant briefing

This document provides an overview of the experiment that is going to be conducted as part of an MSc thesis at the Technical University Delft. Section C.1 provides some context and introduces the objective of this thesis. Section C.2 describes the experiment that every participant will partake in, along with the accompanying risks stated in Section C.3. Section C.4 presents the general experiment planning for a given participant.

C.1. Context of the experiment and research objective

To understand what this research is about, one can think of the example of a person driving a car or riding a bicycle. In such a situation, the steering device serves two major purposes:

1. It allows the ‘pilot’ to send control commands to the vehicle (Pilot wants to turn left → Pilot rotates steering device to the left → Vehicle turns left).
2. It allows the vehicle to tell the pilot in which direction it is moving (A wind gust pushes the vehicle rightwards → As a result, the steering device rotates to the right → The pilot feels his / her arms being moved right and can react to it). Cues like these revolve around the sense of touch in the skin and the sense of force and displacement in joints and muscles, and are known as **haptic cues**.

To put it differently; in the case of cars and bicycles, the position of the steering device and the motion of the vehicle are effectively coupled. Such a configuration has proven to be effective for rejecting disturbances like wind, as it allows one to respond much more quickly using the intrinsic mechanical properties of the arms (as well as their reflexive behavior), rather than a situation where one must rely on eyesight alone to detect any disturbances and respond with an arm command accordingly.

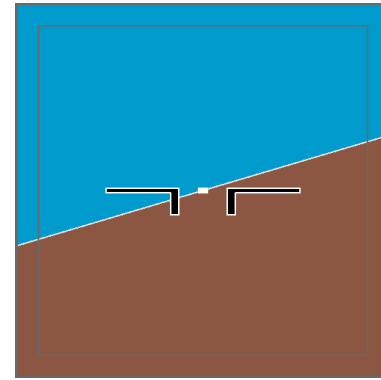
In current aircraft control, only elementary forms of haptic feedback exist. The most well-known example of this is the stick shaker, which warns the pilot of an impending stall condition using vibrations from the stick. In this project, however, a haptic configuration comparable to that of the car and bicycle is tested. In this case, the lateral position of the stick is coupled to the aircraft’s roll rate. Previous research has shown that such a configuration provides significant benefits in the context of aircraft control as well, and it has the potential to considerably stretch the limit of what systems pilots can stabilize / control manually (e.g; cases of extreme turbulence, an intrinsically unstable fighter jet whose stability augmentation systems malfunctions or an aircraft whose dynamic behavior suddenly deteriorates due to wing / engine damage). This project aims to determine a comprehensive set of guidelines to design / tune a control system involving such a haptic link between the pilot and the aircraft.

C.2. The experiment

A basic tracking task is going to be carried out by twelve participants. Figure C.1a shows the hardware that participants will use in the fixed-base simulator: the digital flight display and the side stick. Figure C.1b shows what participants will see on the digital flight display: the current attitude of the aircraft. Participants are tasked with keeping their aircraft level with the horizon. The challenge comes from the two forcing functions that drive the system. Firstly, a relatively slow signal is included, such that you are essentially dealing with a moving target. Secondly, a relatively fast



(a) The hardware that will be used in the experiment.



(b) The artificial horizon that participants will see on the digital flight display.

Figure C.1: A visual summary of the experimental setting.

signal is included to simulate turbulence. The task involves only one degree of freedom, namely the aircraft roll angle. For this reason, the side stick's pitch angle is constrained in the neutral position.

To derive a set of design guidelines for such a configuration, three degrees of freedom will be tested: the aircraft dynamics (Boeing 747 vs. Cessna Citation) as well as the feed-forward and feed-back gains related to the 'active' side stick. Three stick settings will be tested for each aircraft, resulting in a total of six conditions for which the results will be reported in the thesis. The performance of all participants is quantified using measurements of the force applied on the stick, the stick deflection, the aircraft roll angle and the target / disturbance forcing functions that drive the system.

C.3. Risks

Due to the nature of the experiment, there are very few risks for the participants involved. As the digital measurements will only be labelled using participant numbers, the only personal information that is stored is the participant's name on the signed informed consent form. This information is only stored physically by the responsible researcher of this project, Dr. ir. René van Paassen (up to five years after project completion). Besides the risks regarding privacy, there are virtually no risks related to psychological or physiological well-being, as the control task imposes little strain on the user. If anything, boredom is likely the biggest risk involved in the experiment.

C.4. Planning

The performance of participants will be assessed using runs of 90 seconds. For every condition, there are an estimated 8-10 runs required to get consistent data (the last five runs are averaged for every condition), which results in an estimated 15-20 minutes needed per condition. Every participant will test the first six conditions about which will be reported. Additionally, each participant will try one of the two to four 'exotic' settings that are pushing the limits in terms of stability margins at the end of their session, such that some additional insight can be acquired by the research group for this control configuration. In total, the experiment is expected to take approximately 3 hours per participant, see Figure C.2.

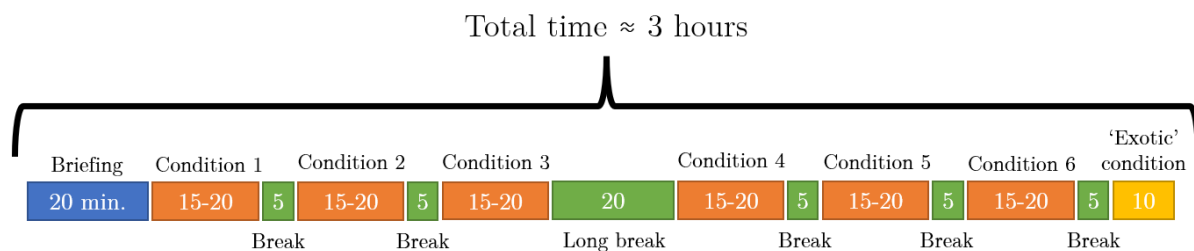


Figure C.2: General planning of the experiment for a given participant.

D

All experimental frequency response functions

This appendix provides an overview of the frequency response functions of all testing conditions in different comparisons. Figs. D.1 and D.2 compare the B747's and Cessna's FRFs at the tested feed-forward gain settings. Figs. D.3 and D.4 do the same for the tested feed-back settings for the B747 and the Cessna, respectively. Finally, Figs. D.5 and D.6 compare the conditions of double feed-forward and double feed-back gains for the B747 and the Cessna, respectively.

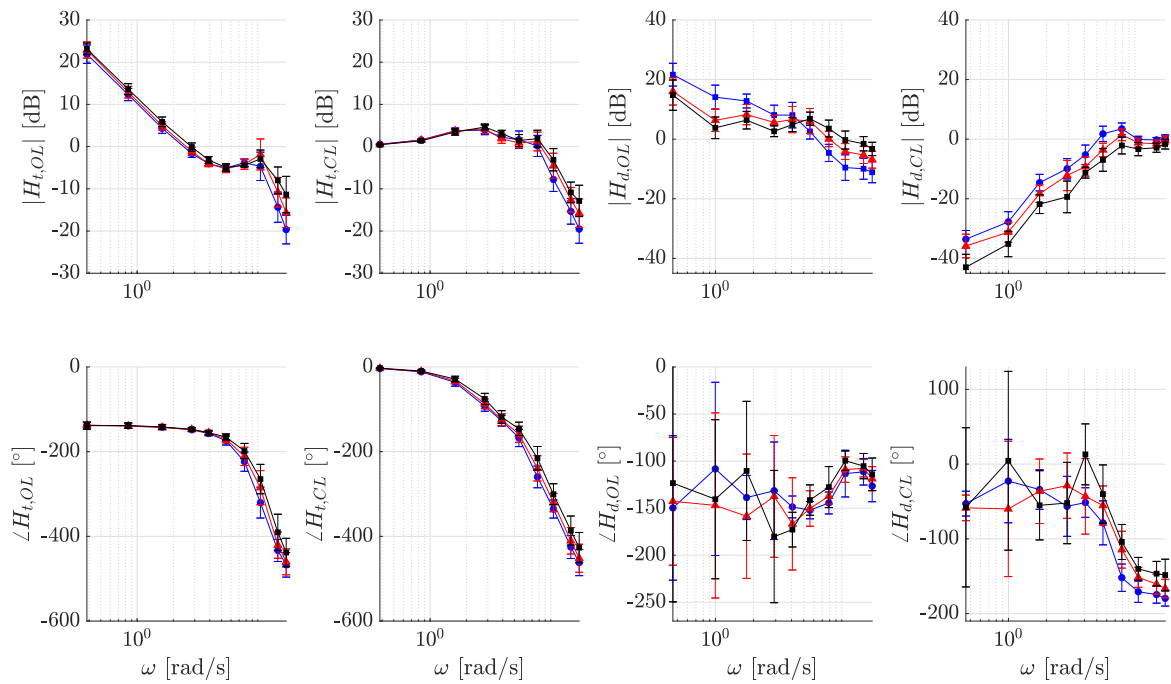


Figure D.1: The frequency response functions of conditions 1 (blue circle), 2 (red triangle) and 7 (black square), which respectively represent the cases of single, double and triple K_{fwd} for the Boeing 747. All values are reported as mean \pm std. deviation.

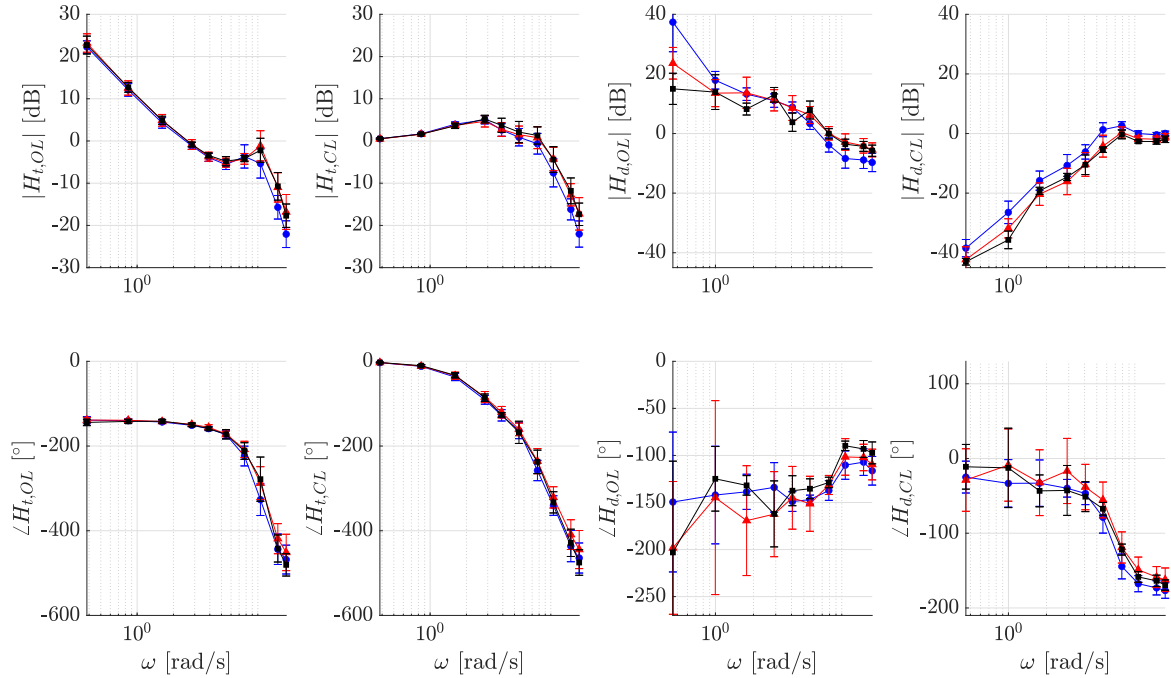


Figure D.2: The frequency response functions of conditions 4 (blue circle), 5 (red triangle) and 8 (black square), which respectively represent the cases of single, double and triple K_{fwd} for the Cessna Citation II. All values are reported as mean \pm std. deviation.

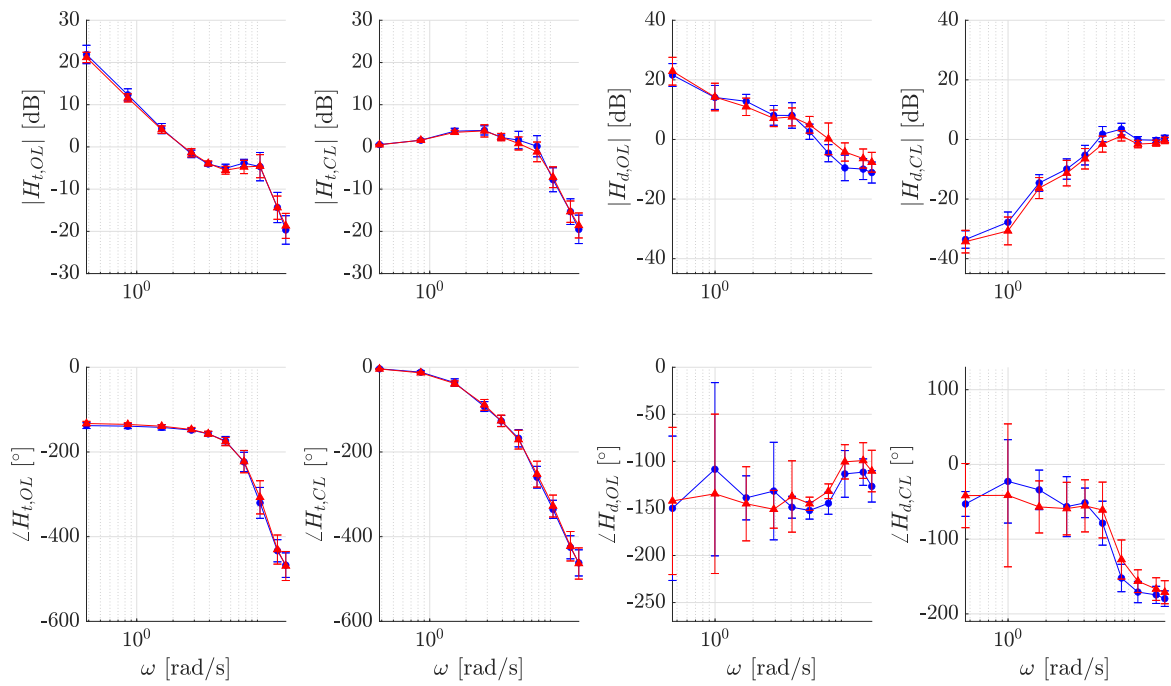


Figure D.3: The frequency response functions of conditions 1 (blue circle) and 3 (red triangle), which respectively represent the cases of single and double $K_{\dot{\phi}}$ for the Boeing 747. All values are reported as mean \pm std. deviation.

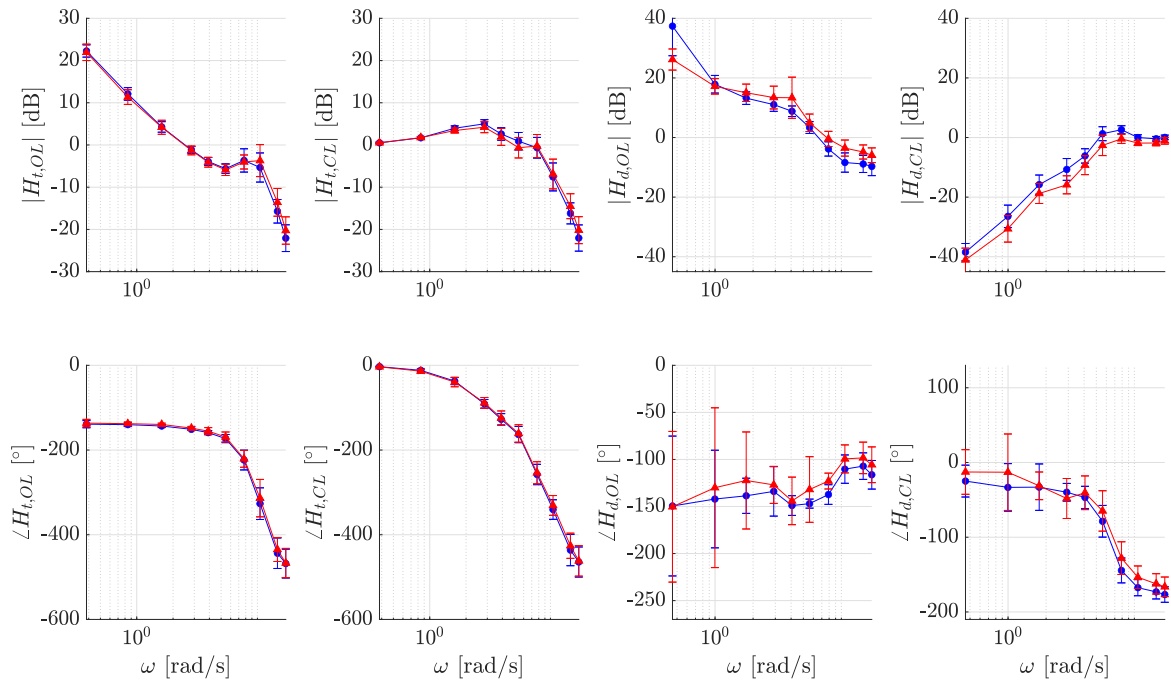


Figure D.4: The frequency response functions of conditions 1 (blue circle) and 3 (red triangle), which respectively represent the cases of single and double $K_{\dot{\phi}}$ for the Cessna Citation II. All values are reported as mean \pm std. deviation.

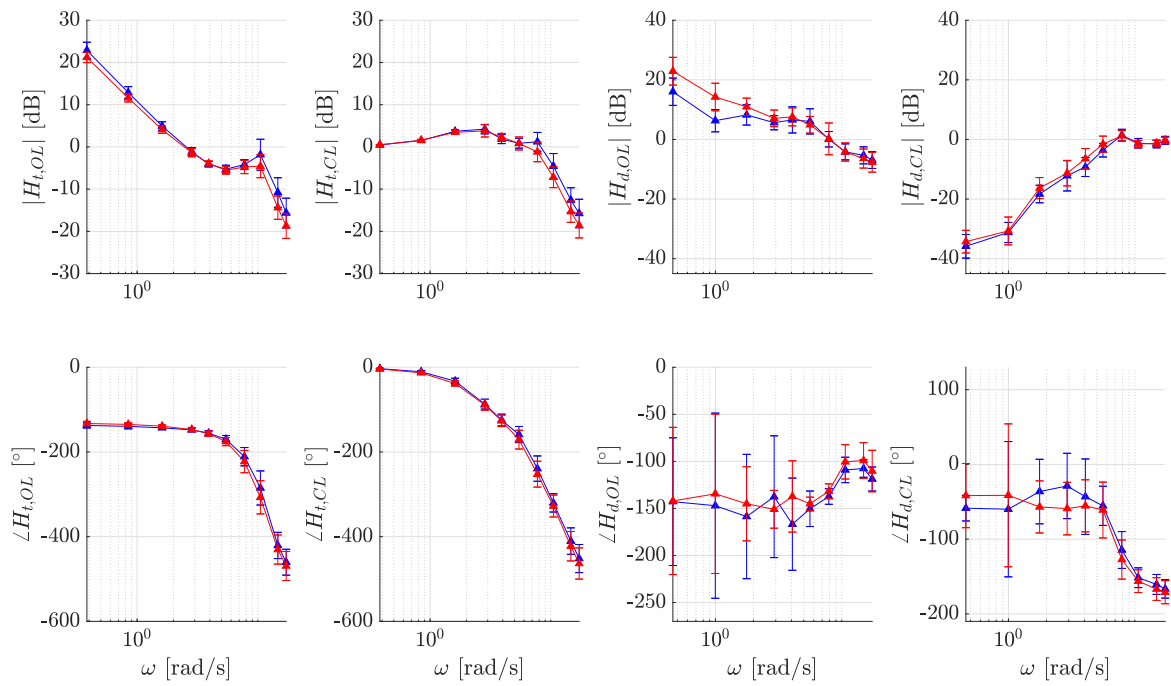


Figure D.5: The frequency response functions of conditions 2 (blue) and 3 (red), which respectively represent the cases of double K_{fwd} and double $K_{\dot{\phi}}$ for the Boeing 747. All values are reported as mean \pm std. deviation.

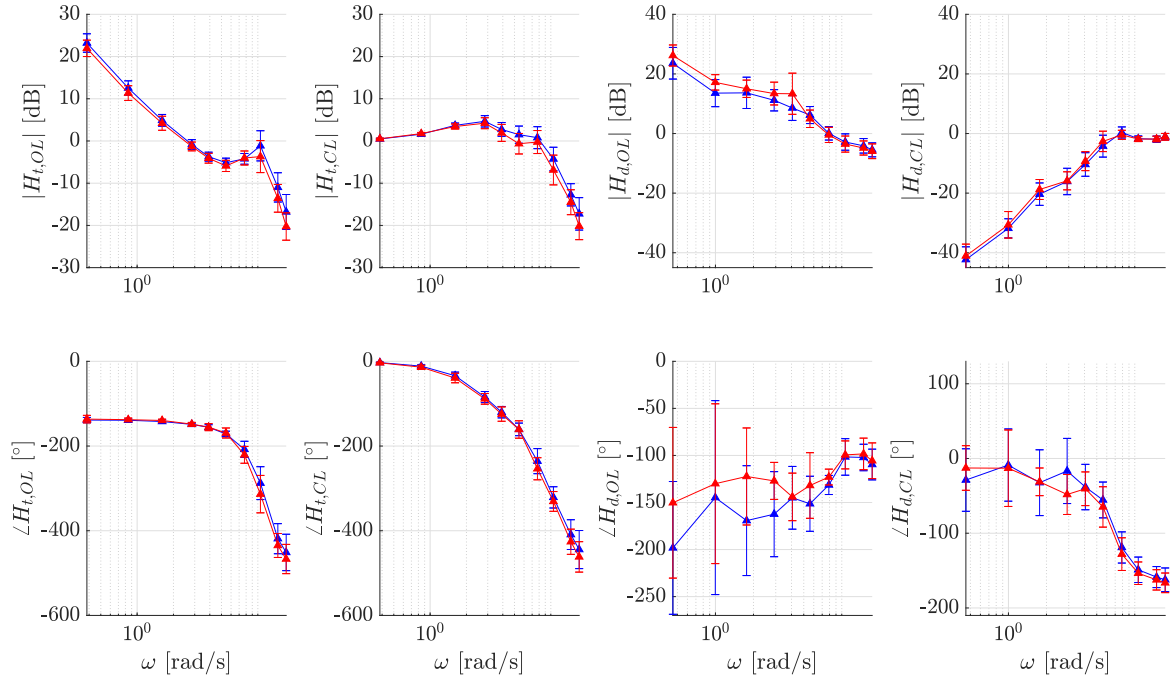


Figure D.6: The frequency response functions of conditions 2 (blue) and 3 (red), which respectively represent the cases of double K_{fwd} and double $K_{\dot{\phi}}$ for the Cessna Citation II. All values are reported as mean \pm std. deviation.

E

Instructions for the project's code

This section provides a comprehensive overview of the bundle of files that was used to estimate the neuromuscular parameters, simulate the experiment, store the experimental data and process / plot said experimental data. Instructions are provided whenever a script provides the user with easy ways to adjust parameters to his/her liking. For all MATLAB files holds that the adjustable parameters have been collected in a clearly indicated 'user input zone' at the top of the file to improve the ease of use.

Neuromuscular parameter estimation files

The script *Datafitter_active_V3.m* estimates the neuromuscular parameters based on the FRFs produced by Fu [14] for the low, medium or high forcing function signal bandwidth, by minimizing the cost function *ActiveStickCostfunc_V3.m* using the MATLAB routine *fmincon.m*. The user input zone in this file allows for the selection of upper and lower limits for ten neuromuscular parameters, which can also be constrained at a fixed value here. The file *Datafitter_constants.m* defines the remaining variables which are considered constants in the data fitting procedure, and which can be adjusted as well. *Datafitter_Active_V3.m* calls upon various functions and MATLAB workspaces which contain no information that should be altered.

The outcome of a wide array of tested constraint sets has been stored in 'NMS_Parameter_...Estimation_Overview.xlsx'. The Excel file 'NMS_Gains_Trend_Identification.xlsx' continues the analysis and identifies the linear combinations between certain NMS coefficients that produce equally low cost values for *ActiveStickCostfunc_V3.m*. The MATLAB file *Planes_plotted.m* plots these trends in three-dimensional planes. Going back to 'NMS_Parameter_Estimation_Overview.xlsx', the gains that were finally selected for the relaxed, average and ambitious pilot are shown in rows 96, 99 and 102, respectively.

Simulation / experiment baseline files

The file *CE_dynamics.m* generates the transfer functions and a Bode plot of the aircraft dynamics that were used for the simulations as well as the experiment. It also contains the most important note with regards to the difference in sign conventions between the preliminary thesis / simulation code and the final paper:

Note how the transfer functions that were determined for the F-16 and the Cessna have strictly negative numerator components. This is in line with the sign convention in aircraft control: positive lateral stick displacement (leftwards) results in a negative roll rate. This does come across as confusing for the average reader with respect to the system's stability, as the pilot's equalization gains of an error signal in a tracking task are typically positive (whereas they ought to be negative in our case). You can either have:

- Controlled element dynamics with negative numerator components, a haptic feedback gain that is negative and pilot equalization (PID) gains that are all negative. This is the notation that complies with the standard sign convention, and it is the way in which it has been simulated in MATLAB and reported in the preliminary thesis.

- Controlled element dynamics with positive numerator components, a haptic feedback gain that is positive and pilot equalization (PID) gains that are all positive. This is by far a less confusing notation for the average reader and values are therefore reported as such by Fu [14] and by me in the paper.

The file *Simulation_signals.m* defines the time vector and forcing functions that were used for the simulations as well as the experiment in the HMI-lab.

Simulation files

The file *Joystick_Models.slx* is the Simulink model that forms the core of all simulation work. It contains a model for both the active and passive manipulator configuration.

The MATLAB script *Iterative_Performance_Estimation.m* allows the user to test an array of feed-forward and feed-back gains for all three aircraft, with a 'relaxed', 'average' or 'ambitious' pilot control style. This is done by averaging the results of 'N_iterations' (30) samples that had a proper signal-to-noise ratio for the cognitive nonlinearities injected at the perceived error signal e , in line with the findings produced by Levison [42] and Van der El [43].

The file *Joystick_Models_SingleRunInitialization.m* allows the user to run the Simulink model a single time using one aircraft, one feed-forward gain, one feed-back gain and one pilot control style. With this script, the Simulink model does not model any cognitive nonlinearities, as the noise intensity needs to be determined iteratively and depends on the selected hardware settings. Furthermore, an overview of the simulated time-domain metrics for the low and medium bandwidth forcing functions can be found in 'SimulationResults_Timedomain_Low/MedBW.xlsx'.

Experimental data processing files

The file *ExperimentalResults_DataImport.m* imports the raw experimental data which is stored in a separate folder. The output of this script has been stored in a MATLAB workspace, which *ExperimentalResults_ProcessingAndPlots.m* uses to process and plot all the results shown in the paper.